学 位 論 文

Ultrafast chiroptical spectroscopy and its application to biomolecular dynamics

（ 超高速キラル分光法の開発と生体分子ダイナミクスへの応用 ）

平成27年12月 博士（理学）申請

東京大学大学院理学系研究科
化学専攻

平 松 光 太 郎

Contents

Part I Introduction

Part II Femtosecond time-resolved CD spectroscopy

Part III CARS-ROA spectroscopy

Part IV Summary

Abstract

Chiral structure is ubiquitously found in nature. Especially in biomolecular science, chirality plays a central role because the building blocks of biomolecules such as L-amino acids and D-sugars are chiral and enantiopure. Since the Pasteur's discovery of the connection between molecular asymmetry and optical rotation, asymmetric interaction between chiral molecules and circularly polarized light has been utilized for studying chirality. Today, chiroptical spectroscopy such as electronic and vibrational circular dichroism (ECD, VCD) and Raman optical activity (ROA) is widely recognized as a powerful tool and routinely performed with commercially available spectrometers. The development of chiroptical spectroscopy has been fueled by the growing demands of chemists and biologists for obtaining more detailed structural information of complicated molecules beyond the framework established by the conventional non-chiroptical spectroscopy.

Such development toward chiroptical spectroscopy is, in turn, one of the major aims in the area of ultrafast spectroscopy. Molecules to be measured in the ultrafast spectroscopy also become increasingly complicated and new ultrafast techniques with better structural sensitivity are becoming required. Development of ultrafast chiroptical method is, however, quite challenging due to weakness of the chiroptical signal and instability of ultrashort light sources. In this thesis work, ultrafast chiroptical techniques are realized through overcoming such difficulties by employing polarization-resolved optical-heterodyne detection.

First, femtosecond time-resolved CD (TRCD) spectroscopy which is practically applicable to biomolecular dynamics is developed. It becomes possible to measure CD spectra of transient chemical species produced by the pump pulse with the time resolution better than 300 fs. Proof-of-principle TRCD experiments with Λ- and Δ-Ru(bpy)$_3^{2+}$ show that broadband spectra covering almost the whole visible spectral range can be measured with the sensitivity better than 0.4 mdeg. One of the biggest hurdles in TRCD spectroscopy is artificial signals arising from molecular orientation induced by the pump radiation. I demonstrate this problem is solved by resolving a series of time-resolved spectra by the singular value decomposition into genuine CD and artificial spectra. Using this new technique, chirality change of biomolecules in the excited state is investigated. TRCD and transient absorption spectra of bilirubin bound to human serum albumin at pH=4.0 and 7.8 are measured. The results show that bilirubin undergoes ultrafast chirality flip with the time constant of about 10 ps at pH=4.0 but does not at pH=7.8. This is, to the best of my knowledge, the first direct observation of ultrafast chirality reversal.

Second, a new spectroscopic method to measure ROA by coherent anti-Stokes Raman scattering (CARS-ROA) is developed. ROA spectroscopy has better structural resolution than CD spectroscopy but its signal intensity is several orders of magnitudes smaller than that of CD; the development of time-resolved ROA spectroscopy is extremely challenging. In this thesis work, by exploiting multiplex CARS technique with the polarization-resolved heterodyne detection, ROA measurement with markedly higher contrast ratio of the chiral signal to the achiral background is realized. The developed CARS-ROA spectroscopy also enables to measure ROA spectrum using a pulsed laser source. Since the first observation of CARS-ROA in 2012, I have developed three different spectrometers to improve the performance. The first setup employs the near-infrared incident light and self-heterodyne scheme. Although the contrast ratio is much better than that the conventional ROA spectroscopy, the signal to noise ratio is worse than the conventional ROA spectroscopy mainly due to intrinsic weak scattering intensity in the near-infrared. In the second-generation CARS-ROA, the active-heterodyne detection is employed. Measurement of spectra with less artifact is accomplished because a broad offset artifact due to optical rotatory dispersion could be quantitatively distinguished in the active heterodyne detection. In the third-generation, the wavelength of the incident light is changed to the visible with the self-heterodyne method. In the visible excitation, both the absolute signal intensity and the contrast ratio become higher than those in previous generations and much better signal to noise ratio is accomplished. Although the CARS-ROA measurement is performed for a system in the steady state, the method can readily be applied to the time-resolved measurements by introducing the pump pulses.

The methods developed in the present study open up a new class of spectroscopy which can directly discuss chirality changes during various photochemical reactions. Besides the illustrative demonstration measuring the ultrafast chirality flip of the bilirubin-protein complex, the developed ultrafast chiroptical spectroscopy will play essential roles for investigating mechanisms of a variety of chemical and biochemical reactions.

Part I

Introduction

Chapter 1

Introduction

1.1 Chiroptical spectroscopy

Chirality is the aspect of an object which that is not superposable on its mirror image. Chiral structure is found throughout the nature, from the elementary particles [1] to living systems [2]. Due to its handedness, chiral structure interacts differently with left- and right-circularly polarized radiation. Chiroptical spectroscopy exploits such difference to extract structural information of the chiral structures.

In the context of chemistry, a chiroptical phenomenon was first observed by Arago in 1811 in the form of the rotation of the linear polarization in a quartz crystal, which we call optical rotation (OR) [3]. Arago's discovery was followed by the observation of OR in organic molecules in liquid and solution phases [4]. Based on these discoveries, molecular chirality was found to be the source of OR. Optical rotation is understood as a difference in refractive indices of left- and right-circularly polarized light because the linearly polarized light is regarded as a superposition of left- and right-circularly polarized light. An absorption analog of OR, circular dichroism (CD), is another form of the chiroptical processes. Circular dichroism was first observed in 1847 and is most widely used chiroptical technique today.

Up to the 1950s, most of chiroptical measurements had been performed at a single wavelength, usually at the sodium D line at 589 nm. Due to the development of electronics in the 1950-60s, it became possible to routinely measure the wavelength dependence of OR and CD by commercially available spectrometers. Since then, CD and optical rotatory dispersion (ORD) spectroscopy has been applied to structural investigation of a variety of molecules such as dienes [5, 6], benzene compounds [7], biaryls [8], helical polymers [9], metal compounds [10], amino acids [11], polypeptides [12], proteins [13–16], and nucleic acids [17, 18].

In the CD studies of relatively small chiral organic molecules, the aim is the determination of abso-

lute configurations, which is the most straightforward application of chiroptical spectroscopy because a chiroptical spectrum of one enantiomer forms the mirror image of that of the opposite enantiomer. Using the Rosenfeld's formula for calculating the rotational strength [19],

$$R = \mathrm{Im}[\langle 0|\boldsymbol{\mu}|\alpha\rangle \cdot \langle \alpha|\boldsymbol{m}|0\rangle], \tag{1.1}$$

the angle between the transition electric dipole moment and the transition magnetic dipole moment can be evaluated from the observed CD. Based on the above formula, non-empirical methods such as the octant rule [20] and the exciton chirality method [21] have been developed and used for intuitive estimation of absolute configuration from the observed rotational strength. Today, determination of absolute configurations is becoming even easier due to the development of *ab initio* quantum chemical calculations [22]. In the studies of large biopolymers, CD spectroscopy is mainly used as a tool for determining its secondly or higher order steric structure. Differently from the small molecules, biopolymers are still beyond the reach of the *ab initio* methods. So the CD spectra are usually analyzed empirically. Especially, for the structural studies of proteins, CD peaks of $n - \pi^*$ and $\pi - \pi^*$ transitions of amides below 250 nm are often measured as a marker because these are known to be sensitive to the protein secondary structures [16].

Along with the CD spectroscopy, the emission analog of it, circularly polarized luminescence (CPL) has evolved for investigating chiral features of the emitting states [23]. CPL is a unique technique because it can probe molecular chirality of the electronically excited states. Based on the fact that the rotational strength of CD and CPL are the same if no structural change undergoes in the excited states, structural change in the excited states can be discussed from CPL measurements [24]. However, what is measured in CPL spectroscopy is temporally averaged over the lifetime of luminescence. Hence, experimentally observed CPL spectrum is a superposition of those from different transient species, which makes the interpretation complicated [25].

Although chiroptical spectroscopy of electronic transitions has been used in stereochemistry and biochemistry, the range of application of ECD is restricted to molecules having electronic transitions whose transition wavelength is longer than $\sim$160 nm. In contrast, vibrational optical activity (VOA) can be applied to almost all molecules. It is because nearly all the molecules have vibrational transitions in the range between about 50 cm^{-1} and 3500 cm^{-1}. VOA is composed of vibrational circular dichroism (VCD) and Raman optical activity (ROA), in which circular intensity difference of infrared absorption and Raman scattering is observed, respectively. The measurable wavenumber of VOA ranges from 500 cm^{-1} to over 10000 cm^{-1} in VCD and from less than 30 cm^{-1} to 2000 cm^{-1} in ROA. Also in terms of abundance of the obtainable information about molecular structure, VOA spectroscopy has an advantage over the electronic optical activity spectroscopy. The application area of VOA is, therefore, very broad. For example, the determination of the absolute configurations by VCD [26], and ROA [27, 28] in combination with *ab initio* calculation, the estimation of the enan-

tiomeric excess in VCD [29] and in ROA [30] have been performed. VOA spectroscopy is a powerful tool even when the sample is a mixed solution because the spectrum has many characteristic peaks, the number of which is much more than that in the electronic optical activity spectrum [31].

Besides them, the most notable application of VOA is investigation of the three-dimensional configurations of biological molecules. VCD spectra of amino acids [32, 33], peptides [34–37], proteins [38, 39] with different temperature, pH, and solvents have been measured. From these studies, VCD spectral shape were found to be highly sensitive to the protein secondary structures. Based on the knowledges obtained in the early studies, phenomena more directly related to human pathologies such as protein fibrillogenesis have recently been studied [40, 41]. ROA studies of biomolecules such as amino acids [42], peptides [43, 44], carbohydrates [45–47], proteins [48, 49] and nucleic acids [50–52] have also been performed. ROA spectra provide structural information even for unfolded and partially folded proteins, to which it is hard to apply the X-ray crystallography and NMR spectroscopy [53]. For example, the intermediate structure in the formation of amyloid fibrils, which cause neurodegenerative diseases such as Alzheimer's disease, has been revealed by ROA studies [54]. ROA spectroscopy attracts an attention also as a tool for investigating the natively unfolded proteins, which lack a compact tertiary fold in its native state and are recently recognized to have important functions [55, 56].

As seen above, chiroptical spectroscopy has played important roles in a large area of chemistry. One of the key features is its wide applicability. Although the information provided by chiroptical spectroscopy does not have the atomic resolution like NMR and X-ray crystallography, much broader range of molecules can be investigated by chiroptical spectroscopy. In addition, another striking advantage of chiroptical spectroscopy is its potential applicability to ultrafast time-resolved measurement. It is expected that unique structural information of transient chemical species is extracted by time-resolved chiroptical spectroscopy as discussed in the following sections.

1.2 Ultrafast spectroscopy

Understanding the microscopic mechanisms of chemical reactions is one of the major goals in chemistry. Toward this end, ultrafast spectroscopy plays crucial roles because elementary steps of chemical reactions proceed with the timescale of femto- to picoseconds. Mainly due to the rapid progress of the laser technology, spectroscopic techniques now can track such molecular dynamics. In the pump-probe-type time-resolved spectroscopy, chemical reactions are initiated by the pump pulse and optical spectra during the following structural change is measured by the probe pulse. By the probe pulse, a variety of spectroscopic measurements such as UV-Vis absorption, infrared absorption, and Raman scattering are performed. The time resolution of the pump-probe method is determined by the cross-correlation of the pump and probe pulses. Since the invention of the laser in the 1950s [57, 58], temporal width of pulsed laser emission has become shorter and shorter. Today, time resolution better

than 100 fs is easily achieved using commercially available laser sources. Various chemical reactions including bond cleavage, charge transfer and *cis-trans* isomerizations have been investigated by the ultrafast spectroscopy [59]. In parallel with investigations of purely chemical reactions, studies focused on biological reactions have also been performed since the early stage of the ultrafast spectroscopy [60].

In the early works of ultrafast spectroscopy, electronic transitions of the excited state species from the near-UV to the near-infrared were mainly measured. Although the ultrafast spectroscopy in such wavelength range is still widely used today, interpretation of the obtained spectra is sometimes difficult because these are complicated primarily due to coupling to the surrounding solvents [61]. Ultrafast spectroscopy was then extended to vibrational transitions, with using the infrared [62] and Raman [63] spectroscopy. In general, vibrational spectra provide more insights into molecular structure but still are not in one-to-one correspondence with the molecular structure especially for complicated molecules like biomolecules. Consequently, the assignments of the spectral profile are sometimes difficult, and/or some dynamics can not be probed by the existing electronic and vibrational ultrafast spectroscopy. New ultrafast spectroscopic techniques that can probe molecular dynamics unexplored by the conventional methods have been desired.

1.3 Ultrafast chiroptical spectroscopy

As natural extension of the conventional ultrafast spectroscopies such as transient absorption and time-resolved Raman scattering, one can think up ultrafast chiroptical spectroscopy. As described in Section 1.1, chiroptical spectroscopy provides fruitful structural information of chiral molecules compared to the corresponding spectroscopy insensitive to chirality. The ultrafast chiroptical spectroscopy shall give rich structural information for the transient bio/chemical species. The extendability to ultrafast measurement is one significant advantage of chiroptical spectroscopy over NMR spectroscopy and X-ray crystallography. The time resolution of NMR spectroscopy is the order of milliseconds, which is determined by relaxation time scale of the nuclear spin. Therefore, if the material under measurement interconverts between A and B faster than the milliseconds, the obtained NMR spectrum just corresponds the average structure of A and B. Ultrafast NMR spectroscopy is, in principle, impossible. Time-resolved X-ray crystallography with using X-ray free-electron lasers (XFEL) is one of the frontiers of the current ultrafast spectroscopy [64] but it can track the dynamics only in the crystal phase. We need to consider the possibility that what is observed in time-resolved X-ray crystallography is different from the actual reactions in solutions or *in vivo*. In the optical spectroscopy including CD, VCD, and ROA, on the other hand, femtosecond measurements in the solution phase can be achieved by employing the pump-probe technique with femtosecond pulsed lasers.

In the early attempt to measure time-resolved CD (TRCD), standard CD spectrometer was em-

ployed to track the time evolution of the chemical reaction initiated by pump sources such as dye lasers [65]. In the standard CD spectrometer, continuous wave source (e.g. Xenon lamp) is used as a light source. The incident light is modulated to left- and right-circularly polarization by an electro-optic modulator and the transmitted light is detected with a lock-in amplifier in synchronized with the modulator. This allows TRCD measurement with milliseconds time resolution. Using these apparatuses, results of biological interest have appeared [66]. The time resolution was, however, limited by the modulation frequency of the electro-optic modulator and has been difficult to be improved. To observe faster dynamics, development of a novel technique was needed.

To achieve nanosecond TRCD, Lewis *et al.* developed an ellipsometric CD measurement technique in [67]. In the ellipsometric CD measurement, slightly elliptically polarized light is used as the incident light. When the slightly elliptically polarized light passes through the chiral sample, the minor axis intensity changes by CD. By monitoring the minor axis intensity of the transmitted light, CD spectra can be obtained. In this scheme, the modulation was not necessary because the contrast ratio of the chirality-induced intensity change and the intensity itself is relatively large in comparison with the conventional CD technique with the circular polarization. The time resolution of the ellipsometric CD spectroscopy is thus determined by the time cross correlation between the pump and the probe pulses. In principle, pico- or femtosecond TRCD measurement is possible in this scheme. Probably some technical problems such as intensity instability, polarization scrambling, and less tunability, hampered extension of the ellipsometric CD measurements to pico- and femtosecond time region, at least in the 1990s,.

For the shorter temporal resolution, TRCD spectroscopy again by the polarization modulation technique was developed in 1989 [68, 69]. This time, picosecond pulses from a dye laser pumped by a Q-switched Nd:YAG laser were modulated on a pulse-to-pulse basis. The Q-switch was triggered in synchronized with the modulator, and then the probe pulses were alternately left- and right-circularly polarized. The transmitted pulses were detected by a photomultiplier tube and a lock-in amplifier that was referenced to the modulation frequency. Time-resolved measurements were realized in a pump-probe manner.

More than ten years after the development of picosecond TRCD spectroscopy by the modulation technique, picosecond TRCD by the ellipsometric technique was developed by Niezborala *et al.* in 2006 [70]. It was argued that the measurement was easier than the polarization modulation technique. Recently, Cho *et al.* developed a new ECD/VCD measurement scheme, which they named heterodyne optical activity free induction decay (OA FID) characterization [71, 72]. This method is similar to the ellipsometric CD measurement but is more straightforward. They have used linear polarized femtosecond pulses as the probe. Polarizers were placed before and after the sample with the crossed Nicols configuration. The probe field was perturbed by the chiral sample and a small portion of the transmitted light passes through the polarizer after the sample. By measuring both the amplitudes and the phases

of the transmitted light by the spectral interferometry, CD and ORD spectra of the sample can be simultaneously obtained. They have demonstrated that steady-state ECD/VCD spectra were measured with a femtosecond light source as a proof-of-principle experiment of this new scheme. However, to the best of my knowledge, this method had not been applied to the actual time-resolved measurement up to this thesis work.

The detection limit of the previously developed ultrafast TRCD spectroscopy is the order of 10 mdeg [68, 70, 74]. The magnitude of steady-state CD signal observed in the visible, and near UV range is 10-100 mdeg when the concentration and path length are adjusted so that the absorbance becomes 1, which is the condition usually employed in pump-probe measurements. If 10% of the molecules are excited by the pump radiation, expected magnitude of ΔCD is 1-10 mdeg, comparable or smaller than the detection limit of the reported TRCD spectroscopy. To measure transient CD signal of a broad range of chiral molecules, including biomolecules, further improvement in sensitivity has been needed in TRCD spectroscopy.

As for vibrational optical activity, the time-resolved study has been almost unexplored; only one proof-of-principle ultrafast VCD measurement has been reported for a cobalt-sparteine complex [75]. Implementation of time-resolved VOA is even more challenging than that of the electronic TRCD because the absorbance difference of vibrational transitions is typically 10-100 times smaller than that of the electronic transitions. For the sake of an application of time-resolved VCD spectroscopy to more different samples such as peptides and proteins, setup with improved sensitivity was reported recently [76] but the measured time-resolved VCD spectra were still overwhelmed by an artificial signal. Time-resolved ROA spectroscopy is also a promising tool for tracking the ultrafast structural change of biomolecules. However, despite its high demand, time-resolved ROA measurements and even ROA measurements with pulsed lasers had not been reported before this thesis work.

1.4 Present study

As described in the previous section, some efforts have been made to realize the ultrafast chiroptical spectroscopy. However, it is still needed to improve its sensitivity and spectral bandwidth to apply it to many interesting biological systems. In this thesis work, I report two major contributions to the development of the ultrafast chiroptical spectroscopy.

First, broadband and ultrasensitive femtosecond TRCD spectroscopy is developed (Chapter 3). In the previously reported TRCD spectroscopy, sensitivity was in the order of 10 mdeg even at a single wavelength measurements [68, 70, 74]. In the present study, the sensitivity better than 0.4 mdeg was achieved in the broadband measurement covering the whole visible range (415 - 720 nm). The key for such improvements is using the polarization-resolved optical-heterodyne-detected CD measurement scheme. With the linearly polarized incident probe radiation, chirality-induced change of the electric

field is selectively detected by the optical heterodyne technique. Differently from the conventional intensity difference measurement, measurement is free from the achiral background and less susceptible to fluctuation of the optical system including the laser. Due to the broadband feature of the developed TRCD spectrometer, we can analyze a series of time-resolved spectra by multivariate analysis such as singular value decomposition (SVD). As discussed in Chapter 3, SVD is efficient not only for resolving spectra from different chemical species [77] but also for distinguishing the genuine TRCD signal and artificial anisotropic signals induced by the pump radiation. With the developed TRCD spectrometer, I demonstrate the first observation of ultrafast chirality flip in the excited state, which is observed in bilirubin-protein complex (Chapter 4). Bilirubin is dimer-like molecule consisting of two dipyrrinone groups, whose helicity is defined by the dihedral angle between them. Transient absorption and TRCD spectra of the complex after the photoexcitation were measured and interpreted well within the framework of the exciton coupling theory. Sign inversion of the excited state CD, which is attributed the ultrafast chirality flip in the excited state, is observed with the time constant of $\sim$ 10 ps. Ultrafast TRCD spectroscopy is proven to be a useful tool for probing chirality dynamics of biomolecular systems.

Second, a novel scheme to measure ROA using coherent anti-Stokes Raman scattering (CARS) is developed as a first step toward the time-resolved ROA measurements. CARS is one of the third-order nonlinear Raman processes. The signal intensity of CARS is several orders of magnitude larger than that of the spontaneous Raman scattering [78]. In the early 1980s, two theoretical papers proposing CARS-ROA were published [79, 80]. Since then, however, the experimental observation of CARS-ROA had not been achieved up to the present work. In Chapter 5, the proof-of-principle experiment of CARS-ROA in the near-infrared region is reported. I show ROA measurement is realized by detecting CARS radiation that is polarized perpendicularly to the incident polarizations, which are parallel to each other. To detect the extremely weak chirality-induced CARS radiation, the self-heterodyne detection method is employed by using the achiral CARS field as a local oscillator. Due to the more freedom of polarization configurations in coherent anti-Stokes Raman scattering than in spontaneous Raman spectroscopy, the contrast ratio of the chiral signal to the achiral background has been improved markedly. For (-)-β-pinene, it is two orders of magnitude better than that in the reported spontaneous ROA measurement. This is also the first measurement of ROA signal using a pulsed laser source. In Chapter 6, CARS-ROA spectroscopy is also demonstrated by using the active-heterodyne detection. The chirality-induced CARS field is amplified by a CARS field generated from an external reference and is extracted by the spectral interferometry. In this interferometric coherent Raman optical activity (iCROA), both the sign and the magnitude of optical active non-resonant background susceptibility can be directly determined. Measurement of a CARS-ROA spectrum with less artifact is obtained because a broad offset artifact due to optical rotatory dispersion is clearly distinguished in iCROA. In Chapter 7, CARS-ROA spectroscopy is extended to the visible range. In the visible excitation, CARS-ROA spectrum of (-)-β-pinene shows a higher contrast ratio of the chirality-induced signal to the achiral

background than that of the near-infrared CARS-ROA spectrum.

The methods presented here open up a new class of spectroscopy which can directly discuss chirality changes during various photochemical reactions. Observation of the excited-state ultrafast chirality flip by the TRCD spectroscopy is demonstrated as one of the illustrative examples of the ultrafast chiroptical spectroscopy. In addition to this, we can imagine a wide variety of application of the techniques developed here as will be discussed in Section 8.2. I believe these will be key tools for elucidating the mechanisms of biochemical reactions at the molecular level.

Chapter 2

Theory of linear and nonlinear chiroptical processes

2.1 Introduction

This chapter provides the basic theory of linear and nonlinear chiroptical processes based on the semi-classical theory. Chiroptical processes are generally understood as a difference in optical property between left- and right-circularly polarized light. Thus, the chiroptical counterparts of normal (not chiroptical) linear and nonlinear spectroscopy are generally conducted by measuring the optical signals with left- and right-circularly polarized light and taking the difference between them. However, chiroptical spectroscopy is feasible also by using linearly polarized light because linearly polarized light is the superposition of the circularly polarized light. As described in the following chapters, better signal to noise ratio can be achieved with such a scheme in some cases because background level is markedly suppressed. To comprehensively understand different forms of chiroptical spectroscopy, herein, explicit expressions of optical susceptibility tensors of chiroptical processes are derived.

2.2 Framework for calculating effective polarization by the density matrix formulation

Here, a general framework for calculating the optical susceptibility is given by using the density matrix formulation. In the density matrix formulation, the system is described by the density operator:

$$\rho = \sum_{\psi} p_{\psi} |\psi\rangle\langle\psi|, \tag{2.1}$$

where p_ψ is the probability that the system is in the state $|\psi\rangle$. In Eq. (2.1), $|\psi\rangle$ is the ket vector represented in the Schrödinger picture. With the Hamiltonian of the system, H, the time evolution of

the density operator is given by the Liouville equation:

$$\frac{d\rho}{dt} = \frac{1}{i\hbar}[H, \rho], \tag{2.2}$$

where $[\cdot, \cdot]$ is the commutator. Once one obtains the density operator by solving this differential equation, the expectation value of the observable A is given by

$$\langle A \rangle = \mathrm{Tr}(A\rho). \tag{2.3}$$

For convenience, the total Hamiltonian is assumed to be in the following form:

$$H = H_0 + H_{\mathrm{int}} + H_{\mathrm{R}}, \tag{2.4}$$

where $H_0, H_{\mathrm{int}}, H_{\mathrm{R}}$ represent the unperturbed molecular Hamiltonian, radiation-matter interaction Hamiltonian, and relaxation Hamiltonian, respectively. Including the electric dipole, magnetic dipole, and electric quadrupole interactions, the interaction Hamiltonian is written as [81]

$$H_{\mathrm{int}} = \sum_{i,j=1}^{3} \left(-\mu_i E_i - \frac{1}{6}\theta_{ij}\nabla_i E_j - m_i B_i \right), \tag{2.5}$$

where E and B represent the applied electric and magnetic field in the time domain and μ, m, and θ are the electric dipole, magnetic dipole, and electric quadrupole operators, respectively. Each operator is given by

$$\mu_i = \sum_s (r_s)_i q_s, \tag{2.6}$$

$$m_i = \sum_s \sum_{jk} \varepsilon_{ijk} (r_s)_j (p_s)_k q_s, \tag{2.7}$$

$$\theta_{ij} = \sum_s (3 r_i r_j - |\boldsymbol{r}|^2 \delta_{ij}) q_s, \tag{2.8}$$

where r_s, p_s, and q_s are the position, momentum, and charge of s-th charged particle, respectively, ε_{ijk} is the Levi-Civita's epsilon, and δ_{ij} is the Kronecker delta. The relaxation Hamiltonian H_{R} is defined by the following equation:

$$\frac{1}{i\hbar}[H_{\mathrm{R}}, \rho(t)]_{mn} = -\rho_{mn}(t)\Gamma_{mn}, \tag{2.9}$$

where Γ_{mn} is the damping constant of mn element of the density matrix.

To make the calculation concise, the interaction picture is employed below. The density operator

in the interaction picture, ρ_I, is defined as

$$\rho_I = \exp\left(-\frac{H_0}{i\hbar}t\right)\rho_S \exp\left(\frac{H_0}{i\hbar}t\right), \tag{2.10}$$

where the density operator in the Schrödinger picture is explicitly expressed as ρ_S, but this is the same as what is defined in Eq. (2.1). By differentiating Eq. (2.10), one obtains the time evolution of ρ_I as

$$\begin{aligned}
\frac{d\rho_I}{dt} &= -\frac{H_0}{i\hbar}\exp\left(-\frac{H_0}{i\hbar}t\right)\rho_S \exp\left(\frac{H_0}{i\hbar}t\right) \\
&\qquad + \exp\left(-\frac{H_0}{i\hbar}t\right)\left(\frac{d\rho_S}{dt}\right)\exp\left(\frac{H_0}{i\hbar}t\right) + \exp\left(-\frac{H_0}{i\hbar}t\right)\rho_S\left(\frac{H_0}{i\hbar}\right)\exp\left(\frac{H_0}{i\hbar}t\right) \\
&= \frac{1}{i\hbar}\Big[-H_0 \exp\left(-\frac{H_0}{i\hbar}t\right)\rho_S \exp\left(\frac{H_0}{i\hbar}t\right) \\
&\qquad + \exp\left(-\frac{H_0}{i\hbar}t\right)[H,\rho_S]\exp\left(\frac{H_0}{i\hbar}t\right) + \exp\left(-\frac{H_0}{i\hbar}t\right)\rho_S H_0 \exp\left(\frac{H_0}{i\hbar}t\right)\Big] \\
&= \frac{1}{i\hbar}\exp\left(-\frac{H_0}{i\hbar}t\right)\Big([H,\rho_S] - [H_0,\rho_S]\Big)\exp\left(\frac{H_0}{i\hbar}t\right) \\
&= \frac{1}{i\hbar}[H_{I,\mathrm{int}} + H_{I,R}, \rho_I],
\end{aligned} \tag{2.11}$$

where

$$H_{I,\mathrm{int}} = \exp\left(-\frac{H_0}{i\hbar}t\right)H_{S,\mathrm{int}}\exp\left(\frac{H_0}{i\hbar}t\right) \tag{2.12}$$

and

$$H_{I,R} = \exp\left(-\frac{H_0}{i\hbar}t\right)H_{S,R}\exp\left(\frac{H_0}{i\hbar}t\right) \tag{2.13}$$

are the interaction Hamiltonian and the relaxation Hamiltonian in the interaction picture, respectively. As shown in Eq. (2.11), the Liouville equation in the interaction picture formally resembles that in the Schrödinger picture (Eq. (2.2)), but the H_0 term is omitted. This is because the time evolution of the system by H_0 is included in the Hamiltonian side by sandwiching the Hamiltonian between $\exp\left(-H_0t/i\hbar\right)$ and $\exp\left(H_0t/i\hbar\right)$.

With it in mind that Eq. (2.9) remains the same in the interaction picture[1], Eq. (2.11) can be

[1] With $\rho_S = \exp\left(H_0t/i\hbar\right)\rho_I \exp\left(-H_0t/i\hbar\right)$ and $H_{S,R} = \exp\left(H_0t/i\hbar\right)H_{I,R}\exp\left(-H_0t/i\hbar\right)$, Eq. (2.9) is transformed to

$$(i\hbar)^{-1}\{\exp\left(H_0t/i\hbar\right)[H_{I,R},\rho_I]\exp\left(-H_0t/i\hbar\right)\}_{mn} = -\{\exp\left(H_0t/i\hbar\right)\rho_I\exp\left(-H_0t/i\hbar\right)\}_{mn}\Gamma_{mn}$$

As the matrix elements can be explicitly calculated as

$$\{\exp\left(H_0t/i\hbar\right)\}_{nm} = \delta_{nm}\exp\left(E_nt/i\hbar\right),$$

the equation is further transformed to

$$(i\hbar)^{-1}\exp\left\{(E_m - E_n)t/i\hbar\right\}[H_{I,R},\rho_I]_{mn} = -\exp\left\{(E_m - E_n)t/i\hbar\right\}\rho_{I,mn}\Gamma_{mn}.$$

explicitly written by

$$\frac{d\rho_{I,mn}(t)}{dt} = \frac{1}{i\hbar}[H_{I,\mathrm{int}}(t), \rho_I(t)]_{mn} - \Gamma_{mn}\rho_{I,mn}(t). \tag{2.14}$$

This differential equation can be formally integrated as

$$\rho_{I,mn}(t) = \frac{1}{i\hbar}e^{-\Gamma_{mn}t}\int dt'[H_{I,\mathrm{int}}(t'), \rho_I(t')]_{mn}e^{\Gamma_{mn}t'}. \tag{2.15}$$

In order to obtain the density operator of the system after n-times interactions with radiation, Eq. (2.15) is computed by the perturbative method. Below, it is assumed that the system is initially in the ground state, which is the eigenstate of H_0 with the lowest energy; the initial density operator is given by

$$\rho_I^{(0)} = e^{-\frac{H_0}{i\hbar}}|g\rangle\langle g|e^{\frac{H_0}{i\hbar}}. \tag{2.16}$$

The first order perturbation term, which is responsible for the linear optical processes, is then written as

$$\rho_{I,mn}^{(1)}(t) = \frac{1}{i\hbar}e^{-\Gamma_{mn}t}\int dt_1[H_{I,\mathrm{int}}(t_1), \rho_I^{(0)}]_{mn}(t_1)e^{\Gamma_{mn}t_1}. \tag{2.17}$$

In the same manner, the i-th order density operator is calculated as

$$\rho_{I,mn}^{(i)}(t) = \frac{1}{i\hbar}e^{-\Gamma_{mn}t}\int dt_i[H_{I,\mathrm{int}}(t_i), \rho_I^{(i-1)}]_{mn}(t_i)e^{\Gamma_{mn}t_i}. \tag{2.18}$$

Now, the expectation value of the i-th order linear/nonlinear electric dipole, electric quadrupole and magnetic dipole moment can be calculated through use of Eqs. (2.3), (2.6), (2.7), (2.8), (2.16) and (2.18).

In usual textbooks, induced polarization is given by

$$\boldsymbol{P}(t) = N\langle\langle\boldsymbol{\mu}(t)\rangle\rangle_r, \tag{2.19}$$

where N is the number density of molecules and $\langle\ \cdot\ \rangle_r$ denotes the average over all the orientation. Here, the theory is extended to include also the induced electric quadrupole and magnetic dipole mo-

---

The exponential terms are then cancelled out and one obtains

$$(i\hbar)^{-1}[H_{I,R}, \rho_I]_{mn} = -\rho_{I,mn}\Gamma_{mn}.$$

ments:

$$\boldsymbol{Q}(t) = N\langle\langle\boldsymbol{\theta}(t)\rangle\rangle_r, \tag{2.20}$$

$$\boldsymbol{M}(t) = N\langle\langle\boldsymbol{m}(t)\rangle\rangle_r. \tag{2.21}$$

When these contributions are taken into account, the constitutive equations become

$$\boldsymbol{D} = \varepsilon_0\boldsymbol{E} + \boldsymbol{P} - \nabla\cdot\boldsymbol{Q}, \tag{2.22}$$

$$\boldsymbol{H} = \frac{1}{\mu_0}\boldsymbol{B} - \boldsymbol{M}. \tag{2.23}$$

By substituting the above equations into the Maxwell's equations, the wave equation is obtained as

$$\begin{aligned}\nabla^2\boldsymbol{E} - \varepsilon_0\mu_0\frac{\partial^2\boldsymbol{E}}{\partial t^2} &= \mu_0\frac{\partial^2\boldsymbol{P}}{\partial t^2} - \mu_0\nabla\cdot\frac{\partial^2\boldsymbol{Q}}{\partial t^2} + \mu_0\nabla\times\frac{\partial\boldsymbol{M}}{\partial t} \\ &= \mu_0\frac{\partial^2}{\partial t^2}(\boldsymbol{P} - \nabla\cdot\boldsymbol{Q} + \int\nabla\times\boldsymbol{M}dt).\end{aligned} \tag{2.24}$$

Here, I define effective polarization by

$$\boldsymbol{P}^{\mathrm{eff}} = \boldsymbol{P} - \nabla\cdot\boldsymbol{Q} + \int\nabla\times\boldsymbol{M}dt. \tag{2.25}$$

By using this quantity, Eq. (2.24) can rewritten in a simple form as

$$\nabla^2\boldsymbol{E} - \varepsilon_0\mu_0\frac{\partial^2\boldsymbol{E}}{\partial t^2} = \mu_0\frac{\partial^2\boldsymbol{P}^{\mathrm{eff}}}{\partial t^2}. \tag{2.26}$$

This is formally the same as the well-known wave equation under the electric dipole approximation.

Equation (2.26) can easily be solved in the frequency domain. The Fourier transform of Eq. (2.26) is given by

$$\nabla^2\tilde{\boldsymbol{E}}(\omega) + \omega^2\varepsilon_0\mu_0\tilde{\boldsymbol{E}}(\omega) = -\omega^2\mu_0\tilde{\boldsymbol{P}}^{\mathrm{eff}}(\omega), \tag{2.27}$$

where $\tilde{\boldsymbol{E}}$ indicate the electric field in the frequency domain. By inserting the definition of the linear and nonlinear susceptibility,

$$\tilde{\boldsymbol{P}}^{\mathrm{eff}}(\omega) = \varepsilon_0[\chi^{(1,\mathrm{eff})}\tilde{\boldsymbol{E}}(\omega) + \chi^{(2,\mathrm{eff})}\tilde{\boldsymbol{E}}(\omega)\tilde{\boldsymbol{E}}(\omega) + \chi^{(3,\mathrm{eff})}\tilde{\boldsymbol{E}}(\omega)\tilde{\boldsymbol{E}}(\omega)\tilde{\boldsymbol{E}}(\omega) + \cdots], \tag{2.28}$$

into Eq. (2.27), the equation becomes the differential equation of the electric field with respect to the space. If the induced polarization is linearly dependent on the electric field, Eq. (2.27) becomes

$$\nabla^2\tilde{\boldsymbol{E}}(\omega) + \omega^2\varepsilon_0\mu_0(1 + \chi^{(1,\mathrm{eff})})\tilde{\boldsymbol{E}}(\omega) = 0. \tag{2.29}$$

By solving this differential equation with respect to the space, the electric field after passing through the medium can be calculated. When the higher order susceptibilities are taken into account, the power series of $\tilde{\boldsymbol{E}}(\omega)$ come out in the right hand side of Eq. (2.27). In such cases, the frequencies different from that of the applied field can be observed in the emission.

A general procedure for calculating the generated electric field as a result of the linear and nonlinear interaction is given in this section. Given the interaction Hamiltonian in Eq (2.5), the i-th order perturbative expansion of the density operator is given by Eq. (2.18). Next, one can evaluate the i-th order electric dipole, electric quadrupole and magnetic dipole moment induced by the external electric or magnetic field using Eqs. (2.3) and (2.18). The final electric field in the far field is then given by solving the wave equation (2.24). Practical examples of calculating generation of a chiroptical signal will be given in the following sections for linear and nonlinear cases.

2.3 Linear and nonlinear chiroptical processes

2.3.1 Linear

First, the effective polarization by the first order interaction is given. Before going into a case that the electric quadrupole and magnetic dipole interactions are included, the expectation value of the electric dipole moment only with the electric dipole interaction is considered as a starter. Using Eq. (2.17), the expectation value of the dipole moment is written as

$$\begin{aligned}\langle \mu_i(t) \rangle &= \sum_{m,n} (\mu_i)_{I,nm} \rho^{(1)}_{I,mn}(t) \\ &= \frac{1}{i\hbar} \sum_{m,n} (\mu_i)_{S,nm} \int_{-\infty}^{t} [H_{S,\mathrm{int}}(t'), \rho^{(0)}_S]_{mn} e^{(i\omega_{mn}+\Gamma_{mn})(t'-t)} dt'. \end{aligned} \tag{2.30}$$

The interaction Hamiltonian is now just the usual one with the electric dipole approximation:

$$H_{S,\mathrm{int}}(t) = -\sum_i \mu_i E_i(t). \tag{2.31}$$

The applied electric field is assumed to be superposition of planer waves with different frequencies as

$$E_i(t) = \sum_p \tilde{E}_i(\omega_p) e^{-i(\omega_p t - \boldsymbol{k_p z})}. \tag{2.32}$$

Eqs. (2.31) and (2.32) are introduced into Eq. (2.30) to obtain

$$\langle \mu_i(t) \rangle = \frac{1}{\hbar} \sum_p \sum_j \sum_m \left[\frac{(\mu_i)_{gm}(\mu_j)_{mg}}{\omega_{mg} - \omega_p - i\Gamma_{mg}} + \frac{(\mu_j)_{gm}(\mu_i)_{mg}}{\omega_{mg} + \omega_p + i\Gamma_{mg}} \right] \tilde{E}_j(\omega_p) e^{-i(\omega_p t - \boldsymbol{k_p z})}. \tag{2.33}$$

With the use of the molecular polarizability tensor, $\alpha_{ij}(\omega_p)$, the electric dipole moment is also written by

$$\langle \mu_i(t) \rangle = \sum_p \sum_j [\alpha_{ij}(\omega_p) \tilde{E}_j(\omega_p) e^{-i(\omega_p t - \boldsymbol{k_p} \boldsymbol{z})}]. \tag{2.34}$$

Comparing Eqs. (2.33) with (2.34), one can explicitly write down the polarizability tensor as

$$\alpha_{ij}(\omega_p) = \frac{1}{\hbar} \sum_m \Big[\frac{(\mu_i)_{gm}(\mu_j)_{mg}}{\omega_{mg} - \omega_p - i\Gamma_{mg}} + \frac{(\mu_j)_{gm}(\mu_i)_{mg}}{\omega_{mg} + \omega_p + i\Gamma_{mg}} \Big]. \tag{2.35}$$

Here, the first and second term becomes significant when $\omega_{mg} \simeq \omega_p$ and $\omega_{mg} \simeq -\omega_p$, respectively. In the situations considered in this thesis, the second term is negligible because the initial state is the ground state (Eq. (2.16)) and consequently $\omega_{mg} > 0$.

One notes that the polarizability tensor above is given in the molecular coordinate system. In order to obtain the susceptibility tensor observable in the experiments, one needs to convert the coordinate from the molecular system to the laboratory system and to compute the orientational average. Here, the Cartesian coordinates in the molecular system is written by x, y, z (or $i, j, \cdots$ for dummy indices) and these in the laboratory system by X, Y, Z (or $I, J, \cdots$ for dummy indices). When the Euler angle between these two coordinates systems is (ψ, θ, ϕ), tensor representations in these two coordinate systems are connected via the rotation matrix:

$$\begin{aligned} R &= \begin{pmatrix} R_x^X & R_y^X & R_z^X \\ R_x^Y & R_y^Y & R_z^Y \\ R_x^Z & R_y^Z & R_z^Z \end{pmatrix} \\ &= \begin{pmatrix} \cos\phi\cos\theta\cos\psi - \sin\phi\sin\psi & -\cos\phi\cos\theta\sin\psi - \sin\phi\cos\psi & \cos\phi\sin\theta \\ \sin\phi\cos\theta\cos\psi + \cos\phi\sin\psi & -\sin\phi\cos\theta\sin\psi + \cos\phi\cos\psi & \sin\phi\sin\theta \\ -\sin\theta\cos\psi & \sin\theta\sin\psi & \cos\theta \end{pmatrix}. \end{aligned} \tag{2.36}$$

For the second order tensor, expression in the laboratory coordinate system, S_{IJ}, can be obtained from that in the molecular coordinate system, S_{ij} by the following equation:

$$S_{IJ} = \sum_{i,j} R_i^I R_j^J S_{ij}. \tag{2.37}$$

In this thesis, experiments in the liquid phase, where molecules are randomly oriented, are considered. Thus, the observables obtained in the experiments correspond to the value added over all the orientations

$$\langle S_{IJ} \rangle_r = \frac{1}{8\pi^2} \int_0^\pi d\theta \sin\theta \int_0^{2\pi} d\psi \int_0^{2\pi} d\phi S_{IJ}, \tag{2.38}$$

where $\langle \cdot \rangle_r$ denotes the average over all the orientation as introduced in Eq. (2.19). Equation (2.37) is inserted into Eq. (2.38) to obtain

$$\begin{aligned}\langle S_{IJ} \rangle_r &= \frac{1}{8\pi^2} \sum_{i,j} S_{ij} \int_0^{\pi} d\theta \sin\theta \int_0^{2\pi} d\psi \int_0^{2\pi} d\phi R_i^I R_j^J \\ &= \frac{\delta_{IJ}}{3} \sum_{i,j} \delta_{ij} S_{ij} \\ &= \frac{\delta_{IJ}}{3} \sum_{i} S_{ii} = \frac{\delta_{IJ}}{3} (S_{xx} + S_{yy} + S_{zz}). \end{aligned} \tag{2.39}$$

For the calculation of the second- and third-order susceptibility tensors below, general formulas for the orientational average of third-, fourth- and fifth-order tensors are also given here [82]:

$$\langle S_{IJK} \rangle_r = \frac{1}{6} \sum_{i,j,k} \varepsilon_{ijk} \varepsilon_{IJK} S_{ijk}, \tag{2.40}$$

$$\langle S_{IJKL} \rangle_r = \frac{1}{30} \sum_{i,j,k,l} \begin{bmatrix} \delta_{IJ}\delta_{KL} \\ \delta_{IK}\delta_{JL} \\ \delta_{JK}\delta_{IL} \end{bmatrix}^T \begin{bmatrix} 4 & -1 & -1 \\ -1 & 4 & -1 \\ -1 & -1 & 4 \end{bmatrix} \begin{bmatrix} \delta_{ij}\delta_{kl} \\ \delta_{ik}\delta_{jl} \\ \delta_{jk}\delta_{il} \end{bmatrix} S_{ijkl}, \tag{2.41}$$

$$\langle S_{IJKLM} \rangle_r = \frac{1}{30} \sum_{i,j,k,l,m} \begin{bmatrix} \varepsilon_{IJK}\delta_{LM} \\ \varepsilon_{IJL}\delta_{KM} \\ \varepsilon_{IJM}\delta_{KL} \\ \varepsilon_{IKL}\delta_{JM} \\ \varepsilon_{IKM}\delta_{JL} \\ \varepsilon_{ILM}\delta_{JK} \end{bmatrix}^T \begin{bmatrix} 3 & -1 & -1 & 1 & 1 & 0 \\ -1 & 3 & -1 & -1 & 0 & 1 \\ -1 & -1 & 3 & 0 & -1 & -1 \\ 1 & -1 & 0 & 3 & -1 & 1 \\ 1 & 0 & -1 & -1 & 3 & -1 \\ 0 & 1 & -1 & 1 & -1 & 3 \end{bmatrix} \begin{bmatrix} \varepsilon_{ijk}\delta_{lm} \\ \varepsilon_{ijl}\delta_{km} \\ \varepsilon_{ijm}\delta_{kl} \\ \varepsilon_{ikl}\delta_{jm} \\ \varepsilon_{ikm}\delta_{jl} \\ \varepsilon_{ilm}\delta_{jk} \end{bmatrix} S_{ijklm}. \tag{2.42}$$

From Eqs. (2.19, 2.28, 2.34, 2.35, and 2.39), the observable susceptibility tensor is calculated as

$$\begin{aligned}\chi_{IJ}^{(1)} &= \frac{N}{\varepsilon_0} \langle R_i^I R_j^J \alpha_{ij} \rangle_r \\ &= \frac{N\delta_{IJ}}{3\varepsilon_0} (\alpha_{xx} + \alpha_{yy} + \alpha_{zz}). \end{aligned} \tag{2.43}$$

We see that only the diagonal elements of the susceptibility, $\chi_{XX}^{(1)}, \chi_{YY}^{(1)}$, and $\chi_{ZZ}^{(1)}$, have non-zero values and these are equal. With the explicit expression in Eq. (2.43), it can be checked that the susceptibility tensor is not sensitive to molecular chirality. Whether a physical value is sensitive to molecular chirality or not is determined by whether its sign reverse or not by the reflection through a plane. In order to calculate the polarizability after the reflection, it is convenient to set the reflection plane the xy-plane. From Eq. (2.43), it is obvious that the susceptibility does not change if the

subscripts x and y are interchanged:

$$\begin{aligned}\chi^{(1)}_{IJ} &= \frac{N\delta_{IJ}}{3\varepsilon_0}(\alpha_{xx}+\alpha_{yy}+\alpha_{zz}) \\ &\xrightarrow{\text{reflection}} \frac{N\delta_{IJ}}{3\varepsilon_0}(\alpha_{yy}+\alpha_{xx}+\alpha_{zz}) = \chi^{(1)}_{IJ}.\end{aligned} \tag{2.44}$$

Within the dipole approximation, as is well known, the linear spectroscopy is not chiroptical. This is, as shown below, in contrast to the case of the second-order nonlinear processes, which can be chiroptical even within the electric dipole approximation.

Now, the theory is extended to include the magnetic dipole and the electric quadrupole interactions by expanding the Hamiltonian to

$$H_{S,\text{int}} = -\sum_{i,j}\Big[\mu_i E_i(t) + m_i B_i(t) + \frac{1}{6}\theta_{ij}\nabla_i E_j(t)\Big]. \tag{2.45}$$

By introducing the above Hamiltonian into Eq. (2.30), the expectation value of the dipole moment is calculated as

$$\begin{aligned}\langle\mu_i(t)\rangle = \frac{1}{\hbar}\sum_p\sum_{jk}\sum_m\Big[&\frac{(\mu_i)_{gm}(\mu_j)_{mg}}{\omega_{mg}-\omega_p-i\Gamma_{mg}}\tilde{E}_j(\omega_p) + \frac{(\mu_i)_{gm}(m_j)_{mg}}{\omega_{mg}-\omega_p-i\Gamma_{mg}}\tilde{B}_j(\omega_p) \\ &+ \frac{1}{6}\frac{(\mu_i)_{gm}(\theta_{jk})_{mg}}{\omega_{mg}-\omega_p-i\Gamma_{mg}}\nabla_j\tilde{E}_k(\omega_p)\Big]e^{-i(\omega_p t-\boldsymbol{k_p z})}\end{aligned} \tag{2.46}$$

$$= \frac{1}{\hbar}\sum_p\sum_{jk}\Big(\alpha^{\text{ED}}_{ij}\tilde{E}_j(\omega_p) + \alpha^{\text{MD1}}_{ij}\tilde{B}_j(\omega_p) + \alpha^{\text{EQ1}}_{ijk}\nabla_j\tilde{E}_k(\omega_p)\Big)e^{-i(\omega_p t-\boldsymbol{k_p z})}. \tag{2.47}$$

Here the anti-resonant terms are neglected because only the transitions resonant with the real states are considered in circular dichroism spectroscopy. The superscripts ED, MD1 and EQ1 correspond to the terms with the electric dipole, magnetic dipole, and electric quadrupole interaction in the interaction Hamiltonian, respectively. Here, the MD and EQ terms are numbered in order to distinguish them from the effective polarization originating to the induced magnetic dipole and electric quadrupole by the electric dipole interaction. Each tensor element in Eq. (2.47) is given by

$$\alpha^{\text{ED}}_{ij} = \sum_m \frac{(\mu_i)_{gm}(\mu_j)_{mg}}{\omega_{mg}-\omega_p-i\Gamma_{mg}}, \tag{2.48}$$

$$\alpha^{\text{MD1}}_{ij} = \sum_m \frac{(\mu_i)_{gm}(m_j)_{mg}}{\omega_{mg}-\omega_p-i\Gamma_{mg}}, \tag{2.49}$$

$$\alpha^{\text{EQ1}}_{ijk} = \frac{1}{6}\sum_m \frac{(\mu_i)_{gm}(\theta_{jk})_{mg}}{\omega_{mg}-\omega_p-i\Gamma_{mg}}. \tag{2.50}$$

The linear susceptibility tensors corresponding to the ED, MD1, and EQ1 terms are calculated by

taking the orientational average (Eqs. (2.38) and (2.40)) of the above expression as

$$\chi_{IJ}^{(1,\mathrm{ED})} = \frac{N\delta_{IJ}}{3\varepsilon_0}(\alpha_{xx}^{\mathrm{ED}} + \alpha_{yy}^{\mathrm{ED}} + \alpha_{zz}^{\mathrm{ED}}), \tag{2.51}$$

$$\chi_{IJ}^{(1,\mathrm{MD1})} = \frac{N\delta_{IJ}}{3\varepsilon_0}(\alpha_{xx}^{\mathrm{MD1}} + \alpha_{yy}^{\mathrm{MD1}} + \alpha_{zz}^{\mathrm{MD1}}), \tag{2.52}$$

$$\chi_{IJK}^{(1,\mathrm{EQ1})} = \frac{N\varepsilon_{IJK}}{6\varepsilon_0}(\alpha_{xyz}^{\mathrm{EQ1}} + \alpha_{yzx}^{\mathrm{EQ1}} + \alpha_{zxy}^{\mathrm{EQ1}} - \alpha_{xzy}^{\mathrm{EQ1}} - \alpha_{zyx}^{\mathrm{EQ1}} - \alpha_{yxz}^{\mathrm{EQ1}}). \tag{2.53}$$

Here, one can immediately get

$$\chi_{IJK}^{(1,\mathrm{EQ1})} = 0 \tag{2.54}$$

by using the relationship,

$$\alpha_{ijk}^{\mathrm{EQ1}} = \alpha_{ikj}^{\mathrm{EQ1}}, \tag{2.55}$$

which is derived from the definition of the electric quadrupole moment in Eq. (2.8). So the electric quadrupole interaction term in the Hamiltonian does not contribute to the linear optical susceptibility when the system is isotropic. When the system is anisotropic, on the other hand, the electric quadrupole interaction has non-zero contributions to the linear susceptibility [83], which is not discussed further here. As shown in Section 2.3.3, the electric quadrupole interaction also has non-zero contributions for the third order nonlinear susceptibility.

As for the magnetic dipole term, it should be noted that $\chi_{IJ}^{(1,\mathrm{MD1})}$ represents relation between the induced polarizability and the incident magnetic field. The induced polarization in the laboratory coordinate system is given by

$$\tilde{P}_I = \varepsilon_0 \sum_J \left(\chi_{IJ}^{(1,\mathrm{ED})} \tilde{E}_J + \chi_{IJ}^{(1,\mathrm{MD1})} \tilde{B}_J \right). \tag{2.56}$$

Concise expression is obtained for the planer electromagnetic wave propagating along Z-axis, where the magnetic field is given by

$$\tilde{B}_X = -\frac{n}{c}\tilde{E}_Y, \tag{2.57}$$

$$\tilde{B}_Y = \frac{n}{c}\tilde{E}_X. \tag{2.58}$$

By inserting the above equations into Eq. (2.56), one obtains

$$\tilde{P}_X = \varepsilon_0 \left(\chi_{XX}^{(1,\mathrm{ED})} \tilde{E}_X - \frac{n}{c}\chi_{XX}^{(1,\mathrm{MD1})} \tilde{E}_Y \right), \tag{2.59}$$

$$\tilde{P}_Y = \varepsilon_0 \left(\chi_{YY}^{(1,\mathrm{ED})} \tilde{E}_Y + \frac{n}{c}\chi_{YY}^{(1,\mathrm{MD1})} \tilde{E}_X \right). \tag{2.60}$$

Next, the induced magnetic dipole moment is calculated. In the calculation of the induced magnetic dipole moment, the magnetic dipole and electric quadrupole interactions in the Hamiltonian are neglected because $\boldsymbol{m}$ and $\boldsymbol{\theta}$ are several orders of magnitudes smaller than $\boldsymbol{\mu}$. Thus, the induced magnetic dipole is given by

$$\begin{aligned}\langle m_i(t)\rangle &= \frac{1}{\hbar}\sum_p\sum_j\sum_m\left[\frac{(m_i)_{gm}(\mu_j)_{mg}}{\omega_{mg}-\omega_p-i\Gamma_{mg}}\right]\tilde{E}_j(\omega_p)e^{-i(\omega_p t-\boldsymbol{k_p z})} \\ &= \frac{1}{\hbar}\sum_p\sum_j\alpha_{ij}^{\mathrm{MD2}}\tilde{E}_j(\omega_p)e^{-i(\omega_p t-\boldsymbol{k_p z})},\end{aligned} \tag{2.61}$$

where

$$\alpha_{ij}^{\mathrm{MD2}} = \sum_m\frac{(m_i)_{gm}(\mu_j)_{mg}}{\omega_{mg}-\omega_p-i\Gamma_{mg}}. \tag{2.62}$$

By calculating the orientational average of the above expression, the susceptibility tensor associated with the MD2 term is given by

$$\chi_{IJ}^{(1,\mathrm{MD2})} = \frac{N\delta_{IJ}}{3\varepsilon_0}(\alpha_{xx}^{\mathrm{MD2}}+\alpha_{yy}^{\mathrm{MD2}}+\alpha_{zz}^{\mathrm{MD2}}). \tag{2.63}$$

Here, $\chi_{IJ}^{(1,\mathrm{MD2})}$ is defined as a physical value connecting the applied electric field and the induced magnetic polarization:

$$\tilde{M}_X = \varepsilon_0\chi_{XX}^{(1,\mathrm{MD2})}\tilde{E}_X, \tag{2.64}$$

$$\tilde{M}_Y = \varepsilon_0\chi_{YY}^{(1,\mathrm{MD2})}\tilde{E}_Y. \tag{2.65}$$

From the above equations, the effective polarization can be calculated via Eq.(2.25).

Finally, the induced electric quadrupole moment is discussed. Again, the magnetic dipole and electric quadrupole interactions in the Hamiltonian is neglected. The expectation value of the quadrupole moment is given by

$$\langle q_{ij}(t)\rangle = \frac{1}{\hbar}\sum_p\sum_k\sum_m\left[\frac{(\theta_{ij})_{gm}(\mu_k)_{mg}}{\omega_{mg}-\omega_p-i\Gamma_{mg}}\right]\tilde{E}_k(\omega_p)e^{-i(\omega_p t-\boldsymbol{k_p z})} \tag{2.66}$$

$$= \frac{1}{\hbar}\sum_p\sum_j\alpha_{ijk}^{\mathrm{EQ2}}\tilde{E}_k(\omega_p)e^{-i(\omega_p t-\boldsymbol{k_p z})}, \tag{2.67}$$

where

$$\alpha_{ijk}^{\mathrm{EQ2}} = \sum_m\frac{(\theta_{ij})_{gm}(\mu_k)_{mg}}{\omega_{mg}-\omega_p-i\Gamma_{mg}}. \tag{2.68}$$

The orientational average gives the susceptibility as

$$\chi_{IJK}^{(1,\mathrm{EQ2})} = \frac{N\varepsilon_{IJK}}{6\varepsilon_0}(\alpha_{xyz}^{\mathrm{EQ2}} + \alpha_{yzx}^{\mathrm{EQ2}} + \alpha_{zxy}^{\mathrm{EQ2}} - \alpha_{xzy}^{\mathrm{EQ2}} - \alpha_{zyx}^{\mathrm{EQ2}} - \alpha_{yxz}^{\mathrm{EQ2}}), \tag{2.69}$$

$$= 0. \tag{2.70}$$

As with the EQ1 term, $\chi_{IJK}^{(1,\mathrm{EQ2})}$ is zero in the expression of the linear susceptibility.

Now the effective induced polarization is calculated through the use of Eqs. (2.25, 2.59, 2.60, 2.64, 2.65) as

$$\begin{aligned}\tilde{P}_X^{(1,\mathrm{eff})} &= \varepsilon_0\Big(\tilde{P}_X + \frac{n}{c}\tilde{M}_Y\Big) \\ &= \varepsilon_0\Big(\chi^{(1,\mathrm{ED})}\tilde{E}_X - \frac{n}{c}\chi^{(1,\mathrm{MD1})}\tilde{E}_Y + \frac{n}{c}\chi^{(1,\mathrm{MD2})}\tilde{E}_Y\Big), \qquad (2.71)\\ \tilde{P}_Y^{(1,\mathrm{eff})} &= \varepsilon_0\Big(\tilde{P}_Y - \frac{n}{c}\tilde{M}_X\Big) \\ &= \varepsilon_0\Big(\chi^{(1,\mathrm{ED})}\tilde{E}_Y + \frac{n}{c}\chi^{(1,\mathrm{MD1})}\tilde{E}_X - \frac{n}{c}\chi^{(1,\mathrm{MD2})}\tilde{E}_X\Big). \qquad (2.72)\end{aligned}$$

Here, each element of the susceptibility tensor is just written by $\chi^{(1,*)}$ because in the isotropic case, $\chi_{XX}^{(1,*)} = \chi_{YY}^{(1,*)}$ is satisfied as shown in Eq. (2.51), (2.52) and (2.63). By defining $\chi^{(1,\mathrm{eff})}$ as

$$\chi_{XX}^{(1,\mathrm{eff})} = \chi_{YY}^{(1,\mathrm{eff})} = \chi^{(1,\mathrm{ED})}, \tag{2.73}$$

$$\chi_{XY}^{(1,\mathrm{eff})} = -\chi_{YX}^{(1,\mathrm{eff})} = -\frac{n}{c}(\chi^{(1,\mathrm{MD1})} - \chi^{(1,\mathrm{MD2})}), \tag{2.74}$$

one can simply write down the effective induced polarization in the form of

$$\tilde{\boldsymbol{P}}^{(1,\mathrm{eff})} = \varepsilon_0\chi^{(1,\mathrm{eff})}\tilde{\boldsymbol{E}}. \tag{2.75}$$

Now the electric field can be calculated by solving the differential equation (2.29) with the susceptibility tensor given in Eqs. (2.73) and (2.74).

It can be seen that the sign of $\chi^{(1,\mathrm{MD1})}$ and $\chi^{(1,\mathrm{MD2})}$ is inverted by the reflection through a plane. As with Eq. (2.44), the reflection through the xy-plane is considered. From Eq. (2.7), the magnetic dipole moment is converted by the reflection as

$$\begin{pmatrix} m_x \\ m_y \\ m_z \end{pmatrix} \xrightarrow{\text{reflection}} \begin{pmatrix} -m_y \\ -m_x \\ -m_z \end{pmatrix} \tag{2.76}$$

Through the use of Eqs. (2.49, 2.52, 2.62, 2.63, 2.76), one can readily obtain

$$\chi^{(1,\mathrm{MD1})} \xrightarrow{\text{reflection}} -\chi^{(1,\mathrm{MD1})}, \tag{2.77}$$

$$\chi^{(1,\mathrm{MD2})} \xrightarrow{\text{reflection}} -\chi^{(1,\mathrm{MD2})}. \tag{2.78}$$

These relations show that the MD1 and MD2 terms are sensitive to chirality. In experiments of the linear chiroptical spectroscopy, the goal is to obtain the value of $\chi_{XY}^{(1,\mathrm{eff})} = -\chi_{YX}^{(1,\mathrm{eff})} = -nc^{-1}(\chi^{(1,\mathrm{MD1})} - \chi^{(1,\mathrm{MD2})})$. In what follow, the way to access these values are discussed.

Given the light propagates along Z-axis, Eq. (2.29) is explicitly written as

$$-\frac{\partial^2}{\partial Z^2}\tilde{E}_X + \omega^2 c^{-2}(1+\chi^{(1,\mathrm{ED})})\tilde{E}_X - n\omega^2 c^{-3}(\chi^{(1,\mathrm{MD1})} - \chi^{(1,\mathrm{MD2})})\tilde{E}_Y = 0, \tag{2.79}$$

$$-\frac{\partial^2}{\partial Z^2}\tilde{E}_Y + \omega^2 c^{-2}(1+\chi^{(1,\mathrm{ED})})\tilde{E}_Y + n\omega^2 c^{-3}(\chi^{(1,\mathrm{MD1})} - \chi^{(1,\mathrm{MD2})})\tilde{E}_X = 0, \tag{2.80}$$

which can be rewritten in the matrix form as

$$\frac{\partial^2}{\partial Z^2}\tilde{\boldsymbol{E}} = A\tilde{\boldsymbol{E}}, \tag{2.81}$$

where

$$A = \begin{pmatrix} -\omega^2 c^{-2}(1+\chi^{(1,\mathrm{ED})}) & n\omega^2 c^{-3}(\chi^{(1,\mathrm{MD1})} - \chi^{(1,\mathrm{MD2})}) \\ -n\omega^2 c^{-3}(\chi^{(1,\mathrm{MD1})} - \chi^{(1,\mathrm{MD2})}) & -\omega^2 c^{-2}(1+\chi^{(1,\mathrm{ED})}) \end{pmatrix}. \tag{2.82}$$

Now the differential equation (2.81) is solved by diagonalizing the matrix A using a transform matrix

$$P = \frac{1}{\sqrt{2}}\begin{pmatrix} 1 & i \\ 1 & -i \end{pmatrix}. \tag{2.83}$$

The matrix A is diagonalized as

$$B = PAP^{-1} = \begin{pmatrix} k_+^2 & 0 \\ 0 & k_-^2 \end{pmatrix}, \tag{2.84}$$

with

$$k_\pm^2 = -\omega^2 c^{-2}(1+\chi^{(1,\mathrm{ED})}) \pm in\omega^2 c^{-3}(\chi^{(1,\mathrm{MD1})} - \chi^{(1,\mathrm{MD2})}). \tag{2.85}$$

In parallel, the vector representation is transformed to

$$\begin{aligned}\tilde{\boldsymbol{E}}' &= P\tilde{\boldsymbol{E}} \\ &= \frac{1}{\sqrt{2}}\begin{pmatrix} \tilde{E}_X + i\tilde{E}_Y \\ \tilde{E}_X - i\tilde{E}_Y \end{pmatrix} = \begin{pmatrix} \tilde{E}_+ \\ \tilde{E}_- \end{pmatrix}. \end{aligned} \tag{2.86}$$

Eq. (2.81) can be rewritten with a diagonal matrix as

$$\frac{\partial^2}{\partial Z^2}\tilde{\boldsymbol{E}}' = B\tilde{\boldsymbol{E}}'. \tag{2.87}$$

Here $\tilde{E}_\pm$ represent the right- and left-circularly polarized electric field. In order that the above differential equation has non-trivial solutions,

$$n^2 \pm \frac{i}{c}(\chi^{(1,\mathrm{MD1})} - \chi^{(1,\mathrm{MD2})})n - (1 + \chi^{(1,\mathrm{ED})}) = 0 \tag{2.88}$$

is required. Four solutions of this equation with respect to n is given by

$$n_{+\rightarrow} = \frac{1}{2c}\left[\sqrt{4c^2(1+\chi^{(1,\mathrm{ED})}) - (\chi^{(1,\mathrm{MD1})} - \chi^{(1,\mathrm{MD2})})} - i(\chi^{(1,\mathrm{MD1})} - \chi^{(1,\mathrm{MD2})})\right], \tag{2.89}$$

$$n_{+\leftarrow} = \frac{1}{2c}\left[-\sqrt{4c^2(1+\chi^{(1,\mathrm{ED})}) - (\chi^{(1,\mathrm{MD1})} - \chi^{(1,\mathrm{MD2})})} - i(\chi^{(1,\mathrm{MD1})} - \chi^{(1,\mathrm{MD2})})\right], \tag{2.90}$$

$$n_{-\rightarrow} = \frac{1}{2c}\left[\sqrt{4c^2(1+\chi^{(1,\mathrm{ED})}) - (\chi^{(1,\mathrm{MD1})} - \chi^{(1,\mathrm{MD2})})} + i(\chi^{(1,\mathrm{MD1})} - \chi^{(1,\mathrm{MD2})})\right], \tag{2.91}$$

$$n_{-\leftarrow} = \frac{1}{2c}\left[-\sqrt{4c^2(1+\chi^{(1,\mathrm{ED})}) - (\chi^{(1,\mathrm{MD1})} - \chi^{(1,\mathrm{MD2})})} + i(\chi^{(1,\mathrm{MD1})} - \chi^{(1,\mathrm{MD2})})\right]. \tag{2.92}$$

Here, $\rightarrow$ and $\leftarrow$ correspond to the solutions for the electromagnetic field propagating to $+Z$ and $-Z$ direction, respectively. Now the solutions propagating to $+Z$ direction are discussed and $n_{+\rightarrow}$ and $n_{-\rightarrow}$ will be simply written by n_+ and n_- in what follows. Equation (2.87) is then solved as

$$\tilde{E}_+(Z) = \tilde{E}_+(0)e^{ik_+Z}, \tag{2.93}$$

$$\tilde{E}_-(Z) = \tilde{E}_-(0)e^{ik_-Z}, \tag{2.94}$$

Above equations indicate that circularly polarized light passes through the material without mixing with the circularly polarized light with the opposite helicity. The absorption coefficient of each polarization, $\sigma_\pm$ is given by

$$\sigma_\pm = \frac{2\omega}{c}\mathrm{Im}[n_\pm]. \tag{2.95}$$

Circular dichroism is defined as the absorbance difference between left- and right-circularly polarized

light as

$$\begin{aligned}\Delta A &= \frac{Z(\sigma_- - \sigma_+)}{\ln(10)} \\ &= \frac{2Z\omega \mathrm{Im}[n_- - n_+]}{c\ln(10)} \\ &= \frac{2Z\omega}{c^2\ln(10)}\Big(\chi^{(1,\mathrm{MD1})} - \chi^{(1,\mathrm{MD2})}\Big). \end{aligned} \tag{2.96}$$

The discussion above is given with the basis set of right- and left-circularly polarized light, which corresponds to the traditional circular dichroism spectroscopy with the absorbance difference scheme.

In what follows, the basis set is converted back to the unit vectors along X- and Y-axes. Equations (2.93, 2.94) become

$$\tilde{E}_X(Z) = \tilde{E}_X(0)\Big(e^{ik_+Z} + e^{ik_-Z}\Big) + i\tilde{E}_Y(0)\Big(e^{ik_+Z} - e^{ik_-Z}\Big), \tag{2.97}$$

$$\tilde{E}_Y(Z) = -i\tilde{E}_X(0)\Big(e^{ik_+Z} - e^{ik_-Z}\Big) + \tilde{E}_Y(0)\Big(e^{ik_+Z} + e^{ik_-Z}\Big), \tag{2.98}$$

which can be rewritten in the matrix form as

$$\begin{pmatrix} \tilde{E}_X(Z) \\ \tilde{E}_Y(Z) \end{pmatrix} = \begin{pmatrix} M_{XX} & M_{XY} \\ M_{YX} & M_{YY} \end{pmatrix} \begin{pmatrix} \tilde{E}_X(0) \\ \tilde{E}_Y(0) \end{pmatrix}, \tag{2.99}$$

where

$$M_{XX} = M_{YY} = \frac{1}{2}\Big(e^{ik_+Z} + e^{ik_-Z}\Big), \tag{2.100}$$

$$M_{XY} = -M_{YX} = \frac{i}{2}\Big(e^{ik_+Z} - e^{ik_-Z}\Big). \tag{2.101}$$

Equation (2.99) relates the input electric field, $\tilde{E}_X(0)$, $\tilde{E}_Y(0)$, and the output electric field, $\tilde{E}_X(Z)$, $\tilde{E}_Y(Z)$, after passing through material with the thickness of Z. This way of representing the change of the electric field is known as Jones matrix calculus [84]. As will be presented later, the ratio M_{XY}/M_{XX} can experimentally be determined precisely. With the approximation, $e^{ik_\pm Z} \simeq 1 + ik_\pm Z$, the ratio becomes

$$\frac{M_{XY}}{M_{XX}} = \frac{Z}{2}(k_- - k_+) \tag{2.102}$$

$$= \frac{Z\omega}{2c}(n_- - n_+). \tag{2.103}$$

By comparing the above equation with Eq. (2.96), one obtains

$$\mathrm{Im}\left[\frac{M_{XY}}{M_{XX}}\right] = \frac{\ln(10)}{4}\Delta A. \tag{2.104}$$

In the linear polarization basis, CD is simply measured as $\mathrm{Im}[M_{XY}/M_{XX}]$. An important advantage of using the linear polarization over the circular polarization is that one does not need to observe the small difference as in Eq. (2.96). As a result, measurements with the linear polarization are less susceptible from fluctuation. The detailed procedure for measurement and analysis of the Jones matrix will be given in Section 3.2.

2.3.2 Second order

Although the second nonlinear processes are not used in this thesis work, it is worthwhile to briefly discuss the second order nonlinear chiroptical spectroscopy here. For an isotropic achiral liquid, the second-order nonlinear optical processes are generally prohibited due to the inversion symmetry [85]. For systems lacking the inversion symmetry such as surfaces and chiral media, the second-order nonlinear processes become allowed within the framework of the electric dipole approximation [86]. In sum-frequency generation (SFG) spectroscopy, signals originating from surfaces and chiral media can be distinguished by different polarization configurations [87].

In analogy with Eq. (2.35), the hyperpolarizability is defined as

$$\begin{aligned}\beta^{\mathrm{ED}}_{ijk}(\omega_p+\omega_q,\omega_q,\omega_p) = \frac{1}{2\hbar^2}\sum_{m,n}\Bigg[&\frac{(\mu_i)_{gn}(\mu_j)_{nm}(\mu_k)_{mg}}{(\omega_{ng}-\omega_p-\omega_q-i\Gamma_{ng})(\omega_{mg}-\omega_p-i\Gamma_{mg})}\\
&+\frac{(\mu_i)_{gn}(\mu_k)_{nm}(\mu_j)_{mg}}{(\omega_{ng}-\omega_p-\omega_q-i\Gamma_{ng})(\omega_{mg}-\omega_q-i\Gamma_{mg})}\\
&+\frac{(\mu_k)_{gn}(\mu_i)_{nm}(\mu_j)_{mg}}{(\omega_{mn}-\omega_p-\omega_q-i\Gamma_{mn})(\omega_{ng}+\omega_p+i\Gamma_{ng})}\\
&+\frac{(\mu_j)_{gn}(\mu_i)_{nm}(\mu_k)_{mg}}{(\omega_{mn}-\omega_p-\omega_q-i\Gamma_{mn})(\omega_{ng}+\omega_q+i\Gamma_{ng})}\\
&+\frac{(\mu_j)_{gn}(\mu_i)_{nm}(\mu_k)_{mg}}{(\omega_{nm}+\omega_p+\omega_q+i\Gamma_{nm})(\omega_{mg}-\omega_p-i\Gamma_{mg})}\\
&+\frac{(\mu_k)_{gn}(\mu_i)_{nm}(\mu_j)_{mg}}{(\omega_{nm}+\omega_p+\omega_q+i\Gamma_{nm})(\omega_{mg}-\omega_q-i\Gamma_{mg})}\\
&+\frac{(\mu_k)_{gn}(\mu_j)_{nm}(\mu_i)_{mg}}{(\omega_{mg}+\omega_p+\omega_q+i\Gamma_{mg})(\omega_{ng}+\omega_p+i\Gamma_{ng})}\\
&+\frac{(\mu_j)_{gn}(\mu_k)_{nm}(\mu_i)_{mg}}{(\omega_{mg}+\omega_p+\omega_q+i\Gamma_{mg})(\omega_{ng}+\omega_q+i\Gamma_{ng})}\Bigg].\end{aligned} \tag{2.105}$$

Using Eq. (2.40), the second order nonlinear susceptibility is written by

$$\chi^{(2,\mathrm{ED})}_{IJK}(\omega_p+\omega_q,\omega_q,\omega_p) = \frac{N\varepsilon_{IJK}}{6\varepsilon_0}(\beta^{\mathrm{ED}}_{xyz}+\beta^{\mathrm{ED}}_{yzx}+\beta^{\mathrm{ED}}_{zxy}-\beta^{\mathrm{ED}}_{xzy}-\beta^{\mathrm{ED}}_{yxz}-\beta^{\mathrm{ED}}_{zyx}). \tag{2.106}$$

As with the linear susceptibility including the magnetic dipole interaction, the reflection through the

xy-plane inverts the sign of the susceptibility;

$$\chi_{IJK}^{(2,\mathrm{ED})} = \frac{N\varepsilon_{IJK}}{6\varepsilon_0}(\beta_{xyz}^{\mathrm{ED}} + \beta_{yzx}^{\mathrm{ED}} + \beta_{zxy}^{\mathrm{ED}} - \beta_{xzy}^{\mathrm{ED}} - \beta_{yxz}^{\mathrm{ED}} - \beta_{zyx}^{\mathrm{ED}})$$
$$\xrightarrow{\text{reflection}} \frac{N\varepsilon_{IJK}}{6\varepsilon_0}(\beta_{yxz}^{\mathrm{ED}} + \beta_{xzy}^{\mathrm{ED}} + \beta_{zyx}^{\mathrm{ED}} - \beta_{yzx}^{\mathrm{ED}} - \beta_{xyz}^{\mathrm{ED}} - \beta_{zxy}^{\mathrm{ED}}) = -\chi_{IJK}^{(2,\mathrm{ED})}. \quad (2.107)$$

In the second-order nonlinear spectroscopy, chiroptical signal is generated within the electric dipole approximation. From Eq. (2.106), one notes that $\chi_{IJK}^{(2,\mathrm{ED})}$ is proportional to ε_{IJK}. Thus, the susceptibility vanishes unless all the electric fields have components perpendicular to each other. In an optical configuration where two incident beams co-propagate and these polarizations are perpendicular to each other, the induced polarization is parallel to the traveling direction and the emission is not constructively generated. Thus, non-collinear configuration is used in the chiral SFG experiments, where the coherence length is ~ 100 nm [88]. Although the coherence length is dependent on the incident angle of the two incoming beams, it is generally much shorter than usual third order nonlinear spectroscopy such as coherent anti-Stokes Raman scattering [89], in which the coherence length can be longer than 1 cm. Consequently the signal is relatively weak in the chiral SFG spectroscopy even though it is dipole allowed.

Chiral SFG spectroscopy resonant with vibrational transitions [90–93], electronic transitions [88, 94], and both [95, 96] has attracted attention as an emerging tool for investigating molecular chirality.

2.3.3 Third order

In this subsection, the theory is extended to the third order perturbation. Using Eq. (2.18), the third-order perturbation expansion of the density operator without the damping is expressed as

$$\rho_{I,mn}^{(3)}(t) = \left(\frac{1}{i\hbar}\right)^3 \int_{-\infty}^{t} dt_3 \int_{-\infty}^{t_3} dt_2 \int_{-\infty}^{t_2} dt_1 [H_{I,\mathrm{int}}(t_3), [H_{I,\mathrm{int}}(t_2), [H_{I,\mathrm{int}}(t_1), \rho_I^{(0)}]]]_{mn}. \quad (2.108)$$

Eq. (2.108) expresses the molecular density operator after the interactions with light which occur at t_1, t_2 and t_3. Eq. (2.108) includes 8 terms as a result of the expansion of the three commutator. These correspond to different third-order nonlinear optical processes including the coherent Stokes Raman scattering and stimulated Raman scattering. In this study, I perform chiroptical measurements using coherent anti-Stokes Raman scattering (CARS), which is derived from the term

$$\rho_{I,mn}^{(3,\mathrm{CARS})}(t) = \left(\frac{1}{i\hbar}\right)^3 \int_{-\infty}^{t} dt_3 \int_{-\infty}^{t_3} dt_2 \int_{-\infty}^{t_2} dt_1 (H_{I,\mathrm{int}}(t_3) H_{I,\mathrm{int}}(t_2) H_{I,\mathrm{int}}(t_1) \rho_I^{(0)})_{mn}. \quad (2.109)$$

So I will focus on this term in this section but the discussion below is easily applicable to optical processes originating to the other terms. By introducing the relaxation Hamiltonian, Eq. (2.109)

becomes

$$\rho_{I,mn}^{(3,\mathrm{CARS})}(t) = \left(\frac{1}{i\hbar}\right)^3 \sum_{a,b} e^{-\Gamma_{mn}t} \int_{-\infty}^{t} dt_3 (H_{\mathrm{int}}(t_3))_{mb} e^{-(\Gamma_{bn}-\Gamma_{mn})t_3} \times \int_{-\infty}^{t_3} dt_2 (H_{\mathrm{int}}(t_2))_{ba} e^{-(\Gamma_{an}-\Gamma_{bn})t_2} \times \int_{-\infty}^{t_2} dt_1 (H_{\mathrm{int}}(t_1))_{ag} \langle g|n\rangle e^{\Gamma_{an}t_1}. \quad (2.110)$$

Using Eq. (2.3), the expectation values of the third order nonlinear electric dipole moment density, magnetic dipole moment density, electric quadrupole moment density are given by

$$\langle \mu_i \rangle = N\left(\frac{1}{i\hbar}\right)^3 \sum_{a,b,c} (\mu_i)_{gc} e^{-\Gamma_{cg}t} \int_{-\infty}^{t} dt_3 (H_{\mathrm{int}}(t_3))_{cb} e^{-(\Gamma_{bg}-\Gamma_{cg})t_3} \times \int_{-\infty}^{t_3} dt_2 (H_{\mathrm{int}}(t_2))_{ba} e^{-(\Gamma_{ag}-\Gamma_{bg})t_2} \int_{-\infty}^{t_2} dt_1 (H_{\mathrm{int}}(t_1))_{ag} e^{\Gamma_{ag}t_1}, \quad (2.111)$$

$$\langle m_i \rangle = N\left(\frac{1}{i\hbar}\right)^3 \sum_{a,b,c} (m_i)_{gc} e^{-\Gamma_{cg}t} \int_{-\infty}^{t} dt_3 (H_{\mathrm{int}}(t_3))_{cb} e^{-(\Gamma_{bg}-\Gamma_{cg})t_3} \times \int_{-\infty}^{t_3} dt_2 (H_{\mathrm{int}}(t_2))_{ba} e^{-(\Gamma_{ag}-\Gamma_{bg})t_2} \int_{-\infty}^{t_2} dt_1 (H_{\mathrm{int}}(t_1))_{ag} e^{\Gamma_{ag}t_1}, \quad (2.112)$$

$$\langle Q_{ij} \rangle = N\left(\frac{1}{i\hbar}\right)^3 \sum_{a,b,c} (Q_{ij})_{gc} e^{-\Gamma_{cg}t} \int_{-\infty}^{t} dt_3 (H_{\mathrm{int}}(t_3))_{cb} e^{-(\Gamma_{bg}-\Gamma_{cg})t_3} \times \int_{-\infty}^{t_3} dt_2 (H_{\mathrm{int}}(t_2))_{ba} e^{-(\Gamma_{ag}-\Gamma_{bg})t_2} \int_{-\infty}^{t_2} dt_1 (H_{\mathrm{int}}(t_1))_{ag} e^{\Gamma_{ag}t_1}. \quad (2.113)$$

Generally, the magnitudes of the magnetic dipole moment and the electric quadrupole moment are several orders of magnitude smaller than that of the electric dipole moment. In the above expressions, the terms including the magnetic dipole and electric quadrupole moments more than twice are negligible. In Eq. (2.111), therefore, among the interaction Hamiltonians, the magnetic dipole and electric quadrupole interactions are included at most once (Fig. 2.1, (A)-(G)). In Eqs. (2.112) and (2.113), all the interaction Hamiltonians are approximated simply by the electric dipole interaction (Fig. 2.1, (H),(I)).

First, the process including only electric dipole interactions (Fig. 2.1, (A)) is considered. The expectation values of the third order nonlinear electric dipole moment density of the process (A) in

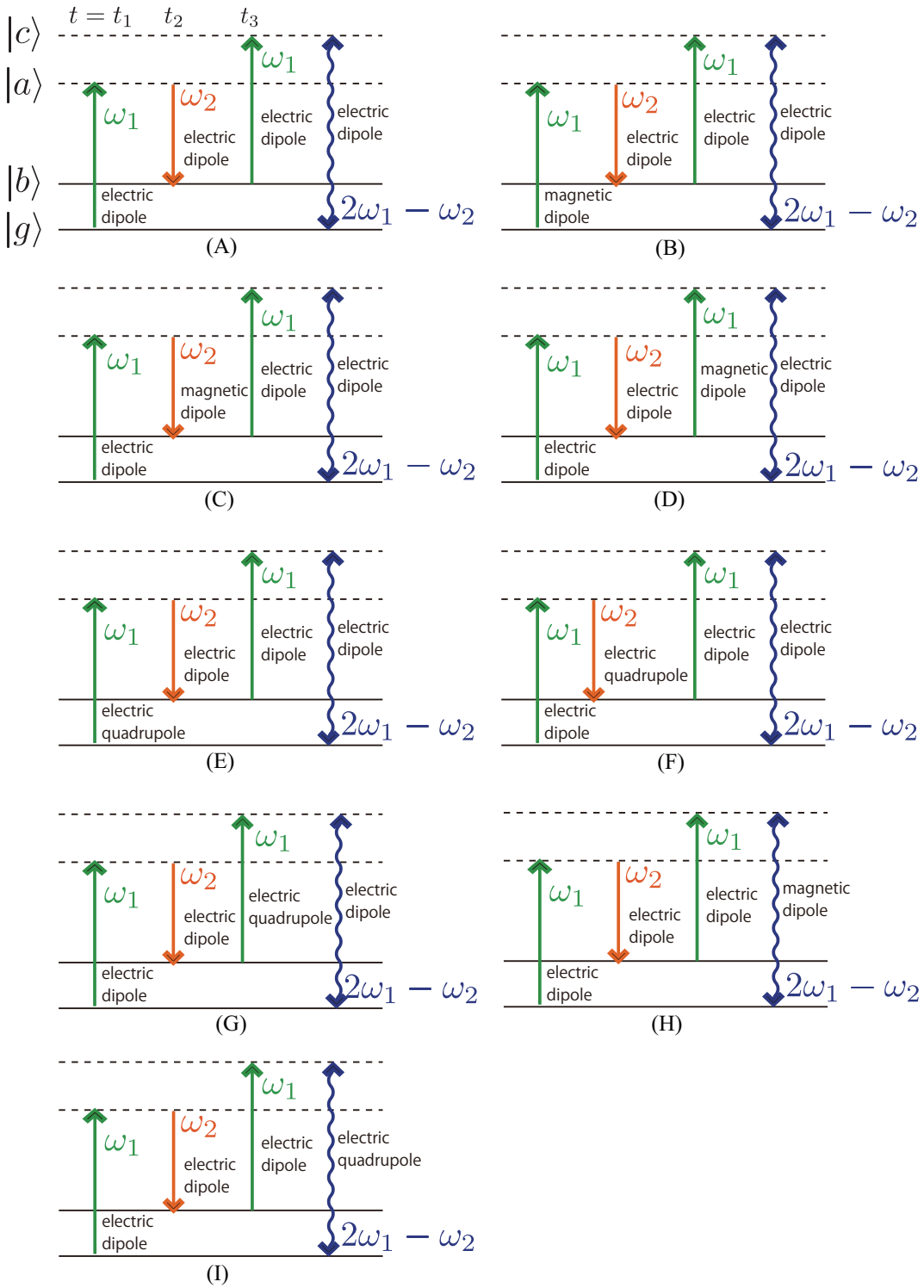

Figure 2.1: Diagrams of the CARS processes including magnetic dipole or electric quadrupole interactions.

Fig. 2.1 is given by

$$\begin{aligned}\langle\mu_i\rangle_A =& -\frac{N}{(i\hbar)^3}\sum_{a,b,c}\sum_{j,k,l}(\mu_i)_{gc}e^{-(i\omega_{cg}+\Gamma_{cg})t}\int_{-\infty}^{t}dt_3(\mu_j)_{cb}e^{-[i\omega_{bc}-(\Gamma_{bg}-\Gamma_{cg})]t_3}\\ &\times\int_{-\infty}^{t_3}dt_2(\mu_l)_{ba}e^{-[\omega_{ab}i-(\Gamma_{ag}-\Gamma_{bg})]t_2}\int_{-\infty}^{t_2}dt_1(\mu_k)_{ag}e^{-(\omega_{ga}i-\Gamma_{ag})t_1}E_j(t_3)E_l(t_2)E_k(t_1)\\ =&\frac{N}{\hbar^3}\sum_{a,b,c}\sum_{j,k,l}\frac{(\mu_i)_{gc}(\mu_j)_{cb}(\mu_l)_{ba}(\mu_k)_{ag}}{(\omega_{cg}-2\omega_1+\omega_2-i\Gamma_{cg})(\omega_{bg}-\omega_1+\omega_2-i\Gamma_{bg})(\omega_{ag}-\omega_1-i\Gamma_{ag})}\\ &\times e^{-i[(2\omega_1-\omega_2)t-(2\mathbf{k_1}-\mathbf{k_2})\cdot\mathbf{r}]}E_j(\omega_1)E_l(\omega_2)E_k(\omega_1),\end{aligned}\tag{2.114}$$

where the applied electric fields are assumed to be

$$E_i(t_1)=E_i(t_3)=E_i(\omega_1)e^{-i(\omega_1 t-\mathbf{k_1}\cdot\mathbf{r})},\tag{2.115}$$

$$E_i(t_2)=E_i(\omega_2)e^{-i(\omega_2 t-\mathbf{k_2}\cdot\mathbf{r})}.\tag{2.116}$$

The third-order nonlinear susceptibility of the electric dipole allowed CARS process in the molecular coordination system is written as

$$\chi^A_{ijkl}=\frac{N}{\hbar^3}\sum_{a,b,c}\frac{(\mu_i)_{gc}(\mu_j)_{cb}(\mu_l)_{ba}(\mu_k)_{ag}}{(\omega_{cg}-2\omega_1+\omega_2-i\Gamma_{cg})(\omega_{bg}-\omega_1+\omega_2-i\Gamma_{bg})(\omega_{ag}-\omega_1-i\Gamma_{ag})}.\tag{2.117}$$

Each molecular state is written as a product of an electronic state and a vibrational state to apply the Placzek's polarizability approximation:

$$\begin{aligned}|g\rangle=|0\rangle|0\rangle,\quad |a\rangle=|e\rangle|n_a\rangle\\ |b\rangle=|0\rangle|n\rangle,\quad |c\rangle=|e\rangle|n_c\rangle.\end{aligned}\tag{2.118}$$

As the Raman tensor is defined as

$$\alpha_{ij}(\omega)=\frac{1}{\hbar}\sum_e\frac{\langle 0|\mu_i|e\rangle\langle e|\mu_j|0\rangle}{\omega_e-\omega_0-\omega},\tag{2.119}$$

the third-order nonlinear susceptibility tensor given in Eq. (2.117) is rewritten as

$$\chi^A_{ijkl}=\frac{N}{\hbar}\frac{\langle 0|\alpha_{ij}(2\omega_1-\omega_2)|n\rangle\langle n|\alpha_{lk}(\omega_1)|0\rangle}{\omega_{bg}-\omega_1+\omega_2}.\tag{2.120}$$

When the magnetic dipole interaction is included in the CARS process, one of the μ_i and E_i in Eq. (2.114) is substituted by m_i and B_i, respectively. For example, the expectation value of the electric

dipole moment density induced by the process B is written as

$$\begin{aligned}\langle\mu_i\rangle_B =&\frac{N}{\hbar^3}\sum_{a,b,c}\sum_{j,k,l}\frac{(\mu_i)_{gc}(\mu_j)_{cb}(\mu_l)_{ba}(m_k)_{ag}}{(\omega_{cg}-2\omega_1+\omega_2-i\Gamma_{cg})(\omega_{bg}-\omega_1+\omega_2-i\Gamma_{bg})(\omega_{ag}-\omega_1-i\Gamma_{ag})}\\ &\times e^{-i[(2\omega_1-\omega_2)t-(2\mathbf{k_1}-\mathbf{k_2})\cdot\mathbf{r}]}E_j(\omega_1)E_l(\omega_2)B_k(\omega_1) \qquad (2.121)\\ =&\chi^B_{ijkl}E_j(\omega_1)E_l(\omega_2)B_k(\omega_1)e^{-i[(2\omega_1-\omega_2)t-(2\mathbf{k_1}-\mathbf{k_2})\cdot\mathbf{r}]}. \qquad (2.122)\end{aligned}$$

By defining a Raman tensor with the magnetic dipole interaction as

$$G_{ij}(\omega)=\frac{1}{\hbar}\sum_e\frac{\langle 0|\mu_i|e\rangle\langle e|m_j|0\rangle}{\omega_e-\omega_0-\omega}, \qquad (2.123)$$

the third-order nonlinear susceptibility of the process B can be written as

$$\chi^B_{ijkl}=\frac{N}{\hbar}\frac{\langle 0|\alpha_{ij}(2\omega_1-\omega_2)|n\rangle\langle n|G_{lk}(\omega_1)|0\rangle}{\omega_{bg}-\omega_1+\omega_2} \qquad (2.124)$$

χ^C and χ^D are calculated as the same way as

$$\chi^C_{ijkl}=\frac{N}{\hbar}\frac{\langle 0|\alpha_{ij}(2\omega_1-\omega_2)|n\rangle\langle n|G_{kl}(\omega_1)|0\rangle}{\omega_{bg}-\omega_1+\omega_2} \qquad (2.125)$$

$$\chi^D_{ijkl}=\frac{N}{\hbar}\frac{\langle 0|G_{ij}(2\omega_1-\omega_2)|n\rangle\langle n|\alpha_{lk}(\omega_1)|0\rangle}{\omega_{bg}-\omega_1+\omega_2}. \qquad (2.126)$$

For the case that the electric quadrupole interaction is included, one of the μ_i and E_i in Eq. (2.114) is substituted by $\theta_{\alpha i}$ and $\nabla_\alpha E_i$. Therefore, the expectation value of the electric dipole density induced by the process E is written as

$$\begin{aligned}\langle\mu_i\rangle_E =&\frac{N}{6\hbar^3}\sum_{a,b,c}\sum_{j,k,l}\frac{(\mu_i)_{gc}(\mu_j)_{cb}(\mu_l)_{ba}(\theta_{\alpha k})_{ag}}{(\omega_{cg}-2\omega_1+\omega_2-i\Gamma_{cg})(\omega_{bg}-\omega_1+\omega_2-i\Gamma_{bg})(\omega_{ag}-\omega_1-i\Gamma_{ag})}\\ &\times E_j(\omega_1)E_l(\omega_2)e^{-i[(\omega_1-\omega_2)t-(\mathbf{k_1}-\mathbf{k_2})\cdot\mathbf{r}]}\nabla_\alpha[E_k(\omega_1)e^{-i[\omega_1 t-\mathbf{k_1}\cdot\mathbf{r}]}] \qquad (2.127)\\ =&\frac{i(k_1)_\alpha}{6}\chi^E_{ij\alpha kl}E_j(\omega_1)E_l(\omega_2)E_k(\omega_1)e^{-i[(2\omega_1-\omega_2)t-(2\mathbf{k_1}-\mathbf{k_2})\cdot\mathbf{r}]}. \qquad (2.128)\end{aligned}$$

By defining a Raman tensor with the electric quadrupole interaction as

$$A_{i\alpha j}(\omega)=\frac{1}{\hbar}\sum_e\frac{\langle 0|\mu_i|e\rangle\langle e|\theta_{\alpha j}|0\rangle}{\omega_e-\omega_0-\omega} \qquad (2.129)$$

the third-order nonlinear susceptibilities of the process E,F,G can be written as

$$\chi^{E}_{ij\alpha kl} = \frac{N}{\hbar}\frac{\langle 0|\alpha_{ij}(2\omega_1-\omega_2)|n\rangle\langle n|A_{l\alpha k}(\omega_1)|0\rangle}{\omega_{bg}-\omega_1+\omega_2}, \tag{2.130}$$

$$\chi^{F}_{ijk\alpha l} = \frac{N}{\hbar}\frac{\langle 0|\alpha_{ij}(2\omega_1-\omega_2)|n\rangle\langle n|A_{k\alpha l}(\omega_1)|0\rangle}{\omega_{bg}-\omega_1+\omega_2}, \tag{2.131}$$

$$\chi^{G}_{i\alpha jkl} = \frac{N}{\hbar}\frac{\langle 0|A_{i\alpha j}(2\omega_1-\omega_2)|n\rangle\langle n|\alpha_{lk}(\omega_1)|0\rangle}{\omega_{bg}-\omega_1+\omega_2}. \tag{2.132}$$

In the same way, the expectation values of the third order nonlinear magnetic dipole moment density and electric quadrupole moment density are calculated as

$$\begin{aligned}\langle m_i\rangle_H =& \frac{N}{\hbar^3}\sum_{a,b,c}\sum_{j,k,l}\frac{(m_i)_{gc}(\mu_j)_{cb}(\mu_l)_{ba}(\mu_k)_{ag}}{(\omega_{cg}-2\omega_1+\omega_2-i\Gamma_{cg})(\omega_{bg}-\omega_1+\omega_2-i\Gamma_{bg})(\omega_{ag}-\omega_1-i\Gamma_{ag})}\\ &\times e^{-i[(2\omega_1-\omega_2)t-(2\mathbf{k_1}-\mathbf{k_2})\cdot\mathbf{r}]}E_j(\omega_1)E_l(\omega_2)E_k(\omega_1) \qquad (2.133)\\ =&\chi^{H}_{ijkl}E_j(\omega_1)E_l(\omega_2)E_k(\omega_1)e^{-i[(2\omega_1-\omega_2)t-(2\mathbf{k_1}-\mathbf{k_2})\cdot\mathbf{r}]}, \qquad (2.134)\\ \langle\theta_{\alpha i}\rangle_I =& \frac{N}{\hbar^3}\sum_{a,b,c}\sum_{j,k,l}\frac{(\theta_{\alpha i})_{gc}(\mu_j)_{cb}(\mu_l)_{ba}(\mu_k)_{ag}}{(\omega_{cg}-2\omega_1+\omega_2-i\Gamma_{cg})(\omega_{bg}-\omega_1+\omega_2-i\Gamma_{bg})(\omega_{ag}-\omega_1-i\Gamma_{ag})}\\ &\times e^{-i[(2\omega_1-\omega_2)t-(2\mathbf{k_1}-\mathbf{k_2})\cdot\mathbf{r}]}E_j(\omega_1)E_l(\omega_2)E_k(\omega_1) \qquad (2.135)\\ =&\chi^{I}_{\alpha ijkl}E_j(\omega_1)E_l(\omega_2)E_k(\omega_1)e^{-i[(2\omega_1-\omega_2)t-(2\mathbf{k_1}-\mathbf{k_2})\cdot\mathbf{r}]}, \qquad (2.136)\end{aligned}$$

where

$$\chi^{H}_{ijkl} = \frac{N}{\hbar}\frac{\langle 0|G_{ji}(2\omega_1-\omega_2)|n\rangle\langle n|\alpha_{lk}(\omega_1)|0\rangle}{\omega_{bg}-\omega_1+\omega_2} \tag{2.137}$$

$$\chi^{I}_{\alpha ijkl} = \frac{N}{\hbar}\frac{\langle 0|A_{j\alpha i}(2\omega_1-\omega_2)|n\rangle\langle n|\alpha_{lk}(\omega_1)|0\rangle}{\omega_{bg}-\omega_1+\omega_2}. \tag{2.138}$$

The total nonlinear polarization induced by above interactions is thus expressed as

$$P^{NL}_i = \sum_{X=A}^{G}\langle\mu_i\rangle_X - \frac{c}{\omega}\sum_{j,l}\varepsilon_{ijl}k_j\langle m_l\rangle_H - \frac{i}{6}\sum_j k_j\langle\theta_{ji}\rangle_I \tag{2.139}$$

$$\begin{aligned}=& \sum_{j,k,l,\alpha,\beta}\Big[\chi^{A}_{ijkl}E^1_jE^{2*}_lE^1_k + \chi^{B}_{ijkl}B^1_jE^{2*}_lE^1_k + \chi^{C}_{ijkl}E^1_jB^{2*}_lE^1_k + \chi^{D}_{ijkl}E^1_jE^{2*}_lB^1_k\\ &+\frac{i(k_1)_\alpha}{6}\chi^{E}_{i\alpha jkl}E^1_jE^{2*}_lE^1_k - \frac{i(k_2)_\alpha}{6}\chi^{F}_{ijk\alpha l}E^1_jE^{2*}_lE^1_k + \frac{i(k_1)_\alpha}{6}\chi^{G}_{ij\alpha kl}E^1_jE^{2*}_lE^1_k\\ &-\frac{c}{\omega_3}\varepsilon_{i\alpha\beta}(k_3)_\alpha\chi^{H}_{\beta jkl}E^j_1E^{*l}_2E^k_1 - \frac{i(k_3)_\alpha}{6}\chi^{I}_{\alpha ijkl}E^j_1E^{*l}_2E^k_1\Big]. \qquad (2.140)\end{aligned}$$

Here, E^1, E^2 represent $E(\omega_1), E(\omega_2)$, respectively. Magnetic field is expressed as $B_i = \sum_\alpha n\varepsilon_{jiz}E_j$, where z represents the traveling direction of the electromagnetic field. Therefore, the nonlinear polar-

ization can be written as

$$P_i^{NL} = \sum_{j,k,l,\alpha,\beta} \Big[\chi^A_{ijkl} + n_1 \varepsilon_{j\alpha z} \chi^B_{i\alpha kl} + n_2 \varepsilon_{l\alpha z} \chi^C_{ijk\alpha} + n_1 \varepsilon_{k\alpha z} \chi^D_{ij\alpha l} + \frac{i(k_1)_\alpha}{6} \chi^E_{i\alpha jkl} - \frac{i(k_2)_\alpha}{6} \chi^F_{ijk\alpha l} + \frac{i(k_1)_\alpha}{6} \chi^G_{ij\alpha kl} - n_3 \varepsilon_{iz\beta} \chi^H_{\beta jkl} - \frac{i(k_3)_\alpha}{6} \chi^I_{\alpha ijkl} \Big] E_1^j E_2^{*l} E_1^k. \tag{2.141}$$

Up to here, the discussion is given in the molecular coordinate system. What we observe experimentally is, however, the susceptibilities in the laboratory coordinates. Now, the system is changed to the laboratory coordinates system and averaged over all orientations by the use of Eqs. (2.41, 2.42). The total nonlinear polarization in the laboratory coordination is written as

$$\begin{aligned} P_I^{NL} = & \sum_{J,K,L=X,Y,Z} \frac{N}{\hbar(\omega_{bg} - \omega_1 + \omega_2 - i\Gamma)} \\ & \times \langle 0| (a^2 + \frac{\gamma^2}{45})(\delta_{IJ}\delta_{KL} + \delta_{IK}\delta_{JL}) + \frac{2}{15}\gamma^2 \delta_{IL}\delta_{JK} - i\frac{2}{15}\gamma_G^2 (n_2 - n_3)\delta_{JK}\varepsilon_{IJZ} \\ & - i(aG' + \frac{1}{45}\gamma_G^2)[(n_1 + n_2)(\delta_{IJ}\varepsilon_{KLZ} + \delta_{IJ}\varepsilon_{JLZ}) - (n_1 + n_3)(\delta_{JL}\varepsilon_{IKZ} + \delta_{KL}\varepsilon_{IJZ})] \\ & + \frac{i\gamma_A^2}{270\omega_1}[(k_1 + k_3)(\delta_{IJ}\varepsilon_{KLZ} + \delta_{IK}\varepsilon_{JLZ} - (k_1 + k_2)(\delta_{JL}\varepsilon_{IKZ} + \delta_{KL}\varepsilon_{IJZ})] |n\rangle E_1^J E_2^{L*} E_1^K, \end{aligned} \tag{2.142}$$

where tensor invariants are defined as

$$a = \frac{1}{3}(\alpha_{xx} + \alpha_{yy} + \alpha_{zz}), \tag{2.143}$$

$$\gamma^2 = \frac{1}{2}[(\alpha_{xx} - \alpha_{yy})^2 + (\alpha_{yy} - \alpha_{zz})^2 + (\alpha_{zz} - \alpha_{xx})^2], \tag{2.144}$$

$$G' = -\frac{i}{3}(G_{xx} + G_{yy} + G_{zz}), \tag{2.145}$$

$$\gamma_G^2 = \frac{i}{2}[(\alpha_{xx} - \alpha_{yy})(G_{xx} - G_{yy}) + (\alpha_{yy} - \alpha_{zz})(G_{yy} - G_{zz}) + (\alpha_{zz} - \alpha_{xx})(G_{zz} - G_{xx})], \tag{2.146}$$

$$\gamma_A^2 = \frac{3}{2}\omega_1[A_{zxy}(\alpha_{yy} - \alpha_{xx}) + A_{yzx}(\alpha_{xx} - \alpha_{zz}) + A_{xyz}(\alpha_{zz} - \alpha_{yy})]. \tag{2.147}$$

The third-order nonlinear susceptibility including not only electric dipole interactions but also magnetic dipole and electric quadrupole interactions are thus given in the form of

$$\chi^{(3,\mathrm{eff})}_{IJKL} = \chi^{\mathrm{NR}}_{IJKL} + \frac{NR_{IJKL}}{\Omega - \omega_1 + \omega_2 - i\Gamma}, \tag{2.148}$$

where

$$
\begin{aligned}
R_{IJKL} =& \langle 0|(a^2 + \frac{\gamma^2}{45})(\delta_{IJ}\delta_{KL} + \delta_{IK}\delta_{JL}) + \frac{2}{15}\gamma^2\delta_{IL}\delta_{JK} - i\frac{2}{15}\gamma_G^2(n_2 - n_3)\delta_{JK}\varepsilon_{ILZ} \\
& - i(aG' + \frac{1}{45}\gamma_G^2)[(n_1 + n_2)(\delta_{IJ}\varepsilon_{KLZ} + \delta_{IK}\varepsilon_{JLZ}) - (n_1 + n_3)(\delta_{JL}\varepsilon_{IKZ} + \delta_{KL}\varepsilon_{IJZ})] \\
& + \frac{i\gamma_A^2}{270\omega_1}[(k_1 + k_3)(\delta_{IJ}\varepsilon_{KLZ} + \delta_{IK}\varepsilon_{JLZ} - (k_1 + k_2)(\delta_{JL}\varepsilon_{IKZ} + \delta_{KL}\varepsilon_{IJZ})]|n\rangle/\hbar.
\end{aligned}
\tag{2.149}
$$

In CARS measurements, as the difference among ω_1, ω_2 and ω_3 is less than 10000 cm^{-1}, the differences of refractive indices at each wavelength can be neglected. Under the approximation $n_1 = n_2 = n_3 = n$, Eq. (2.149) becomes simpler form as

$$
\begin{aligned}
R_{IKJL} =& \frac{1}{\hbar}\Big\langle 0\Big|\Big(a^2 + \frac{\gamma^2}{45}\Big)(\delta_{IJ}\delta_{KL} + \delta_{IK}\delta_{JL}) + \frac{2}{15}\gamma^2\delta_{IL}\delta_{JK} \\
& - 2in\Big(aG' + \frac{1}{45}\gamma_G^2\Big)[(\delta_{IJ}\varepsilon_{KLZ} + \delta_{IK}\varepsilon_{JLZ}) - (\delta_{JL}\varepsilon_{IKZ} + \delta_{KL}\varepsilon_{IJZ})] \\
& + \frac{in\gamma_A^2}{135\omega_1}\Big[\Big(1 + \frac{\omega_1 - \omega_2}{2\omega_1}\Big)(\delta_{IJ}\varepsilon_{KLZ} + \delta_{IK}\varepsilon_{JLZ}) \\
& \qquad - \Big(1 - \frac{\omega_1 - \omega_2}{2\omega_1}\Big)(\delta_{JL}\varepsilon_{IKZ} + \delta_{KL}\varepsilon_{IJZ})\Big]\Big|n\Big\rangle.
\end{aligned}
\tag{2.150}
$$

For isotropic achiral media, the tensor invariants G', γ_G, γ_A vanish. Therefore, there are only two independent tensor elements:

$$R_{XXXX} = R_{YYYY} = 2\Big(a^2 + \frac{4}{45}\gamma^2\Big), \tag{2.151}$$

$$R_{XYYX} = R_{YXXY} = \frac{2}{15}\gamma^2, \tag{2.152}$$

$$R_{XXYY} = R_{YYXX} = R_{XYXY} = R_{YXYX} = \frac{1}{2}(R_{XXXX} - R_{XYYX}). \tag{2.153}$$

For isotropic chiral media, on the other hand, the tensor invariants G', γ_G, γ_A do not vanish and two more elements of R_{IJKL} become non-zero;

$$R_{XXXY} = -R_{YYYX} = -4in\Big[aG' + \frac{\gamma_G^2}{45} - \Big(1 + \frac{\omega_1 - \omega_2}{2\omega_1}\Big)\frac{\gamma_A^2}{270c}\Big], \tag{2.154}$$

$$R_{XYYY} = -R_{2111} = 4in\Big[aG' + \frac{\gamma_G^2}{45} - \Big(1 - \frac{\omega_1 - \omega_2}{2\omega_1}\Big)\frac{\gamma_A^2}{270c}\Big], \tag{2.155}$$

$$R_{XYXX} = R_{XXYX} = -R_{YXYY} = -R_{YYXY} = \frac{1}{2}(R_{XYYY} - R_{XXXY}). \tag{2.156}$$

In spontaneous ROA experiments, the dimensionless circular intensity difference (CID) is mea-

sured. CID is defined as

$$\Delta(\xi) = \frac{I_R(\xi) - I_L(\xi)}{I_R(\xi) + I_L(\xi)}. \tag{2.157}$$

Here, $I_R(\xi)$ and $I_L(\xi)$ are the Raman intensities obtained with right- and left-circularly polarized incident light in the scattering angle ξ. The CIDs for backward ($\xi = 180°$) and forward ($\xi = 0°$) are written in terms of the tensor invariants [97]:

$$\Delta(180°) = \frac{48n(\gamma_G^2 + \gamma_a^2/18c)}{45a^2 + 7\gamma^2}, \tag{2.158}$$

$$\Delta(0°) = \frac{4n(45aG' + \gamma_G^2 - \gamma_A^2/6c)}{45a^2 + 7\gamma^2}. \tag{2.159}$$

By comparing Eqs. (2.155) and (2.159), R_{YXXX} is approximated by the product of $\Delta(0°)$ and R_{XXXX} as

$$R_{YXXX} \simeq -\frac{i}{2}\Delta(0°)R_{XXXX} \tag{2.160}$$

In this research, I concentrate on detecting $\chi^{(3,\mathrm{eff})}_{YXXX} = \chi^{\mathrm{NR}}_{YXXX} + \dfrac{NR_{YXXX}}{2\hbar(\Omega - \omega_1 + \omega_2 - i\Gamma)}$ as a chirality sensitive value. Detailed experimental procedure for extracting R_{YXXX} will be given in Section 5.2.

Part II

Femtosecond time-resolved CD spectroscopy

Chapter 3

Development of broadband and sensitive femtosecond time-resolved dichroism and birefringence spectroscopy

3.1 Introduction

Time-resolved circular dichroism (TRCD) spectroscopy has great potential as a powerful tool for investigating three-dimensional structural evolution during the reactions of chiral chemical species [98–100] and biomolecules [67, 101, 102]. However, TRCD measurement remains a great challenge, mainly because of the extremely low signal intensity.

To date, ultrafast TRCD instruments have been developed by several groups [68, 70, 103]. They are roughly classified into two categories, depending on their measurement schemes: difference absorption measurement and ellipticity measurement. In the former scheme, a small difference in absorbance between right- and left-circularly polarized light, which is typically less than 10^{-3} of the total absorbance, is measured as is the case in conventional steady-state CD spectroscopy [68]. The sensitivity of this straightforward method is limited by power fluctuation of the light source because the noise of the TRCD signal is primarily determined by intensity fluctuation of the huge achiral background. In addition, in a pump-probe experiment, the measurement is susceptible to artifacts due to linear birefringence (LB) and/or linear dichroism (LD) induced by pump radiation [104].

In the early development stage of the time-resolved difference absorption method, single wavelength radiation was employed as the probe light [68]. Recently, Trifonov et al. have developed a broadband TRCD spectrometer, where a white-light continuum (WLC) generated by self-phase modulation was employed as a light source [103]. While broadband TRCD measurements can provide rich spectral information in the frequency domain, the difficulty in polarization control, attributed mainly to

the strong wavelength dependence of the polarization property of optical components, prevents precise CD measurement across the whole spectral region. On that account, broadband TRCD measurement has been made only for a sample providing strong a TRCD signal of $>$50 mdeg [103].

In the ellipticity measurements, linearly-polarized or slightly elliptically-polarized light is employed as the probe light; CD is measured by monitoring the change in the ellipticity and azimuth of the transmitted light, usually by the use of a strain plate or a Babinet-Soleil (BS) compensator [67, 70]. In this method, only small portion of the probe light reaches the detector because most of the achiral background is reflected at the polarization analyzer located after the sample, which drastically increases the signal to background ratio of the CD measurement. Nevertheless, this type of TRCD measurements using a BS compensator is only practicable at a single wavelength due to the strong wavelength-dependent behavior of the phase retarder [70, 74, 100].

Recently, Eom *et al.* have developed new methods for ellipticity measurement employing the heterodyne-detection technique [72, 105]. They successfully obtained the steady-state CD and optical rotatory dispersion (ORD) spectra of Ni-(tartrate)$_2$ by measuring the relative phase and amplitude of the transmitted electric field perpendicular to the incident polarization. They also referred to the advantages of the technique for time-resolved CD or ORD applications; however no such an attempt has yet been made probably because one has to overcome difficult obstacles in implementing the technique to achieve precise TRCD measurements.

In this Chapter, I report the development of TRCD spectroscopy by the heterodyne detection, which covers almost the whole visible range of 415 - 730 nm with a sensitivity much higher than previously obtained ($<$ 0.4 mdeg). Change of the polarization state by the sample is characterized by measuring the phase and amplitude of the transmitted electric field by the spectral interferometry. The setup developed here is used for measurements not only of time-resolved CD/ORD but also of time-resolved LD/LB by employing different polarization angles.

3.2 Method

3.2.1 Jones matrix calculus

For investigating the polarization change by passing through the sample, it is convenient to use the Jones matrix calculus, in which the polarization state of the light is described by a two-dimensional complex vector. When the electric field propagating in the z-direction is written by (see Fig. 3.2 for the definition of the coordinates[1])

$$E(z,t) = \tilde{E}_x e^{-i(\omega t - kz)} + \tilde{E}_y e^{-i(\omega t - kz)}, \tag{3.1}$$

[1]Here, x, y, z indicate the laboratory coordinate. It should be noted that the notation is different from Chapter 2, where X, Y, Z are used for the laboratory coordinates.

the Jones vector is defined by

$$J = \begin{bmatrix} \tilde{E}_x \\ \tilde{E}_y \end{bmatrix}. \tag{3.2}$$

Here, the absolute magnitudes and the arguments of $\tilde{E}_x$ and $\tilde{E}_y$ represent the amplitude and the relative phase of the electric field in x and y direction, respectively.

Polarization change induced by various optical components is represented by multiplication of 2×2 Jones matrices. Those of CD, ORD, LD, and LB are given by [101]

$$M_{\mathrm{CD}} = \frac{1}{2} \begin{bmatrix} k_R + k_L & -i(k_R - k_L) \\ i(k_R - k_L) & k_R + k_L \end{bmatrix}, \tag{3.3}$$

$$M_{\mathrm{ORD}} = \begin{bmatrix} \cos\delta & -\sin\delta \\ \sin\delta & \cos\delta \end{bmatrix}, \tag{3.4}$$

$$M_{\mathrm{LD}} = \begin{bmatrix} k_x & 0 \\ 0 & k_y \end{bmatrix}, \tag{3.5}$$

$$M_{\mathrm{LB}} = \begin{bmatrix} e^{-i\rho} & 0 \\ 0 & e^{i\rho} \end{bmatrix}. \tag{3.6}$$

In the expression, k_R, k_L, k_x and k_y are the square root of the transmittance of right circularly, left circularly, x- and y-polarized light and δ and ρ are the phase retardation between right- and left-circularly polarized light and x- and y-polarized light, respectively. Eqs. (3.5, 3.6) are the Jones matrices for LD and LB when the optical axis is x or y direction. More generally, the Jones matrices for LD and LB with the optical axis tilted by ϕ are written by

$$\begin{aligned} M_{\mathrm{LD}}(\phi) &= R(\phi) M_{\mathrm{LD}} R(-\phi) \\ &= \begin{bmatrix} k_x \cos^2\phi + k_y \sin^2\phi & (k_x - k_y)\cos\phi\sin\phi \\ (k_x - k_y)\cos\phi\sin\phi & k_x \sin^2\phi + k_y \cos^2\phi \end{bmatrix}, \end{aligned} \tag{3.7}$$

$$\begin{aligned} M_{\mathrm{LB}}(\phi) &= R(\phi) M_{\mathrm{LB}} R(-\phi) \\ &= \begin{bmatrix} e^{-i\rho}\cos^2\phi + e^{i\rho}\sin^2\phi & (e^{-i\rho} - e^{i\rho})\cos\phi\sin\phi \\ (e^{-i\rho} - e^{i\rho})\cos\phi\sin\phi & e^{-i\rho}\sin^2\phi + e^{i\rho}\cos^2\phi \end{bmatrix}, \end{aligned} \tag{3.8}$$

where $R(\phi)$ is the rotation matrix,

$$R(\phi) = \begin{bmatrix} \cos\phi & -\sin\phi \\ \sin\phi & \cos\phi \end{bmatrix}. \tag{3.9}$$

When the linearly polarized light is used as the pump radiation, the angle of the induced anisotropy, ϕ,

is the same as the polarization angle of the pump radiation.

Polarization change by successive optical components is written by multiplying the corresponding matrices in the order of the interaction. When one optical component has more than two polarization properties, the product express the total polarization change if they commute. For example, the Jones matrix for the optical component possessing CD and ORD can be written by

$$\begin{aligned} M_{\mathrm{CD,ORD}} &= M_{\mathrm{CD}} M_{\mathrm{ORD}} \\ &= M_{\mathrm{ORD}} M_{\mathrm{CD}} \\ &= \frac{1}{2} \begin{bmatrix} k_R e^{-i\delta} + k_L e^{i\delta} & -i(k_R e^{-i\delta} - k_L e^{i\delta}) \\ i(k_R e^{-i\delta} - k_L e^{i\delta}) & k_R e^{-i\delta} + k_L e^{i\delta} \end{bmatrix}. \end{aligned} \tag{3.10}$$

The above Jones matrix is the same as Eq. (2.99) in Section 2.3, which was derived for the isotropic chiral system. When the incident field is polarized in the x-direction, the Jones vector for the output radiation becomes

$$J_{\mathrm{out}} = M_{\mathrm{CD,ORD}} \begin{bmatrix} E_0 \\ 0 \end{bmatrix} \tag{3.11}$$

$$= E_0 \begin{bmatrix} k_R e^{-i\delta} + k_L e^{i\delta} \\ i(k_R e^{-i\delta} - k_L e^{i\delta}) \end{bmatrix} = \begin{bmatrix} \tilde{E}_{\mathrm{out},x} \\ \tilde{E}_{\mathrm{out},y} \end{bmatrix}, \tag{3.12}$$

$$\tag{3.13}$$

where E_0 is amplitude of the incident field. As seen in Eq. (2.104), by calculating the ratio of $\tilde{E}_{\mathrm{out},y}$ to $\tilde{E}_{\mathrm{out},x}$, CD and ORD can be extracted in the imaginary and real parts as

$$\frac{\tilde{E}_{\mathrm{out},y}}{\tilde{E}_{\mathrm{out},x}} = \delta + i\frac{k_R - k_L}{k_R + k_L}. \tag{3.14}$$

If one optical component has more than two polarization properties and their Jones matrices do not commute, the matrix for the component cannot be simply expressed by the product of the each matrix. In order to calculate the Jones matrix for the net polarization change, N-matrix method is generally used [106]. In the N-matrix method [101,106], the total Jones matrix is calculated via N-matrix, which is defined as

$$N = \frac{dM}{dz} M^{-1}. \tag{3.15}$$

If the sample is homogeneous along z-direction, Eq. (3.15) can be formally solved as

$$M = \exp(Nz). \tag{3.16}$$

From Eq. (3.16), the Jones matrix for infinitely thin layer can be approximated by

$$M \simeq 1 + Nz. \tag{3.17}$$

Thus, the Jones matrix for multiple infinitely thin layers can be written as

$$\prod_i M_i \simeq 1 + z \sum_i N_i, \tag{3.18}$$

where i indicates the index of the layers. This equation means, in the N-matrix representation, one does not need to care about the order of interaction. For the calculation of the Jones matrix of the optical component with more than two polarization properties, therefore, one can simply calculate the total N-matrix by summing N-matrices of each property and then the total Jones matrix is calculated from the total N-matrix using Eq. (3.16).

The N-matrices corresponding to Eqs. (3.3, 3.4, 3.7, 3.8) are

$$N_{\mathrm{CD}} = \frac{1}{2z} \begin{bmatrix} \ln k_R + \ln k_L & -i(\ln k_R - \ln k_L) \\ i(\ln k_R - \ln k_L) & \ln k_R + \ln k_L \end{bmatrix}, \tag{3.19}$$

$$N_{\mathrm{ORD}} = \frac{\delta}{z} \begin{bmatrix} 0 & -1 \\ 1 & 0 \end{bmatrix}, \tag{3.20}$$

$$N_{\mathrm{LD}}(\phi) = \frac{1}{z} \begin{bmatrix} \ln k_x \cos^2\phi + \ln k_y \sin^2\phi & (\ln k_x - \ln k_y)\cos\phi\sin\phi \\ (\ln k_x - \ln k_y)\cos\phi\sin\phi & \ln k_x \sin^2\phi + \ln k_y \cos^2\phi \end{bmatrix}, \tag{3.21}$$

$$N_{\mathrm{LB}}(\phi) = -\frac{i\rho}{z} \begin{bmatrix} \cos^2\phi - \sin^2\phi & 2\cos\phi\sin\phi \\ 2\cos\phi\sin\phi & \sin^2\phi - \cos^2\phi \end{bmatrix}. \tag{3.22}$$

Given the N matrix

$$N = \begin{bmatrix} n_1 & n_2 \\ n_3 & n_4 \end{bmatrix}, \tag{3.23}$$

equation (3.16) can be explicitly rewritten as

$$M = e^{Tz} \begin{bmatrix} \cosh(Q'z) + \frac{1}{2Q'}(n_1 - n_4)\sinh(Q'z) & \frac{n_3}{Q'}\sinh(Q'z) \\ \frac{n_2}{Q'}\sinh(Q'z) & \cosh(Q'z) - \frac{1}{2Q'}(n_1 - n_4)\sinh(Q'z) \end{bmatrix}, \tag{3.24}$$

where

$$T = \frac{n_1 + n_4}{2}, \tag{3.25}$$

$$Q' = \sqrt{\frac{1}{4}(n_1 - n_4)^2 + n_2 n_3}. \tag{3.26}$$

With the N-matrices in Eqs. (3.19-3.22), the total Jones matrix representing all of LD, LB, CD, and ORD becomes

$$M_{\mathrm{tot}}(\phi) = \begin{bmatrix} m_1 & m_2 \\ m_3 & m_4 \end{bmatrix}, \tag{3.27}$$

with

$$m_1 = \cosh Q + (\sin^2\phi - \cos^2\phi)(\beta - i\rho)\frac{\sinh Q}{Q}, \tag{3.28}$$

$$m_2 = -\Big[2\cos\phi\sin\phi(\beta - i\rho) + (\delta + i\gamma)\Big]\frac{\sinh Q}{Q}, \tag{3.29}$$

$$m_3 = -\Big[2\cos\phi\sin\phi(\beta - i\rho) - (\delta + i\gamma)\Big]\frac{\sinh Q}{Q}, \tag{3.30}$$

$$m_4 = \cosh Q - (\sin^2\phi - \cos^2\phi)(\beta - i\rho)\frac{\sinh Q}{Q}, \tag{3.31}$$

where

$$\beta = 2(\ln k_x - \ln k_y), \tag{3.32}$$

$$\gamma = 2(\ln k_L - \ln k_R), \tag{3.33}$$

$$Q = \sqrt{(\beta - i\rho)^2 + (\delta + i\gamma)^2}. \tag{3.34}$$

Equation (3.27) is a general form of Jones matrix which expresses all of LD, LB, CD, and ORD. What is experimentally observed for such a sample will be discussed in the following sections.

3.2.2 Heterodyne-detected dichroism and birefringence measurement

In the present study, linearly-polarized radiation, with polarization angle θ from the x-axis, is employed as the incident probe light. As will be shown in Section 3.2.4, the quantity experimentally measured in Fourier transform spectral interferometry (FTSI) [107] is

$$F_{x,y}(\omega, \theta, \tau) = \tilde{E}_{x,y}(\omega, \theta)\tilde{E}^{\mathrm{LO}*}_{x,y}(\omega)\exp(-i\omega\tau), \tag{3.35}$$

where $\tilde{E}_{x,y}(\omega, \theta)$ and $\tilde{E}^{\mathrm{LO}}_{x,y}(\omega)$ express the electric field of the signal and the local oscillator(LO), respectively, and τ is the temporal delay between $\tilde{E}_{x,y}(\omega, \theta)$ and $\tilde{E}^{\mathrm{LO}}_{x,y}(\omega)$. As seen in Eq. (3.14),

when a chiral liquid or solution is employed as the target object, one can simply calculate CD and ORD from the quantity $\alpha(\omega)$ defined as

$$\begin{aligned}\alpha(\omega) &= \frac{2\theta_0 S(\omega,0)}{S(\omega,\theta_0)-S(\omega,-\theta_0)} \\ &\simeq \delta + i\frac{k_R-k_L}{k_R+k_L},\end{aligned} \tag{3.36}$$

where

$$S(\omega,\theta) = \frac{F_y(\omega,\theta,\tau)}{F_x(\omega,\theta,\tau)}, \tag{3.37}$$

with a fixed polarization angle, θ_0. As $(k_R-k_L)/(k_R+k_L)$ and δ in Eq. (3.36) respectively correspond to CD and ORD, one can readily obtain CD and ORD spectra.

When the sample is photoexcited in TRCD measurements, LD and/or LB associated with photoinduced anisotropy should be taken into consideration in addition to CD and ORD, where the total Jones matrix is represented by Eq. (3.27). This leads to a situation in which the real (imaginary) part of $\alpha(\omega)$ does not simply correspond to ORD (CD). I have performed a model calculation of $\alpha(\omega)$ by using Eq. (3.27) with hypothetical, but realistically presumed, CD, ORD, LD, and LB spectra in order to estimate how LD and LB have a controversial influence on the CD and ORD measurement. With Eq. (3.27), $\alpha(\omega)$ spectra are calculated as

$$\alpha(\omega) = \frac{2\theta_0 S(\omega,0)}{S(\omega,\theta_0)-S(\omega,-\theta_0)} \tag{3.38}$$

$$= \frac{\theta_0 m_3(m_3^2\cos^2\theta_0 - m_2^2\sin^2\theta_0)}{m_1\sin\theta_0\cos\theta_0(m_1m_4-m_2m_3)}. \tag{3.39}$$

Calculated spectra of $\alpha(\omega)$ are shown in Fig. 3.1.

As shown in Fig. 3.1, the imaginary part of the calculated $\alpha(\omega)$, $\mathrm{Im}[\alpha(\omega)]$, is roughly reproduced by the linear combination of CD and LB, and the real part, $\mathrm{Re}[\alpha(\omega)]$, by that of ORD and LD. The contribution of LB and LD is nearly proportional to the angle between the pump and probe polarizations, ϕ. The model calculations, however, also reveal that $\mathrm{Im}[\alpha(\omega)]$ deviates significantly from CD and the same goes for $\mathrm{Im}[\alpha(\omega)]$ vs. CD even when the pump and probe polarizations are set to be parallel ($\phi = 0$). These deviations can be approximated by $LD \times CD - LB \times ORD$ for the imaginary part and $-LD \times ORD - LB \times CD$ for the real part (see Fig. 3.1). In the measurements of time-resolved CD and ORD, therefore, signals originating from anisotropy are generally superposed in $\alpha(\omega)$ spectra and great care is needed in handling the obtained data.

The discrepancy between the genuine CD/ORD and $\mathrm{Im}/\mathrm{Re}[\alpha(\omega)]$ spectra at $\theta = 0$ is explained also by analytical calculation. With the assumptions of $\theta_0 \ll \pi, \delta \ll \beta, \gamma \ll \rho$, and $Q \ll 1$, Eq. (3.39)

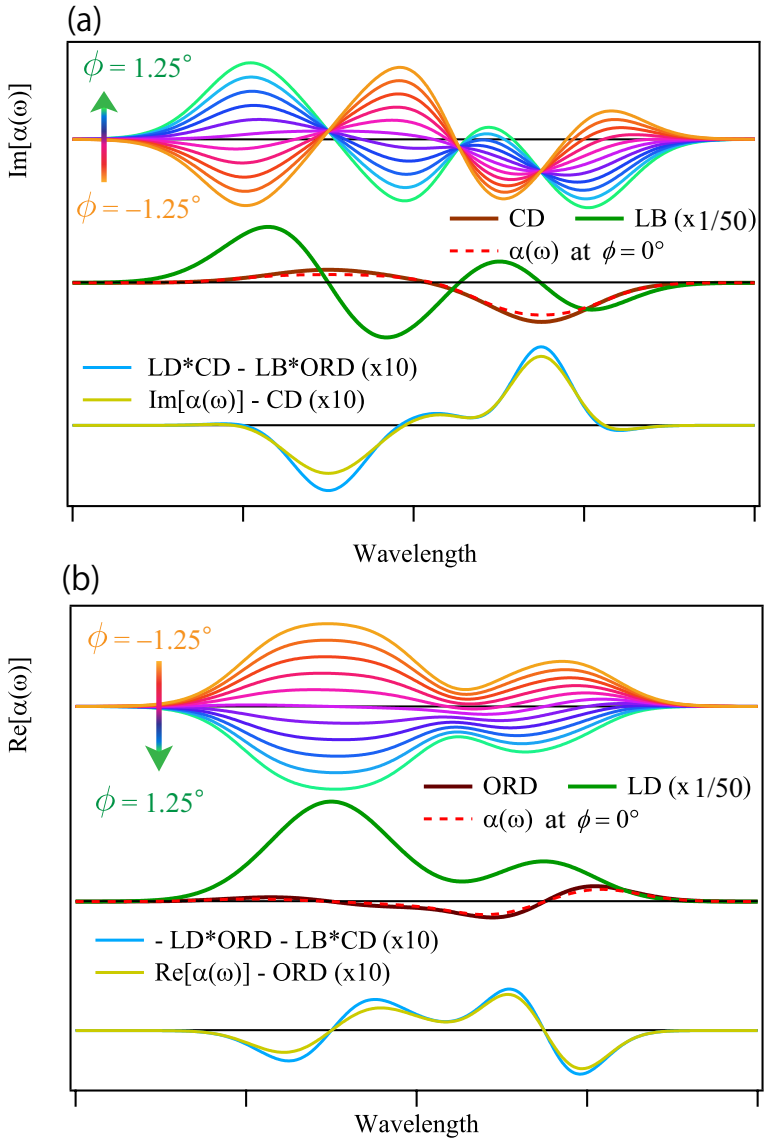

Figure 3.1: Simulated spectra of the (a) imaginary and (b) real part of the $\alpha(\omega)$ spectra(top) with different pump polarization angle ϕ. Hypothetical spectra of the CD, LB, ORD, and LD of the sample are shown in the middle part of the figures. At the bottom of the figures, the difference between the CD/ORD and $\alpha(\omega)$ spectra are shown.

is approximated by

$$\alpha(\omega) \simeq (\delta + i\gamma)(1 - \beta + i\rho) \tag{3.40}$$

$$= \delta - \delta\beta - \gamma\rho + i(\gamma + \delta\rho - \gamma\beta). \tag{3.41}$$

As shown in Fig. 3.1 in the main text, the obtained spectra are significantly distorted when the system has LD and/or LB. The difference between the spectrum of $\mathrm{Im}[\alpha(\omega)]$ calculated by N-matrix method and the true CD spectrum is approximated by $\delta\rho - \gamma\beta$,viz., $LB \times ORD - LD \times CD$ and that between $\mathrm{Re}[\alpha(\omega)]$ and ORD is approximated by $-\delta\beta - \gamma\delta$,viz., $-LD \times ORD - LB \times CD$.

As will be discussed in Section 3.3.4, this issue can be circumvented by taking advantage of broad-band measurements of $\alpha(\omega)$. A large quantity of the time- and wavelength-resolved $\alpha(\omega)$, which are experimentally obtained by heterodyne-detected ellipticity measurements, are analyzed by the singular value decomposition (SVD). In the SVD analysis, a series of time-resolved $\alpha(\omega)$ spectra are well decomposed into genuine transient CD/ORD components and the anisotropic components, $LD \times CD - LB \times ORD$ and $-LD \times ORD - LB \times CD$ for the imaginary and real parts, respectively.

3.2.3 Apparatus and sample preparation

The optical setup of our heterodyne-detected femtosecond dichroism and birefringence spectrometer is shown in Fig. 3.2. A Ti:Sapphire regenerative amplifier (Integra-C, Quantronix) is used as a light source. The output of the amplifier (785 nm, 1 kHz, 2.2 mJ) is divided into pump and probe pulses. The pump pulse is obtained by frequency conversion such as the second harmonic generation (SHG) or the optical parametric amplification (OPA). In the proof of principle experiment using $Ru(bpy)_3^{2+}$ as a sample, SH at 393 nm generated by LiB_3O_5 crystal is employed as the pump light. The pump radiation is focused into the sample after passing through an optical delay and a Gran-Taylor polarizer. For the probe pulse, WLC is generated by the self-phase modulation (SPM). The WLC beam is divided into two so that they constitute a Mach-Zehnder interferometer; one is used as a probe and the other is used as a LO. The probe polarization is set at an angle θ with the x axis by a Glan-Taylor (GT) prism mounted on a stepper-motor driven rotational stage, which is placed just before the sample. Here, the x- and y-coordinates are parallel to the polarization of the reflected and transmitted light of the GT prism after the sample, respectively. The polarization of the LO is set to be linear and slightly tilted from x axis in order that the phase of the x- and y-polarization may be identical. The probe light is recombined with the LO with optical delay τ, which is modulated using a piezo stage. The combined light is separated into x- and y-polarized light by the GT prism and their spectra are measured simultaneously in different lines of the CCD camera.

The pulse width of the probe and LO are elongated to $\sim$2.5 ps primarily due to the dispersion of

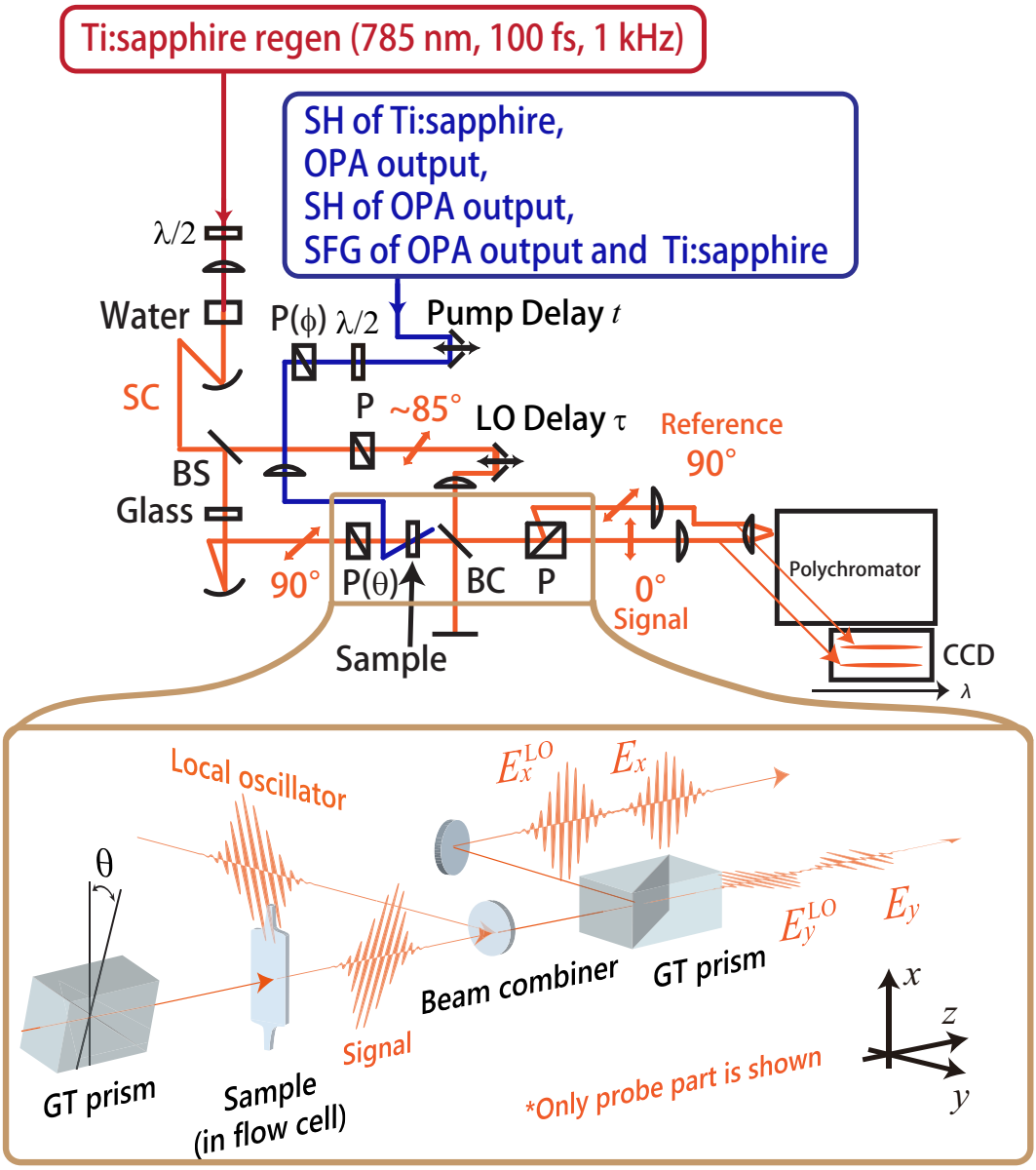

Figure 3.2: Experimental setup of the heterodyne-detected femtosecond TRCD spectrometer . BS: beam splitter, BC: beam combiner, $\lambda/2$: half wave plate, P: polarizer, PZT: piezoelectric stage

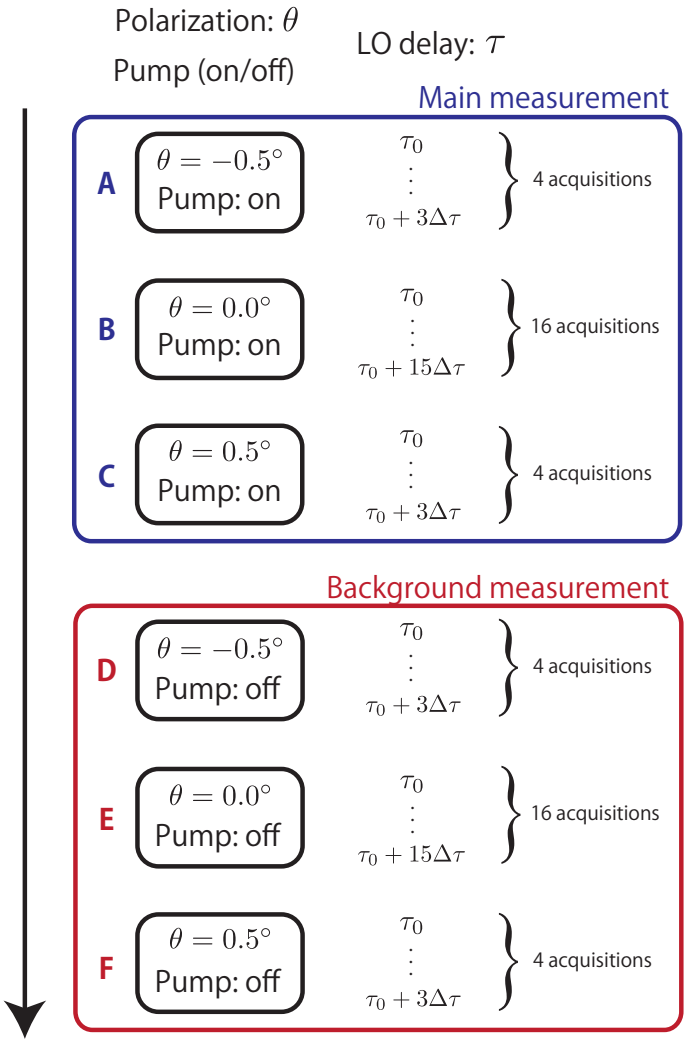

Figure 3.3: Protocol of measuring the time-resolved dichroism and birefringence spectra.

the polarizer. For measurements of dynamics faster than 2.5 ps, therefore, chirp compensation is done by measuring the pulse shape using the optical Kerr effect. The time resolution is estimated to be less than 400 fs in the measured wavelength range after the chirp compensation.

In this study, first, time-resolved LD/LB measurements were performed on an ethanolic solution of 3,3'-diethyloxadicarbocyanine iodide (DODCI) with the excitation wavelength at 550 nm. Then, I performed time-resolved CD/ORD measurements on Δ- and Λ-Ru(bpy)$_3^{2+}$ as a proof-of-principle. Racemic Ru(bpy)$_3$Cl$_2$ was purchased from Aldrich and optically resolved by the procedure given in Ref. [108]. The enantiomeric separation was confirmed by measuring CD spectrum of each sample with a commercial CD spectrometer. Measurements below are made for 1 mg/mL aqueous solution of Δ- and Λ-Ru(bpy)$_3$Br$_2$.

3.2.4 Procedure to extract dichroism and birefrengence spectra

In the conventional FTSI procedure, a better separation of the heterodyne term from the homodyne terms in time domain is achieved by performing measurements with a larger τ value. The modulation depth decreases, however, with increasing τ value, due to the limited coherence length. Thus, the separation and the modulation depth are in a trade-off relationship. In order to overcome this difficulty, in this study, measurements were performed with several different τ values at sub-wavelength intervals within the coherence length, and the heterodyne term is further separated by filtering out the homodyne terms in the reciprocal space of τ. The extraction of the heterodyne terms $F_{x,y}(\omega, \theta)$ is done as follows.

The sequence of each measurement is summarized in Fig. 3.3. In the current scheme, one set of measurement at a single delay consists of 48 acquisitions of spectra. The dichroism and birefringence spectra with and without the pump radiation are obtained from 24 acquisitions of the first and second halves. In each half, the initial and final four acquisition are performed at $\theta = -0.5^\circ$ (A,D in Fig. 3.3) and 0.5° (C, F) to obtain $S(\omega, -0.5^\circ)$ and $S(\omega, 0.5^\circ)$, respectively. The middle 16 acquisitions are performed at $\theta = 0.0^\circ$ (B, D) to obtain $S(\omega, 0.0^\circ)$. The acquisitions at each θ are performed with different LO delays, which is modulated as

$$\tau = \tau_0 + n\Delta\tau, \tag{3.42}$$

where n indicates the data number. The measurements at $\theta = 0.0^\circ$ are performed with the greater number of acquisitions because the observed fringe is much weaker than those obtained at $\theta = \pm 0.5^\circ$. What is done for extracting $S(\omega, \theta)$ is the same for these three processes (A, B, C in Fig. 3.3). So the procedure is demonstrated below for a series of spectra at $\theta = 0.0^\circ$ and 10 ps after the photoexcitation of DODCI with the pump polarization, $\phi = 2.5^\circ$.

The spectrum obtained at τ is formulated by

$$\begin{aligned}
\tilde{I}_{x,y}(\omega, \theta, n) &= |\tilde{E}_{x,y}(\omega, \theta) + \tilde{E}^{\mathrm{LO}}_{x,y}(\omega, \theta) \exp[i\omega(\tau_0 + n\Delta\tau)]|^2 \qquad (3.43)\\
&= |\tilde{E}_{x,y}(\omega, \theta)|^2 + |\tilde{E}^{\mathrm{LO}}_{x,y}(\omega, \theta)|^2 \\
&\quad + \tilde{E}^{*}_{x,y}(\omega, \theta)\tilde{E}^{\mathrm{LO}}_{x,y}(\omega, \theta) \exp[i\omega(\tau_0 + n\Delta\tau)] \\
&\quad + \tilde{E}_{x,y}(\omega, \theta)\tilde{E}^{\mathrm{LO}*}_{x,y}(\omega, \theta) \exp[-i\omega(\tau_0 + n\Delta\tau)]. \qquad (3.44)
\end{aligned}$$

Here, what one needs to extract is the fourth term in Eq. (3.44). In the 16 acquisitions, the LO delay is modulated from $\tau = \tau_0$ to $\tau = \tau_0 + 15\Delta\tau$ with the increment of $\Delta\tau$. Obtained raw spectra are shown in Fig. 3.4, where the peaks of the spectral fringes shifts by the evolution of τ. The observed intensity monitored at 540 nm plotted as a function of the data number is shown in Fig. 3.5 (a). Sine modulation originating to $\exp(i\omega(\tau_0 + n\Delta\tau))$ and $\exp(-i\omega(\tau_0 + n\Delta\tau))$ in Eq. (3.44) is observed which is observed as a peak around 0.3 in the reciprocal space (Fig. 3.5 (b)).

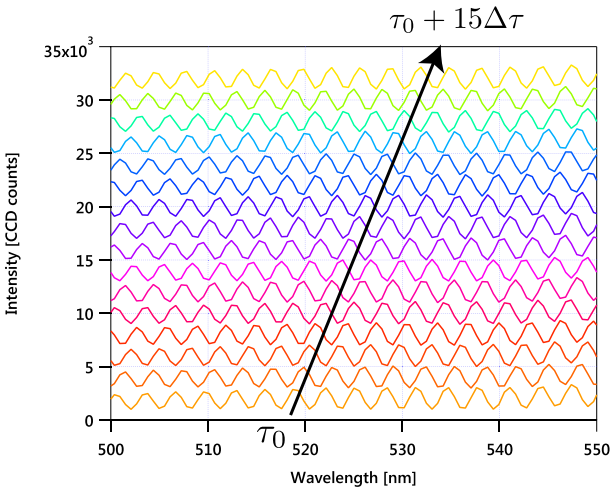

Figure 3.4: y component of the raw spectra obtained at $\theta = 0$. The LO delay is modulated from $\tau = \tau_0$ to $\tau = \tau_0 + \Delta\tau$.

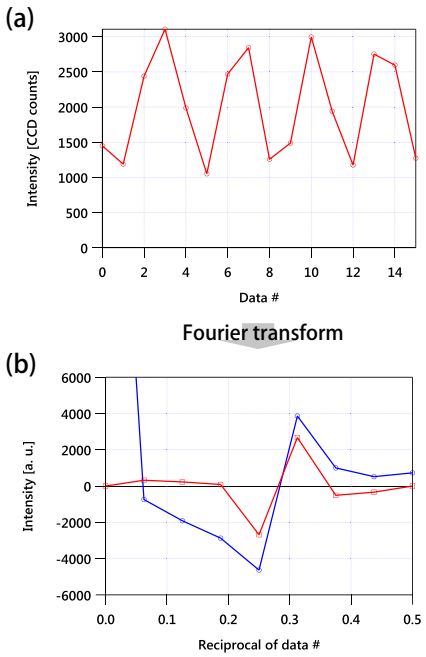

Figure 3.5: (a) Intensity change as a function of the data number. (b) Fourier transform of (a). The blue and red curves represent the real and imaginary parts, respectively.

By Fourier transforming $\tilde{I}_{x,y}(\omega, \theta, n)$ from n to m, one obtains

$$\begin{aligned}\hat{\tilde{I}}_{x,y}(\omega,\theta,m) &= \int dn \exp(-inm)\tilde{I}_{x,y}(\omega,\theta,n) \qquad (3.45)\\ &= \left(|\tilde{E}_{x,y}(\omega,\theta)|^2 + |\tilde{E}^{\mathrm{LO}}_{x,y}(\omega,\theta)|^2\right)\int dn \exp(-inm)\\ &\quad + \tilde{E}^{*}_{x,y}(\omega,\theta)\tilde{E}^{\mathrm{LO}}_{x,y}(\omega,\theta)\exp(i\omega\tau_0)\int dn \exp[-in(m-\omega\Delta\tau)]\\ &\quad + \tilde{E}_{x,y}(\omega,\theta)\tilde{E}^{\mathrm{LO}*}_{x,y}(\omega,\theta)\exp(-i\omega\tau_0)\int dn \exp[-in(m+\omega\Delta\tau)]. \qquad (3.46)\end{aligned}$$

Thus, in the $\hat{\tilde{I}}_{x,y}(\omega, \theta, m)$ spectra, as shown in Fig. 3.6, the homodyne and heterodyne terms are observed at $m = 0$ and $m = \pm\omega\Delta\tau$, respectively. Figure. 3.6 shows that the homodyne terms are observed only at $m = 0$. However, the heterodyne terms are distributed from $m = 1/16$ to $m = 8/16$ due to the spectral leakage in Fourier transformation [110], although it should be at $m = 4/16, 5/16$. The spectral leakage is not problematic in the current analysis because the component only at $m = 0$ is erased at this stage and the others remain. In m-space, the homodyne terms are erased by making $\hat{\tilde{I}}_{x,y}(\omega, \theta, 0) = 0$. Then, the spectra are inverse Fourier transformed from m to n-space to obtain

$$\begin{aligned}\tilde{I}'_{x,y}(\omega,\theta,n) &= \tilde{E}^{*}_{x,y}(\omega,\theta)\tilde{E}^{\mathrm{LO}}_{x,y}(\omega,\theta)\exp[i\omega(\tau_0+n\Delta\tau)]\\ &\quad + \tilde{E}_{x,y}(\omega,\theta)\tilde{E}^{\mathrm{LO}*}_{x,y}(\omega,\theta)\exp[-i\omega(\tau_0+n\Delta\tau)], \qquad (3.47)\end{aligned}$$

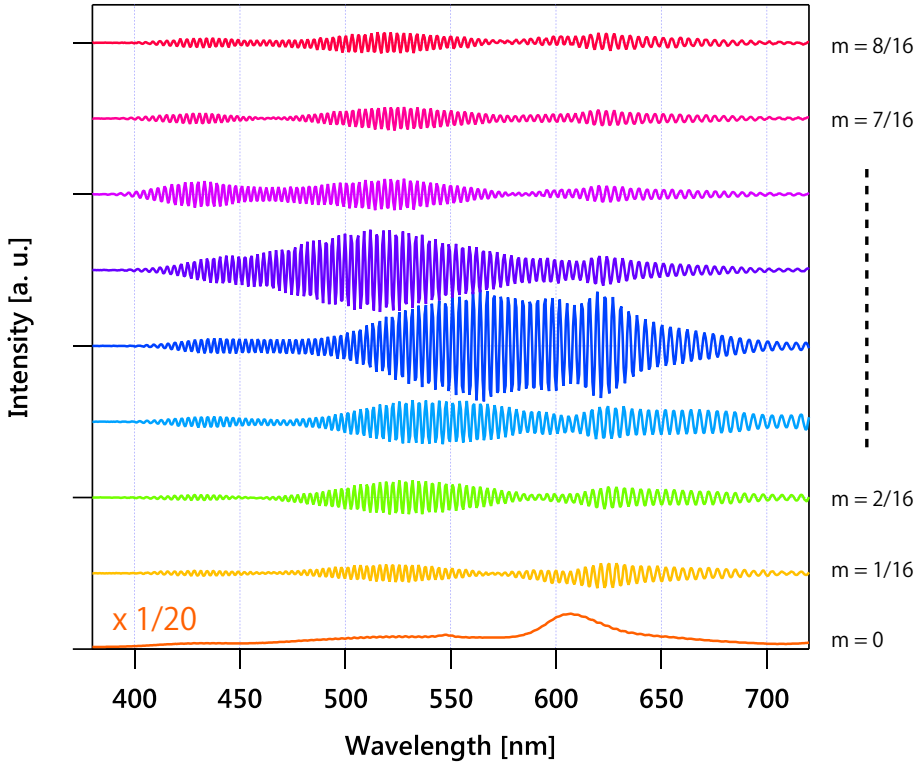

Figure 3.6: $\hat{\tilde{I}}_y(\omega, \theta, m)$ spectra obtained as Fourier transform of $\tilde{I}_y(\omega, \theta, n)$ from n to m.

whose spectrum at $n = 0$ is shown in the blue curve in Fig. 3.7 (a). By the comparison with the raw spectrum shown in the red curve in Fig. 3.7 (a), it is clearly seen that the homodyne contribution is canceled.

Next, $\tilde{I}'_{x,y}(\omega, \theta, n)$ is inverse Fourier transformed from ω-space to T-space to obtain the time-domain interferogram as follows:

$$I'_{x,y}(T, \theta, n) = \int d\omega \exp[-i\omega(T - \tau_0 - n\Delta\tau)]\tilde{E}^*_{x,y}(\omega, \theta)E^{\mathrm{LO}}_{x,y}(\omega, \theta) + \int d\omega \exp[-i\omega(T + \tau_0 + n\Delta\tau)]\tilde{E}_{x,y}(\omega, \theta)E^{\mathrm{LO}*}_{x,y}(\omega, \theta). \quad (3.48)$$

The experimentally obtained time-domain interferogran with $n = 0$ and $\theta = 0.0°$ is shown in Fig. 3.7(b). The first and second terms in Eq. (3.48) are observed at $T \simeq \pm 0.3$ ps and the residual homodyne terms are observed at $T = 0$. In order to extract the second heterodyne term, the filter function given by the blue curve in Fig. 3.7 (b) is multiplied by the time-domain interferogram. For comparison, the time-domain interferogram without the filtering in m-space is shown in Fig. 3.7 (c), where the homodyne and heterodyne terms are mixed to each other at around $T = 0.12$ ps. In this case, these are not separated simply by multiplying the filter function in the time domain. Reduction of the homodyne term by the filtering in m-space improves the separation of the heterodyne term from the homodyne term. This improvement is essential for sensitive measurement of weak chiroptical signals.

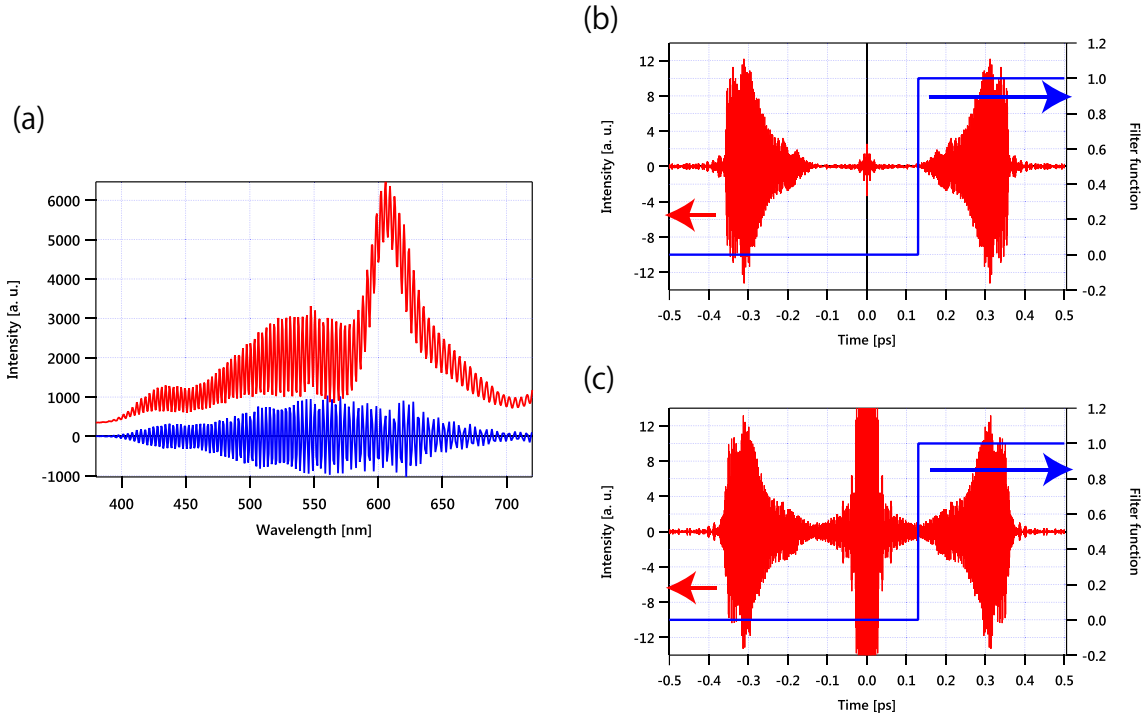

Figure 3.7: (a) Red curve: the raw spectrum obtained at $\theta = 0.0°$ and $\tau = \tau_0$, which corresponds to $\tilde{I}_y(\omega, 0.0°, 0)$. Blue curve: the spectrum after filtering in the m space, which corresponds to $\tilde{I}'_y(\omega, 0.0°, 0)$. (b) Red: Time-domain interferogram obtained at $\theta = 0.0°$ and $n = 0$, which corresponds to $\tilde{I}'_y(\omega, 0.0°, 0)$. Blue: Filter function employed to extract the heterodyne term at $T = \tau$. (c) Notation of each curve is the same as (b), but the time-domain interferogram was obtained without the filtering in the m space.

After the filtering in the time domain, the time-domain interfergram is Fourier transformed to obtain

$$F_{x,y}(\omega, \theta, n) = \tilde{E}^*_{x,y}(\omega, \theta)\tilde{E}^{\mathrm{LO}}_{x,y}(\omega, \theta)\exp[i\omega(\tau_0 + n\Delta\tau)]. \tag{3.49}$$

Through the use of Eqs. (3.36, 3.37, 3.49), $\alpha(\omega)$ spectra can be calculated.

3.3 Results and discussion

3.3.1 TRLD and TRLB measurements of DODCI

First, time-resolved $\alpha(\omega)$ spectra of DODCI after photoexcitation at 550 nm with non-parallel pump polarization ($\phi = 2.5°$) are observed. Because DODCI is achiral molecule, the real and imaginary parts of $\alpha(\omega)$ precisely correspond to the LD and LB spectra induced by the photoexcitation, respectively[2]. Figure 3.8 (a) shows LD spectra, which are observed as $\mathrm{Re}[\alpha]$, at selected delays. For comparison, the transient absorption (TA) spectra observed at the magic angle polarization are shown in Fig. 3.8 (b). The spectral shapes of these two resemble each other, but the temporal decay of the LD is faster than

[2]Actually, whether or not the sample is chiral, $\alpha(\omega)$ spectra are dominated by LD and LB when $\phi > 1°$.

that of the TA.

In general, the absorbance changes on the condition that the probe polarization is parallel and perpendicular to the pump polarization can be written by

$$A_{\parallel}(\lambda, t) = d \sum_i \sigma_i(\lambda) N_i(t) \frac{1 + 2r_i(t)}{3}, \tag{3.50}$$

$$A_{\perp}(\lambda, t) = d \sum_i \sigma_i(\lambda) N_i(t) \frac{1 - r_i(t)}{3}, \tag{3.51}$$

where i is the index of transitions, d is the thickness of the sample, $\sigma_i(\lambda)$ is the absorption cross section, and $N_i(t)$ is the number of molecules responsible for i-th transition at delay time t. In the above equations, $r_i(t)$ is the anisotropy defined by

$$r_i(\lambda, t) = \frac{1}{5}(3\cos^2\psi_i(t) - 1), \tag{3.52}$$

where $\psi_i(t)$ is the angle between the transition dipole moments of the probe and pump absorption. In the current measurement, what is measured as LD is

$$\begin{aligned} \mathrm{Re}[\alpha(\lambda, t)] &\simeq \frac{\tan\phi}{2}(A_{\parallel}(\lambda, t) - A_{\perp}(\lambda, t)) \\ &= \frac{d\tan\phi}{2} \sum_i \sigma_i(\lambda) N_i(t) r_i(t). \end{aligned} \tag{3.53}$$

In the usual TA measurement, the absorbance difference measured at the magic angle is written as

$$\begin{aligned} A_{\mathrm{MA}}(\lambda, t) &= \frac{1}{3}(A_{\parallel}(\lambda, t) + 2A_{\perp}(\lambda, t)) \\ &= d \sum_i \sigma_i(\lambda) N_i(t). \end{aligned} \tag{3.54}$$

As the anisotropy is determined by the angle of the transition dipole moment, its value is constant over a single transition. From Eqs. (3.53) and (3.54), the spectral profiles of LD and A_{MA} are the same if the anisotropy values are the same for all the measured transitions.

The sameness of the spectral profiles in the LD and TA indicates that all the considered transition dipole moments are parallel to each other. From its linearity of the structure of DODCI (Fig. 3.9), it is natural to assume that the transition dipole moments observed in the visible range are along its long axis.

The difference in decaying behavior between the LD and TA is attributable to $r(t)$. From the measurements of the LD and magic-angle TA, anisotropy value is calculated by taking the ratio of LD to TA. The decay profile of $r(t)$ is shown in Fig. 3.10. The temporal change of $r(t)$ is well reproduced by a single exponential function with the decay constant of 168 ± 3 ps, which is almost identical to the previously reported values [111, 112].

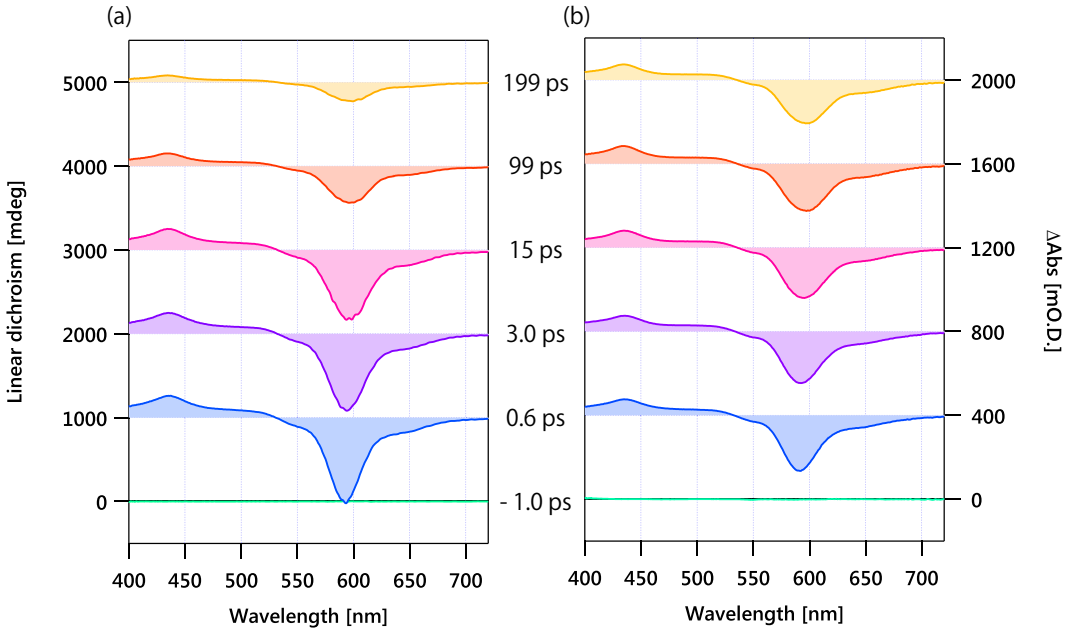

Figure 3.8: (a) Time-resolved LD and spectra of DODCI after photoexcitation at 550 nm with $\phi = 2.5°$. (b) Transient absorption spectra of DODCI measured at the magic angle polarization. The pump wavelength is the same as that of (a).

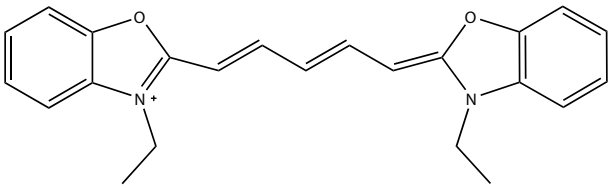

Figure 3.9: Molecular structure of DODCI

3.3.2 Kramers-Kronig relations between LD and LB

In the current measurements, LB spectra are also measured at the same time (Fig. 3.11). Linear birefringence is observed as the imaginary part of α and proportional to the difference between the refractive indices parallel and perpendicular to the pump polarization:

$$\begin{aligned} LB(\lambda, t) &= \mathrm{Im}[\alpha(\lambda, t)] \\ &= n_{\parallel}(\lambda, t) - n_{\perp}(\lambda, t) \\ &= \frac{d \tan \phi}{2} \sum_i \nu_i(\lambda) N_i(t) r_i(t), \end{aligned} \tag{3.55}$$

where $\nu_i(\lambda)$ represents wavelength dependence of refractive index of the i-th transition. As seen in the LD spectra, decay due to the relaxation of the anisotropy is also observed in the LB.

In the current setup, the LD and LB spectra are measured independently. However, these should

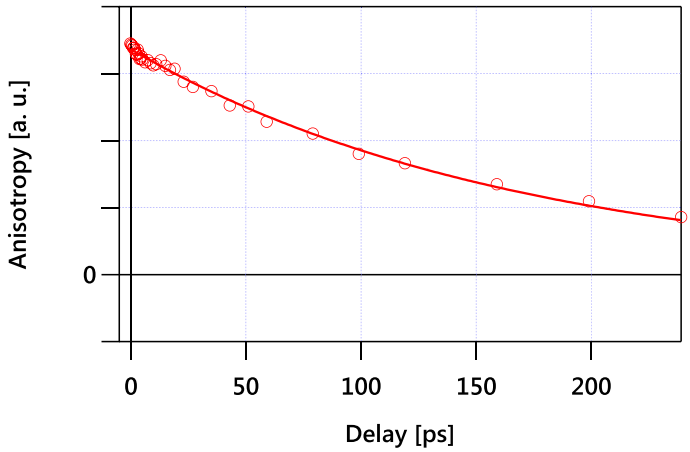

Figure 3.10: Temporal change of anisotropy $r(t)$ measured at 440 nm. The circles represent the observed data and the solid line represents the curve fitted by a single exponential function with the lifetime of 168 ± 3 ps.

be related to each other via the Kramers-Kronig (KK) relations as follows [113, 114]:

$$\mathrm{Re}[\alpha(\omega)] = \frac{2}{\pi}\mathcal{P}\int_0^\infty d\omega' \frac{\mathrm{Im}[\alpha(\omega')]\omega'}{\omega'^2 - \omega^2}, \tag{3.56}$$

$$\mathrm{Im}[\alpha(\omega)] = -\frac{2}{\pi}\mathcal{P}\int_0^\infty d\omega' \frac{\mathrm{Re}[\alpha(\omega')]\omega'}{\omega'^2 - \omega^2}, \tag{3.57}$$

where $\mathcal{P}$ denotes the Cauchy principle value. Hence, the satisfaction of the KK relations is a good criterion for the reliability of the measurements.

Below, LB spectrum is evaluated as the KK transform of the LD spectrum at 0.6 ps. It is hard to evaluate the integral in the above equations because they span from 0 to ∞ while the experimental data are obtained in the limited range. Instead, I evaluate the KK relations by decompose the observed LD spectrum into superposition of several Lorentzian functions as

$$\mathrm{Im}[\alpha(\omega)] = \sum_i \frac{A_i\Gamma_i}{(\omega - \omega_i)^2 + \Gamma_i^2}. \tag{3.58}$$

For the spectrum represented by Eq. (3.58), the KK transform can be analytically calculated as

$$\mathrm{Re}[\alpha(\omega)] = -\sum_i \frac{A_i(\omega - \omega_i)}{(\omega - \omega_i)^2 + \Gamma_i^2}. \tag{3.59}$$

To perform the KK transform, the LD spectrum at 0.6 ps was fitted by 5 Lorentzian functions as shown in Fig. 3.12 (a). Figure 3.12 (b) shows the LB spectra observed experimentally (red) and reproduced by the KK relations (blue). These two spectra are obviously consistent with each other. This is one strong evidence showing spectra obtained in the developed setup are reliable.

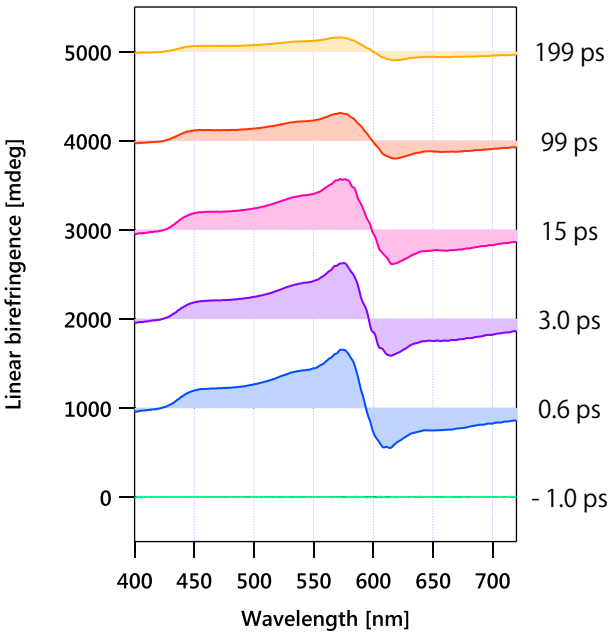

Figure 3.11: Temporal change of anisotropy $r(t)$ measured at 440 nm. The circles represent the observed data and the solid line represents the curve fitted by a single exponential function with the lifetime of 168 ± 3 ps.

3.3.3 TRCD and TRORD measurements of Ru(bpy)$_3^{2+}$

Steady-state CD and ORD spectra of Δ- and Λ-Ru(bpy)$_3^{2+}$ obtained with the setup developed in this study are shown in Fig. 3.13 (a) and (b), respectively. The spectra of the enantiomers form a mirror image and are consistent with the spectra measured with a commercial CD spectrometer. The imaginary and real parts of the obtained time-resolved $\alpha(\omega)$ spectra of Δ- and Λ-Ru(bpy)$_3^{2+}$ are shown in Fig. 3.13 (c) and (d), respectively. In these measurements, no chirp compensation was performed because the minimum time increment (4 ps) was longer than the cross-correlation between the pump and the probe pulse. The observed $\alpha(\omega)$ spectra at the longer delay are explained by the superposition of the bleach of the ground state CD and a broad CD peak ranging from 550 nm to over 730 nm, which is assignable to transient species. It should be noted that the spectra of the enantiomers at the longer delay time are in a mirror image even for weak (~ 0.4 mdeg) signal observed in the longer wavelength region. On the other hand, the obtained spectra are significantly distorted at the shorter delay time due to the photoinduced anisotropy.

3.3.4 SVD analysis

I performed SVD analysis on the obtained $\alpha(\omega)$ spectra of Λ-Ru(bpy)$_3^{2+}$ in order to separate spectral components with different time dependence. Here, a series of time-dependent $\alpha(\omega)$ spectra are denoted

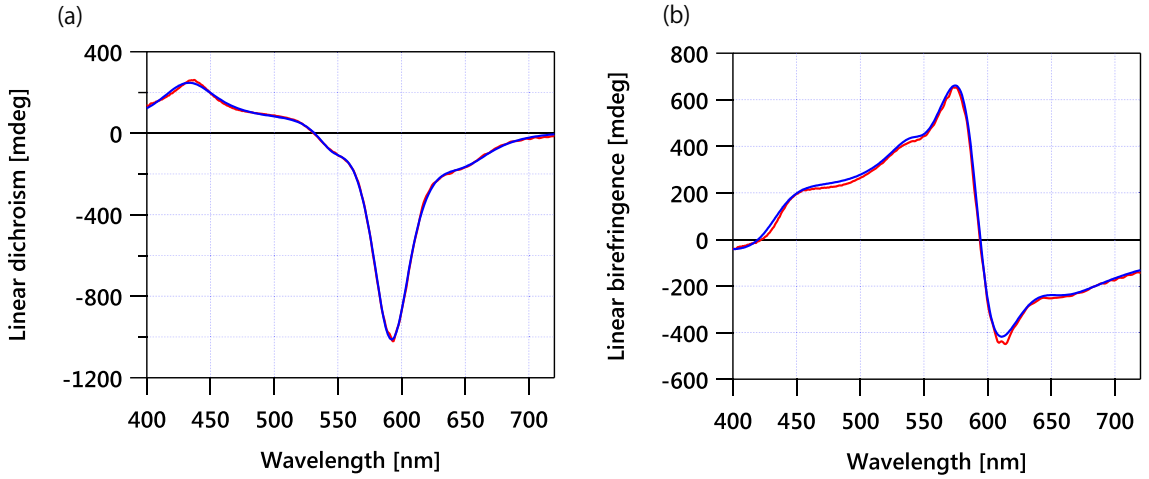

Figure 3.12: (a) Red: Observed LD spectrum of DODCI at $t = 0.6$ ps. Blue: Fitted curve by 5 Lorentzians. (b) Red: Observed LB spectrum of DODCI at $t = 0.6$ ps. Blue: LB spectrum reproduced by Kramers-Kronig transformation of the fitted LD spectrum (blue curve in (a)).

as

$$S = \begin{pmatrix} \boldsymbol{s_1} & \boldsymbol{s_2} & \cdots \end{pmatrix}, \tag{3.60}$$

where $\boldsymbol{s_i}$ corresponds to the spectrum obtained at the i-th delay. SVD decomposes S into the product of three matrices as

$$S = UWV^T, \tag{3.61}$$

where V^T is the transposed matrix of V. Here, the decomposition is done uniquely under the condition such that U and V are orthogonal and W is diagonal. Equation (3.61) is thus written in the vector form as

$$\begin{aligned} \begin{pmatrix} \boldsymbol{s_1} & \boldsymbol{s_2} & \cdots \end{pmatrix} &= \begin{pmatrix} \boldsymbol{u_1} & \boldsymbol{u_2} & \cdots \end{pmatrix} \begin{pmatrix} w_1 & 0 & \\ 0 & w_2 & \\ & & \ddots \end{pmatrix} \begin{pmatrix} \boldsymbol{v_1}^T \\ \boldsymbol{v_2}^T \\ \vdots \end{pmatrix} \\ &= \sum_i \boldsymbol{u_i} w_i \boldsymbol{v_i}^T. \end{aligned} \tag{3.62}$$

Results of the decomposition of $\mathrm{Im}[\alpha(\omega)]$ by SVD are shown in Fig. 3.14. From Fig. 3.14 (c), one can see that only the beginning two components have non-negligible contributions. In other words, the obtained $\mathrm{Im}[\alpha(\omega)]$ spectra are mostly reproduced by the superposition of $\boldsymbol{u_1}$ and $\boldsymbol{u_2}$, which temporally

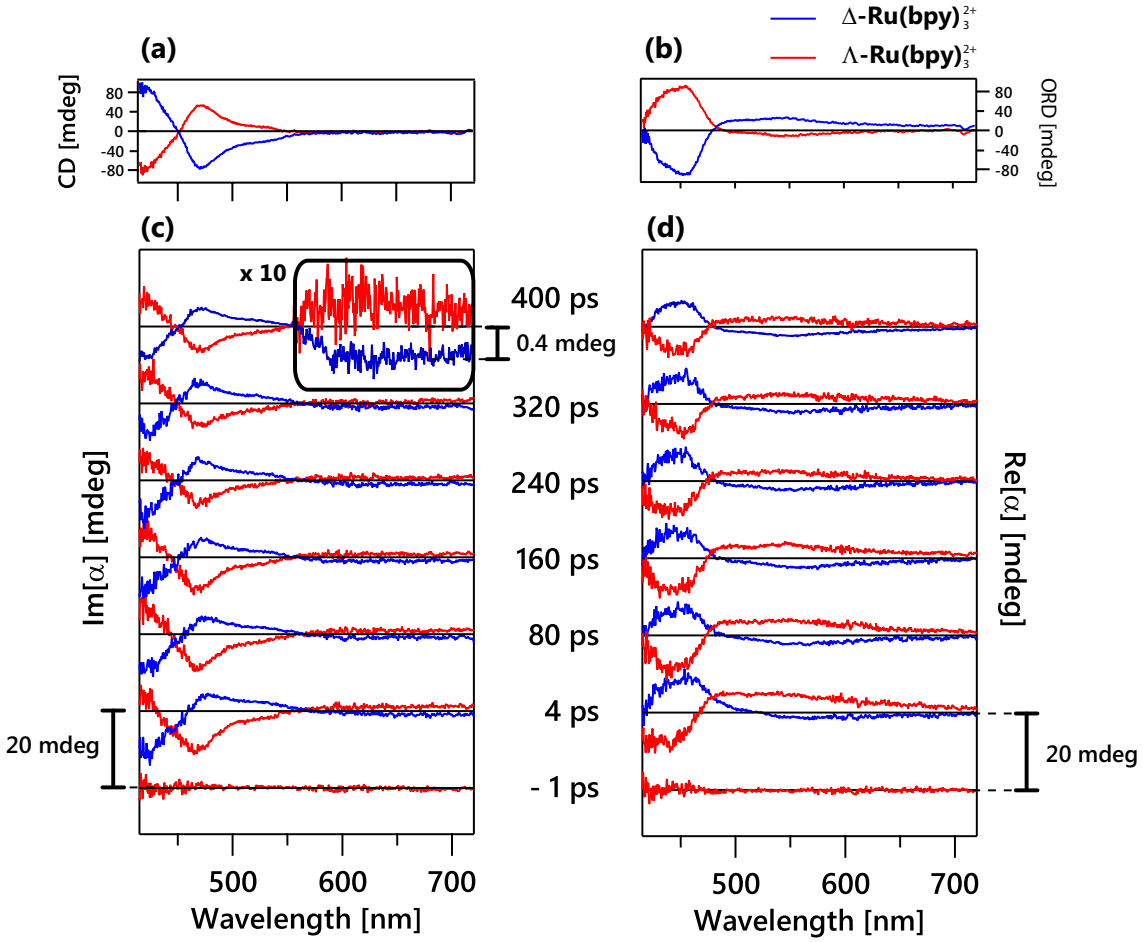

Figure 3.13: (a) CD and (b) ORD spctra of Δ- and Λ-Ru(bpy)$_3^{2+}$ in the ground state obtained with our setup. (c) Imaginary and (d) real part of obtained time-resolved $\alpha(\omega)$ spectra of Ru(bpy)$_3^{2+}$. The exposure time was 30 min for each spectrum except for that of the Δ-isomer at 400 ps delay time, which was obtained with 4 hours exposure time.

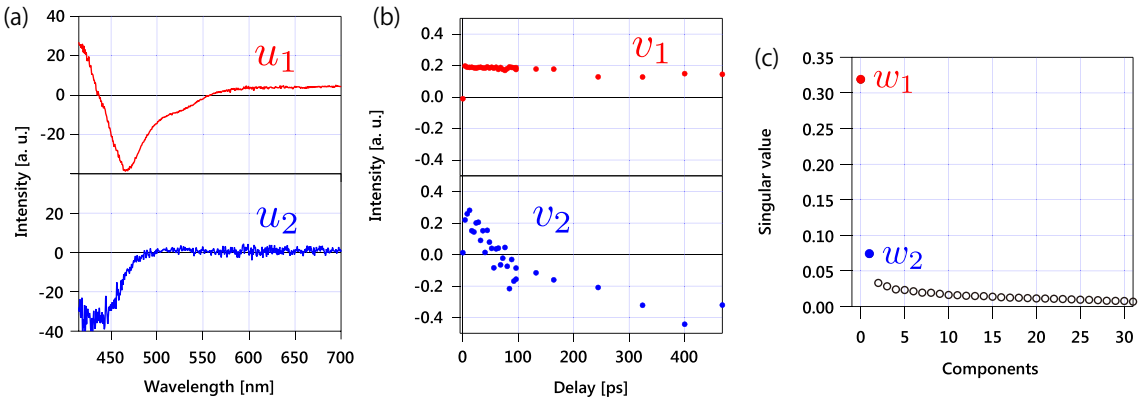

Figure 3.14: Singular value decomposition of time-dependent $\mathrm{Im}[\alpha(\omega)]$ spectra. (a) Spectral components (first and second columns of U matrix), (b) Temporal components (first and second rows of V matrix), (c) Singular values (diagonal values of W matrix)

evolve as $\boldsymbol{v_1}$ and $\boldsymbol{v_2}$, respectively, as follows:

$$\begin{pmatrix} \boldsymbol{s_1} & \boldsymbol{s_2} & \cdots \end{pmatrix} \simeq \begin{pmatrix} \boldsymbol{u_1} & \boldsymbol{u_2} \end{pmatrix} \begin{pmatrix} w_1 & 0 \\ 0 & w_2 \end{pmatrix} \begin{pmatrix} \boldsymbol{v_1}^T \\ \boldsymbol{v_2}^T \end{pmatrix}. \tag{3.63}$$

In SVD, as $\boldsymbol{u_i}$ and $\boldsymbol{v_i}$ are determined by the orthogonality condition, they are not physically meaningful in general.

At this stage, a model is needed for obtaining something physically meaningful. If the model spectral sets, $\boldsymbol{u_i'}$, or the model temporal changes, $\boldsymbol{v_i'}$, can be reproduced by the linear combination of $\boldsymbol{u_i}$ or $\boldsymbol{v_i}$, respectively, the model may explain the experimental data. The linear combination is taken with a transform matrix M as

$$\begin{aligned} S &= UWV^T \\ &= UWM^{-1}MV^T \\ &= U'V'^T \\ &= \sum_i \boldsymbol{u_i'}\boldsymbol{v_i'}^T, \end{aligned} \tag{3.64}$$

where

$$U' = UWM^{-1}, \tag{3.65}$$

$$V'^T = MV^T. \tag{3.66}$$

Usually one assumes the function form of either $\boldsymbol{u_i'}$ or $\boldsymbol{v_i'}$ by the model to calculate M. The other is then derived from the above equations.

In the current measurements, one can safely presume that there are two different components

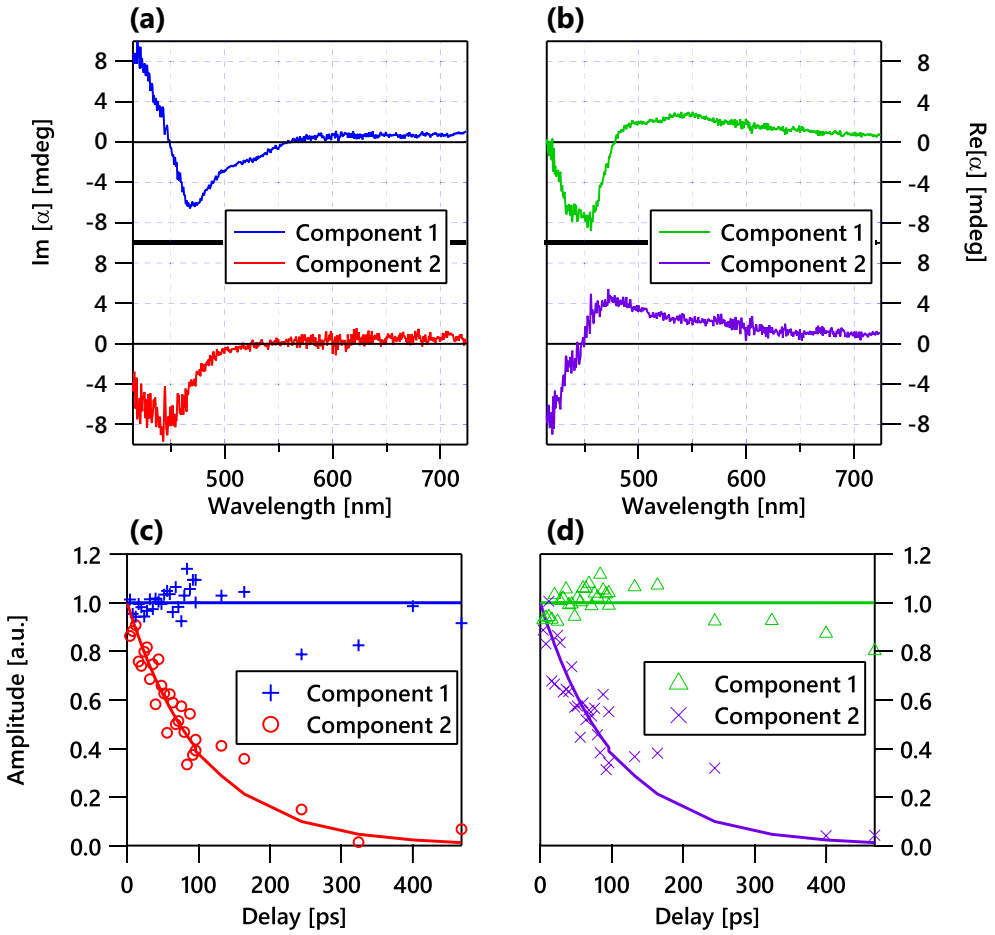

Figure 3.15: Results of SVD analysis on the time-resolved $\alpha(\omega)$ spectra of Λ-Ru(bpy)$_3^{2+}$. (a) Imaginary and (b) real parts of the spectra of the non-decaying and exponentially decaying components. (c,d) Time dependence of the imaginary and real parts of each component, respectively.

because w_i are almost zero at $i \geq 3$. I assume that one component does not change over time and the other exponentially decays;

$$v_1'(t) = v_{10}', \tag{3.67}$$

$$v_2'(t) = v_{20}' e^{-t/T}. \tag{3.68}$$

With V, from the SVD calculation, and V', from the model, M can be derived using Eq. (3.66). In the actual analysis, $v_1(t)$ and $v_2(t)$ are fitted by the superposition of $v_1'(t)$ and $v_2'(t)$, in which five parameters, each element of M and T, are determined. For $\mathrm{Im}[\alpha(\omega)]$, the model of the temporal changes, $v_1'(t), v_2'(t)$, are shown by the solid lines in Fig. 3.15 (c). The linear combination of $v_1(t)$ and $v_2(t)$, obtained from Eq. (3.66) with the M determined by the fitting procedure, are drawn by + and $\circ$ markers in Fig. 3.15 (c), which shows the current model well explains the obtained data. One can immediately calculate the corresponding spectra, $u_1'(\omega)$ and $u_2'(\omega)$, from Eq. (3.66), which are shown in Fig.3.15 (a). The same analysis is performed independently for the series of $\mathrm{Re}[\alpha(\omega)]$ spectra,

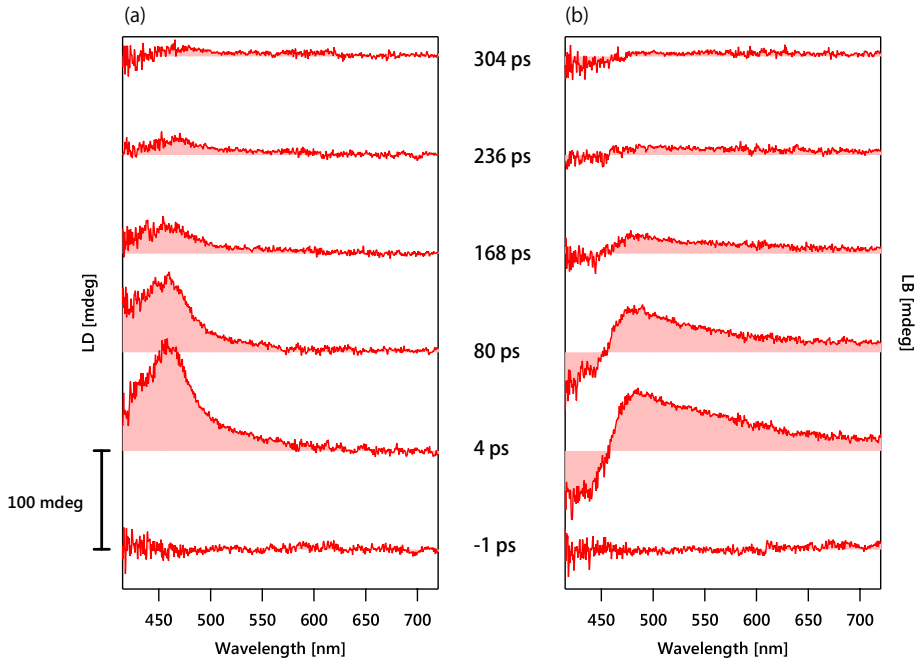

Figure 3.16: Time-resolved (a) LD and (b) LB spctra of Λ-Ru(bpy)$_3^{2+}$ after photoexcitation at 393 nm. Spectra are measured at $\phi = 5°$.

whose results are shown in Fig. 3.15 (b,d). As theoretically expected, both the real and imaginary parts of $\alpha(\omega)$ spectra are well reproduced by the same model.

Based on the fact that the spectrum of component 1 is reproduced by superposition of the reversed ground state spectrum and a broad positive peak above 550 nm, which is not observed in the ground state CD, I conclude that component 1 corresponds to the bleaching of the ground-state CD and the appearance of long-lived excited-state CD.

The decay time constant of component 2 is estimated to be 106 ± 13 ps, which is equal to that of the anisotropy (119 ± 10 ps) measured by LD. Thus, I conclude that component 2 arises from the photoinduced anisotropy. Although component 2 originates from the anisotropy, its spectral shape is different from that of LB (Fig. 3.16), which is superposed on $\alpha(\omega)$ spectra when the pump polarization is not parallel to the probe polarization. Therefore, it is impossible to remove this signal simply by rotating the polarizer for the pump radiation.

3.3.5 Assignments of the spectral components

There are several possible assignments for the broad CD peak observed in the wavelength range above 550 nm. Ru(bpy)$_3^{2+}$ is photoexcited to a singlet metal-to-ligand charge-transfer (MLCT) state, which undergoes ultrafast intersystem crossing to the long-lived triplet MLCT state. Besides the triplet MLCT state, Ru(bpy)$_3^{3+}$, Ru(bpy)$_3^{1+}$, and solvated electrons are reported as products of redox reactions of triplet MLCT state [115]. One can safely exclude the possibility of Ru(bpy)$_3^{1+}$ because it does not

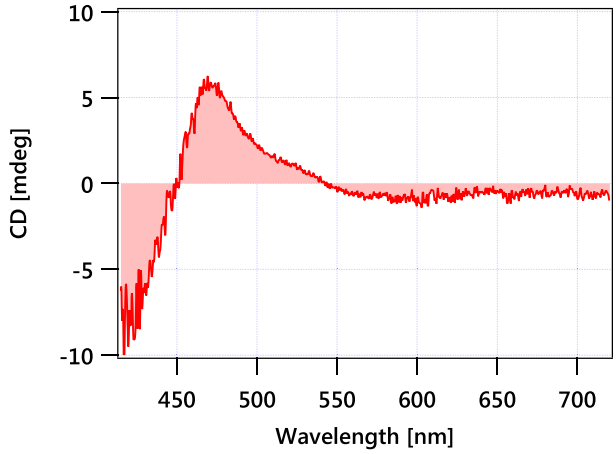

Figure 3.17: Time-resolved CD spectrum of Δ-Ru(bpy)$_3^{2+}$ with the electron scavenger (mixture of water and acetone with the ratio of 4:11). Spectrum was obtained at 468 ps after the photoexcitation.

possess absorption ranging from 570 to 730 nm [116]. Λ-Ru(bpy)$_3^{3+}$ has positive CD band from 400 to 500 nm [117], which is not discernible in the CD spectrum of component 1. Hence, the contribution of Λ-Ru(bpy)$_3^{3+}$ should be negligible. The solvated electron has a broad absorption above 500 nm and induced CD could be observed in this band if the electron is close to the chiral complex. In order to check this possibility, I measured the TRCD spectrum of the same sample with electron scavenger (mixture of water and acetone with the ratio of 4:11). It has been reported that the solvated electron scavenged within 1.2 ns in the presence of 1 $\%$ acetone [118, 119]. As seen in Fig. 3.17, with the addition of acetone, the spectral profile of the broad TRCD peak did not change from that with pure water. This allows us to discard the possibility of the solvated electron as the spectral carrier. Consequently, I concluded that the broad excited state CD comes from the triplet MLCT state.

There are two important advantages in our TRCD setup developed in this study over previous ones. The first one is better sensitivity. In the recently reported single wavelength TRCD measurements [74], the measurement error was about 0.3 mOD, which equals to 10 mdeg. Also in broadband TRCD spectroscopy, the sensitivity was estimated to be the order of 0.1 mOD [103]. The sensitivity obtained in this study ($<$ 0.4 mdeg or 0.013 mOD) is, at least, one order of magnitude better than in the previously reported TRCD measurements. The other advantage is that the genuine TRCD spectra are extracted from the raw spectra congested by the anisotropy induced signal. In the previous setups, it was assumed that the anisotropy induced signals were negligible by employing linear polarization parallel to the probe polarization [70, 100] or scrambled polarization [68, 99, 103] as pump pulses. However, spurious signals originating anisotropy have not been quantitatively estimated in these studies. In our setup, the anisotropy induced signals, which are induced even in the parallel polarization configuration, can be clearly differentiated from the true TRCD spectra using SVD analysis.

3.4 Conclusion

It is demonstrated that broadband and sensitive dichroism and birefringence spectroscopy with femtosecond time resolution are feasible by the polarization-resolved optical heterodyne detection. The developed setup was used both for time-resolved LD/LB and CD/ORD with using different pump polarization angle. In the TRCD spectroscopy using a linearly polarized pump light, it was impossible to remove completely the artificial signal coming from anisotropy. By combining broadband TRCD spectroscopy with SVD, I succeeded to extract the true TRCD spectra from the observed spectra. Using the setup, sensitivity of about 0.4 mdeg was achieved with 30 minutes exposure time. The developed broadband and sensitive TRCD spectrometer will open up possibilities of accessing ultrafast three-dimensional structural changes during photochemical reactions.

Chapter 4

Direct observation of photo-induced ultrafast chirality flip by TRCD spectroscopy

4.1 Introduction

In this Chapter, the actual application of the developed TRCD spectroscopy to biomolecular dynamics is demonstrated. As a target of biomolecular study with TRCD spectroscopy, I employ bilirubin (BR) molecule (Fig. 4.1 (a)) bound to human serum albumin (HSA). Bilirubin is one of the mammalian bile pigments. In the blood circulation, BR is transported by binding to serum albumins because BR is not water-soluble. Due to its biological importance and interest as a molecular scientific target, structure of the BR-HSA complex has been thoroughly investigated by X-ray crystallography [121], Resonance Raman spectroscopy [122], and CD spectroscopy [123–134]. Among them, CD spectroscopy is recognized as a particularly powerful tool for analyzing the structure of BR-serum albumin complexes because BR shows strong CD signal when it binds to serum albumins. CD spectra of BR-HSA complex show bisignate peaks in between 400 and 500 nm which correlate with the dihedral angle between the two dipyrrinone groups. One of the striking features of BR-HSA complex is its CD spectrum is flipped by changing the pH value of the solution [123, 125, 126], which is attributable to the sign inversion of the dihedral angle (Fig. 4.1 (b)). From the pH-dependent change of CD signal, this change of the structures is associated with the N-F transition of the protein [126].

Besides its steady-state structure, understanding the structural evolution of BR-HSA complex after photoexcitation is of importance in terms of application to phototherapy to lower BR concentration of patients with neonatal hyperbilirubinemia. Structural change in the excited-state BR-HSA complex has been investigated by fluorescence lifetime [135–137], transient absorption (TA) [136–138], and circularly polarized luminescence (CPL) [135, 139]. In the CPL study, Tran *et al.* [135, 139] reported

the sign of the CPL spectra are the same for pH=4.1 and 7.4 while CD spectra have opposite peaks at these pH values. They attributed this results to the chirality flip in the excited states, but its dynamical behavior has not been observed due to the lack of the ultrafast chiroptical techniques.

Herein, I report the direct observation of the ultrafast chirality flip of BR-HSA complex by the femtosecond TRCD spectroscopy. In this study, I have measured the TRCD and TA spectra of BR-HSA complex at pH=4.0 and 7.8 with the time resolution of $\sim$ 100 fs. Both the ground-state bleach (GSB) and excited-state absorption/CD (ESA/ESCD) are observed in the wavelength range between 400 and 500 nm. In order to interpret the observed ESA and ESCD spectra, I established a framework for calculating them based on the exciton coupling theory, which enables us to calculate the ESA and ESCD just from the information obtained in the ground state absorption and CD. The observed TRCD show that the BR-HSA complex undergoes the chirality flip with the time constant of 10 ps at pH= 4.0.

4.2 Theory

Here we consider TA and TRCD spectra of a dimer-like molecule consisting of two chromophores within the framework of the exciton coupling theory. In general, time-resolved spectra consist of GSB, ESA/ESCD, and stimulated emission (SE). The spectral shape of GSB can easily be determined because it is identical to the flipped steady-state absorption/CD. Computational estimation of the ESA/ESCD spectra is usually difficult because one needs to calculate the metastable states in the electronically excited states. Here I demonstrate a practical method for calculating ESA and ESCD by considering transitions only between the exciton states.

When a molecule consists of two interacting chromophores, i and j, one-exciton states $|\alpha\rangle$ and $|\beta\rangle$ are formed as the linear combination of the locally excited states (Fig. 4.1 (c)):

$$|\alpha\rangle = \frac{1}{\sqrt{2}}\Big(|ia\rangle|j0\rangle - |i0\rangle|ja\rangle\Big), \tag{4.1}$$

$$|\beta\rangle = \frac{1}{\sqrt{2}}\Big(|ia\rangle|j0\rangle + |i0\rangle|ja\rangle\Big), \tag{4.2}$$

where $|ia\rangle|j0\rangle, |i0\rangle|ja\rangle$ represent the states where chromophore i or j is locally excited. The ground-state absorption and CD are derived by calculating the transition electric dipole moment and the transition magnetic dipole moment. The transition dipole moment of the transitions $|0\rangle \rightarrow |\alpha\rangle$ and $|0\rangle \rightarrow |\beta\rangle$

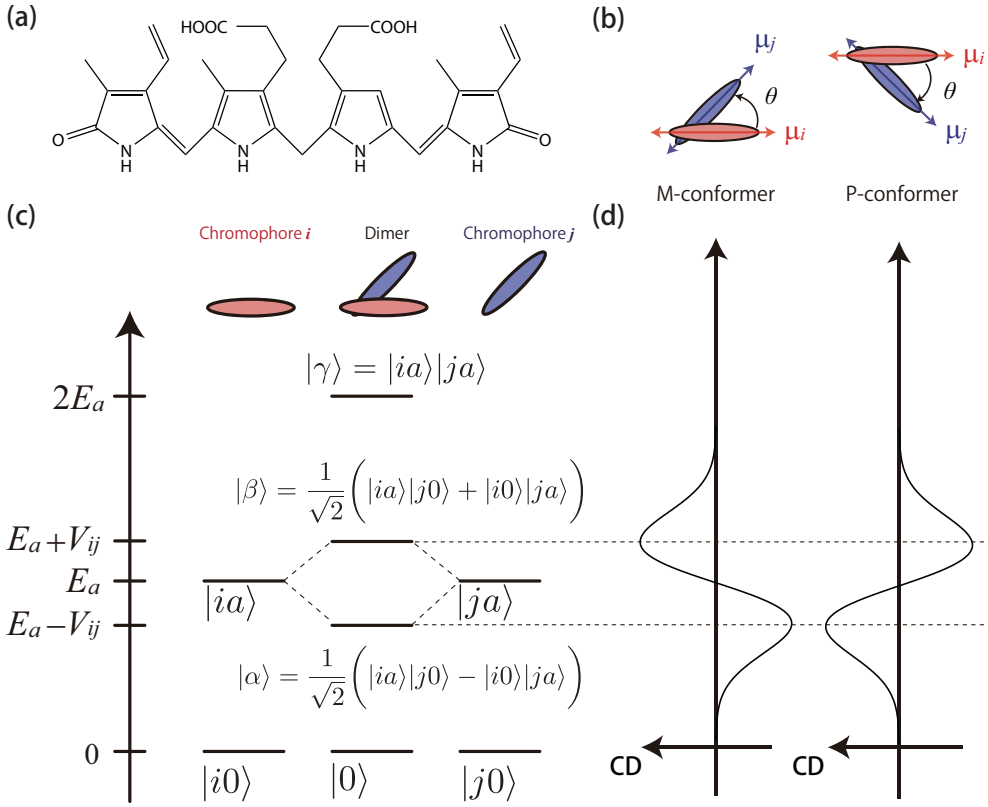

Figure 4.1: (a) Structure and (b) two enantiomeric conformers of BR. (c) Electronic energy states of BR given by the exciton coupling. (d) Schematic CD spectra of BR of P- and M-conformers

are calculated as

$$\begin{aligned}\langle 0|\boldsymbol{\mu}|\alpha\rangle &= \frac{1}{\sqrt{2}}\Big(\langle i0|\langle j0|(\boldsymbol{\mu}^i + \boldsymbol{\mu}^j)|ia\rangle|j0\rangle - \langle i0|\langle j0|(\boldsymbol{\mu}^i + \boldsymbol{\mu}^j)|i0\rangle|ja\rangle\Big) \\ &= \frac{1}{\sqrt{2}}(\boldsymbol{\mu}^i_{0a} - \boldsymbol{\mu}^j_{0a}), \qquad (4.3)\\ \langle 0|\boldsymbol{\mu}|\beta\rangle &= \frac{1}{\sqrt{2}}\Big(\langle i0|\langle j0|(\boldsymbol{\mu}^i + \boldsymbol{\mu}^j)|ia\rangle|j0\rangle + \langle i0|\langle j0|(\boldsymbol{\mu}^i + \boldsymbol{\mu}^j)|i0\rangle|ja\rangle\Big) \\ &= \frac{1}{\sqrt{2}}(\boldsymbol{\mu}^i_{0a} + \boldsymbol{\mu}^j_{0a}), \qquad (4.4)\end{aligned}$$

where $\boldsymbol{\mu}^i$ and $\boldsymbol{\mu}^j$ are the dipole moment operators of the isolated chromophores.

The total magnetic dipole moment $\boldsymbol{M}$ is defined as

$$\boldsymbol{M} = \frac{e}{2mc}(\boldsymbol{R}^i \times \boldsymbol{p}^i + \boldsymbol{R}^j \times \boldsymbol{p}^j) + \boldsymbol{m}^i + \boldsymbol{m}^j, \qquad (4.5)$$

where $\boldsymbol{R}^i, \boldsymbol{p}^i$ and $\boldsymbol{m}^i$ are the position, momentum, and the internal magnetic dipole moment of chromophore i. Thus, the transition magnetic dipole moment of the transitions $|0\rangle \to |\alpha\rangle$ and $|0\rangle \to |\beta\rangle$

are calculated as

$$\langle 0|\boldsymbol{M}|\alpha\rangle = \frac{1}{\sqrt{2}}\left[\frac{e}{2mc}\left(\boldsymbol{R}^i \times \boldsymbol{p}^i_{0a} - \boldsymbol{R}^j \times \boldsymbol{p}^j_{0a}\right) + \boldsymbol{m}^i_{0a} - \boldsymbol{m}^j_{0a}\right], \tag{4.6}$$

$$\langle 0|\boldsymbol{M}|\beta\rangle = \frac{1}{\sqrt{2}}\left[\frac{e}{2mc}\left(\boldsymbol{R}^i \times \boldsymbol{p}^i_{0a} + \boldsymbol{R}^j \times \boldsymbol{p}^j_{0a}\right) + \boldsymbol{m}^i_{0a} + \boldsymbol{m}^j_{0a}\right]. \tag{4.7}$$

For the linear momentum of the chromophore can be rewritten by using the dipole moment as

$$\boldsymbol{p}^i_{0a} = -\frac{2\pi i m c}{e}\sigma_0 \boldsymbol{\mu}^i_{0a}, \tag{4.8}$$

where σ_0 is the excitation energy [140].

Through the use of Eqs. (4.3, 4.4, 4.6, 4.7, 4.8), the dipole strength, D, and the rotational strength, R, of the transitions are given by

$$\begin{aligned} D(|0\rangle \to |\alpha\rangle) &= |\langle 0|\boldsymbol{\mu}|\alpha\rangle|^2 \\ &= \frac{1}{2}|\boldsymbol{\mu}^i_{0a} - \boldsymbol{\mu}^j_{0a}|^2, \end{aligned} \tag{4.9}$$

$$\begin{aligned} D(|0\rangle \to |\beta\rangle) &= |\langle 0|\boldsymbol{\mu}|\alpha\rangle|^2 \\ &= \frac{1}{2}|\boldsymbol{\mu}^i_{0a} + \boldsymbol{\mu}^j_{0a}|^2, \end{aligned} \tag{4.10}$$

$$\begin{aligned} R(|0\rangle \to |\alpha\rangle) &= \mathrm{Im}[\langle 0|\boldsymbol{\mu}|\alpha\rangle \cdot \langle \alpha|\boldsymbol{M}|0\rangle] \\ &= \frac{1}{2}\left[\mathrm{Im}\{(\boldsymbol{\mu}^i_{0a} - \boldsymbol{\mu}^j_{0a}) \cdot (\boldsymbol{m}^i_{a0} - \boldsymbol{m}^j_{a0})\} + \pi\sigma_0 \boldsymbol{R}^{ij} \cdot (\boldsymbol{\mu}^i_{0a} \times \boldsymbol{\mu}^j_{0a})\right], \end{aligned} \tag{4.11}$$

$$\begin{aligned} R(|0\rangle \to |\beta\rangle) &= \mathrm{Im}[\langle 0|\boldsymbol{\mu}|\alpha\rangle \cdot \langle \alpha|\boldsymbol{M}|0\rangle] \\ &= \frac{1}{2}\left[\mathrm{Im}\{(\boldsymbol{\mu}^i_{0a} + \boldsymbol{\mu}^j_{0a}) \cdot (\boldsymbol{m}^i_{a0} + \boldsymbol{m}^j_{a0})\} - \pi\sigma_0 \boldsymbol{R}^{ij} \cdot (\boldsymbol{\mu}^i_{0a} \times \boldsymbol{\mu}^j_{0a})\right]. \end{aligned} \tag{4.12}$$

For linear chromophores like dipyrrinone, the internal magnetic dipole moments $\boldsymbol{m}^{i,j}$ are negligible and the rotational strength is simplified to

$$R(|0\rangle \to |\alpha\rangle) = \frac{1}{2}\pi\sigma_0 \boldsymbol{R}^{ij} \cdot (\boldsymbol{\mu}^i_{0a} \times \boldsymbol{\mu}^j_{0a}), \tag{4.13}$$

$$R(|0\rangle \to |\beta\rangle) = -\frac{1}{2}\pi\sigma_0 \boldsymbol{R}^{ij} \cdot (\boldsymbol{\mu}^i_{0a} \times \boldsymbol{\mu}^j_{0a}). \tag{4.14}$$

So the sign of the two CD peaks of the dimer system are opposite to each other (Fig. 4.2 (b)) and its magnitude is determined by the angle between the transition dipole moments of chromophores i and j.

Suppose that the molecule is excited to $|\alpha\rangle$ to consider the excited-state CD and absorption. In this case, the transition $|\alpha\rangle \to |\gamma\rangle$ needs to be considered. Here, $|\gamma\rangle$ denotes the two-exciton state with

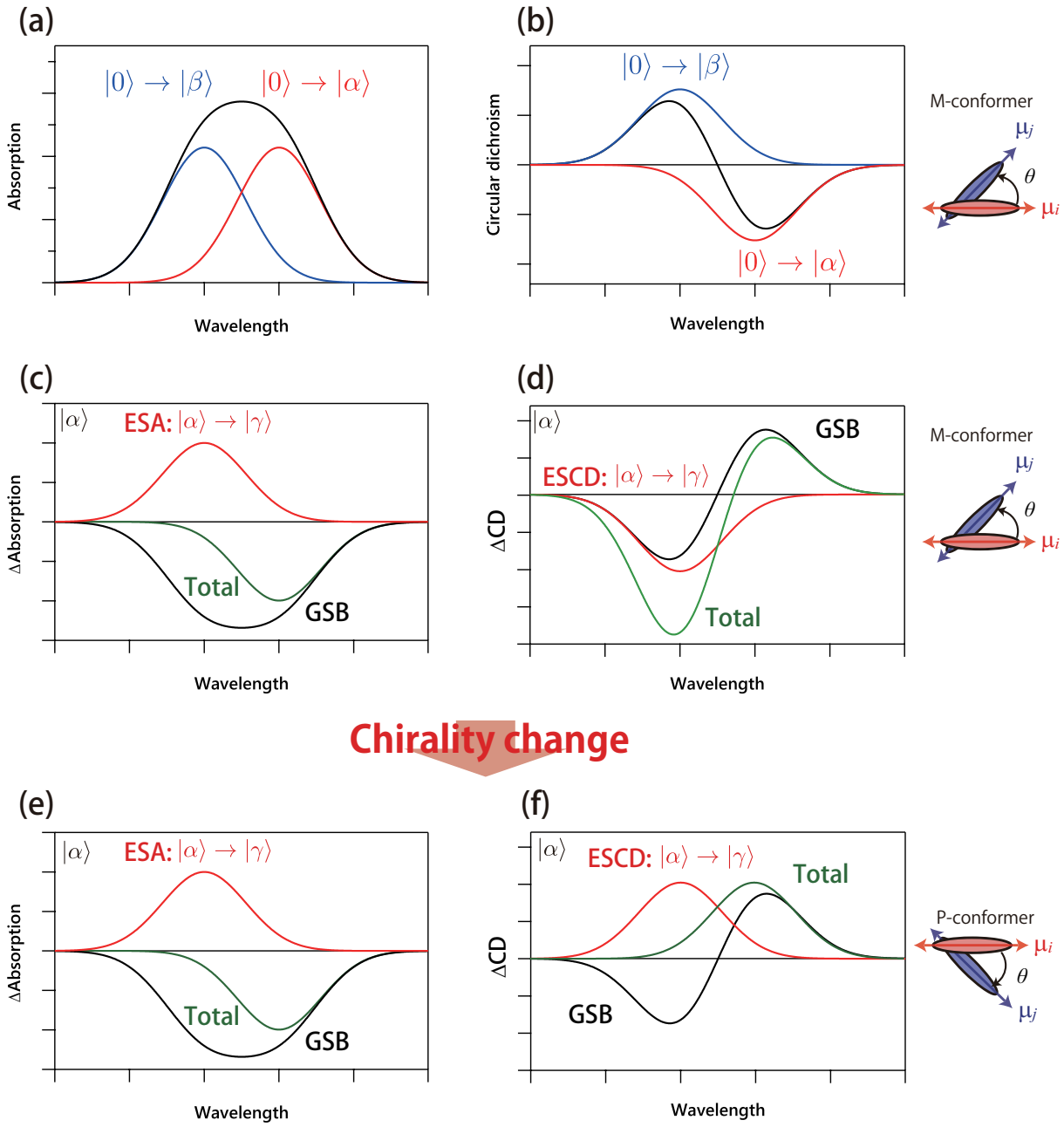

Figure 4.2: Schematic of the steady-state (a) absorption and (b) CD spectra of BR in the P-conformation. (c) TA and (d) TRCD spectra of BR in $|\alpha\rangle$ forming the P-conformer. (e) TA and (f) TRCD spectrum of BR in $|\alpha\rangle$ after the chirality flip to M-conformer.

both the chromophores excited:

$$|\gamma\rangle = |ia\rangle|ja\rangle. \tag{4.15}$$

If structural change in the excited states is negligible, the transition wavelength of $|\alpha\rangle \to |\gamma\rangle$ is identical to that of $|0\rangle \to |\beta\rangle$ (Fig. 4.1(c)). The dipole strength of this transition is given by

$$\begin{aligned} D(|\alpha\rangle \to |\gamma\rangle) &= \left|\langle\alpha|\boldsymbol{\mu}|\gamma\rangle\right|^2 \\ &= \frac{1}{2}\left|\langle ia|\langle j0|(\boldsymbol{\mu}^i + \boldsymbol{\mu}^j)|ia\rangle|ja\rangle - \langle i0|\langle ja|(\boldsymbol{\mu}^i + \boldsymbol{\mu}^j)|ia\rangle|ja\rangle\right|^2 \\ &= \frac{1}{2}\left|-\boldsymbol{\mu}^i_{0a} + \boldsymbol{\mu}^j_{0a}\right|^2 \\ &= D(|0\rangle \to |\alpha\rangle). \end{aligned} \tag{4.16}$$

Similarly, the rotational strength of $|\alpha\rangle \to |\gamma\rangle$ is calculated as

$$\begin{aligned} R(|\alpha\rangle \to |\gamma\rangle) &= \mathrm{Im}[\langle\alpha|\boldsymbol{\mu}|\gamma\rangle \cdot \langle\gamma|\boldsymbol{M}|\alpha\rangle] \\ &= \frac{1}{2}\left[\mathrm{Im}\{(-\boldsymbol{\mu}^i_{0a} + \boldsymbol{\mu}^j_{0a}) \cdot (-\boldsymbol{m}^i_{a0} + \boldsymbol{m}^j_{a0})\} + \pi\sigma_0 \boldsymbol{R}^{ij} \cdot (\boldsymbol{\mu}^i_{0a} \times \boldsymbol{\mu}^j_{0a})\right] \\ &= R(|0\rangle \to |\alpha\rangle). \end{aligned} \tag{4.17}$$

Thus, in this model, the magnitudes of ESA and ESCD associated with the transition $|\alpha\rangle \to |\gamma\rangle$ are the same as those with the transition $|0\rangle \to |\alpha\rangle$ as shown by the red spectra in Fig. 4.2 (c,d).

In the current discussion, it is assumed that SE is not observed in the wavelength range between 400 and 500 nm because large Stokes shift is observed in fluorescence on BR-HSA complex [141]. Thus, the total TA and TRCD at $|\alpha\rangle$ are given by the superposition of GSB and ESA/ESCD as shown in Fig. 4.2 (c,d). In the TA spectrum, GSB in the shorter wavelength range is canceled by the ESA. In the TRCD spectrum, on the other hand, those in the same wavelength range are constructively added. If the molecule is excited to $|\beta\rangle$ by pumping the absorption peak at the shorter wavelength, the ESA and ESCD are observed in the longer wavelength range, corresponding to $|\beta\rangle \to |\gamma\rangle$ transition. In this case, the ESA/ESCD peak in the longer wavelength is canceled by GSB in the TA spectrum and is constructively added with the GSB in the TRCD spectrum.

Structural change in the excited states can happen in actual cases. If the handedness of the molecule is reversed, the ESCD of $|\alpha\rangle \to |\gamma\rangle$ transition reverses while the ESA of the same transition remains the same as shown in Figs. 4.2 (e,f). Consequently, in this simple framework, the total TRCD peak at the shorter wavelength disappear by the chirality flip. In the actual experiments, the results are bit more complicated because also the de-excitation happens simultaneously and both $|\alpha\rangle$ and $|\beta\rangle$ are populated because two peaks are overlapped in the ground state absorption. Such complications will be taken into account as parameters in the fitting analysis as shown in Sec. 4.4.1.

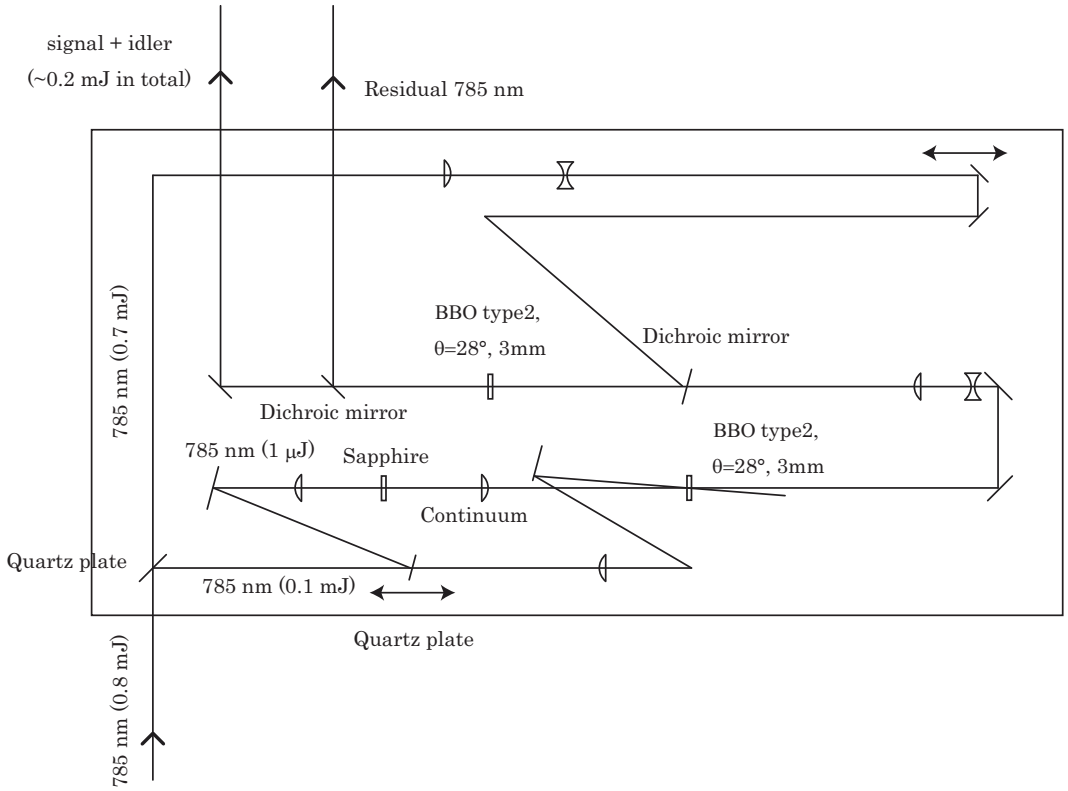

Figure 4.3: Schematic of the developed OPA system for generation of the wavelength-tunable pump radiation

4.3 Experimental

4.3.1 Optical setup

In this study, I have performed the TA and TRCD measurements of BR-HSA complex with excitation wavelength resonant with the exciton band. For the probe part of TRCD measurements, the setup and procedure presented in Chapter 3 is employed. For the generation of wavelength-tunable pump radiation, optical parametric amplifier (OPA) was newly developed.

The design of the developed two-stage OPA system is based on what is found in the literature [142]. About 0.8 mJ of the output of the regenerative amplifier was used for pumping the OPA system. An only small portion ($\sim$ 0.1 mJ) of the input beam is reflected by a quartz plate both for the generation of the seed pulse and for the pump pulse of the first-stage amplification. For the seed light, the beam reflected again by the quartz plate ($\sim 1\mu$J) is focused into a sapphire plate and white light continuum is generated. The generated continuum and the pump are spatially and temporally overlapped in a BBO crystal (type 2, $\theta = 28^\circ$, 3 mm). The temporal overlap is realized by finely tuning the position of the quartz plate until the sum-frequency generation between the pump pulse and the generated signal pulse is found. The amplified seed pulse is combined with the pump pulse for the second-stage amplification by a dichroic mirror. The seed pulse is further amplified by the intense pump radiation with $\sim$ 0.7 mJ

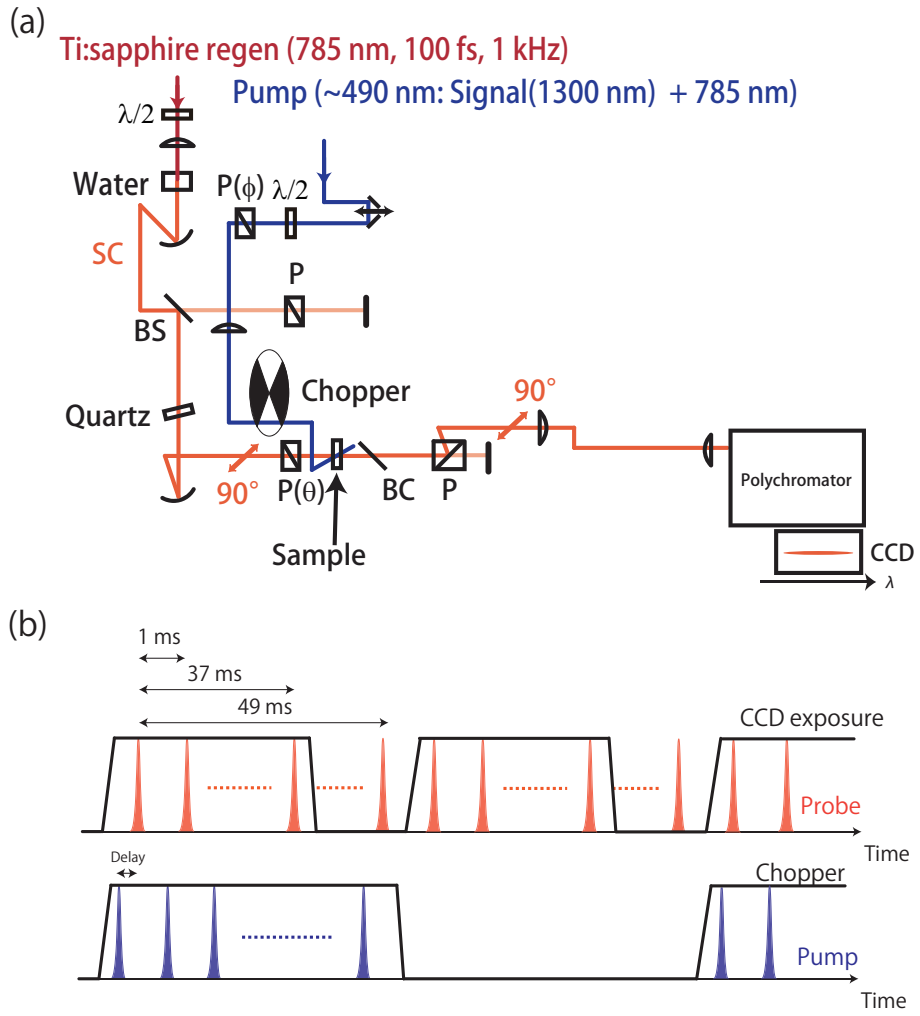

Figure 4.4: (a) Schematic of the setup used for TA measurements, (b) Timing sequence diagram of the pump and probe pulses with respect to the CCD exposure and the chopper.

and about 0.2 mJ of the output is obtained as a total power of the signal and the idler.

The pump radiation used in this study was at 490 nm, which was resonant with the lower exciton state of BR. In order to obtain such wavelengths, the sum frequency between the fundamental (785 nm) the signal ($\sim$ 1200 - 1570 nm) was generated.

For the TA measurements, the setup was slightly modified to what is shown in Fig. 4.4 (a). From the TRCD setup shown in Fig.3.2, the setup can easily be altered to this configuration just by blocking the local oscillator and the signal part after the polarizer. In TA measurements, the spectrum of the probe light whose polarization is parallel to the incident polarization is simply measured by the polychromator and CCD. In order to minimize the noise from the spectral fluctuation of the probe, the exposure time was set as short as possible in the current electronics. The sequence of the series of measurements are shown in Fig. 4.4 (b). The chopper, synchronized with the laser output TTL divided by 100 (10 Hz), is used for modulating the pump pulses. The CCD exposure, on the other hand, is synchronized with the laser output TTL divided by 50 (20 Hz) to alternately obtain the spectra with

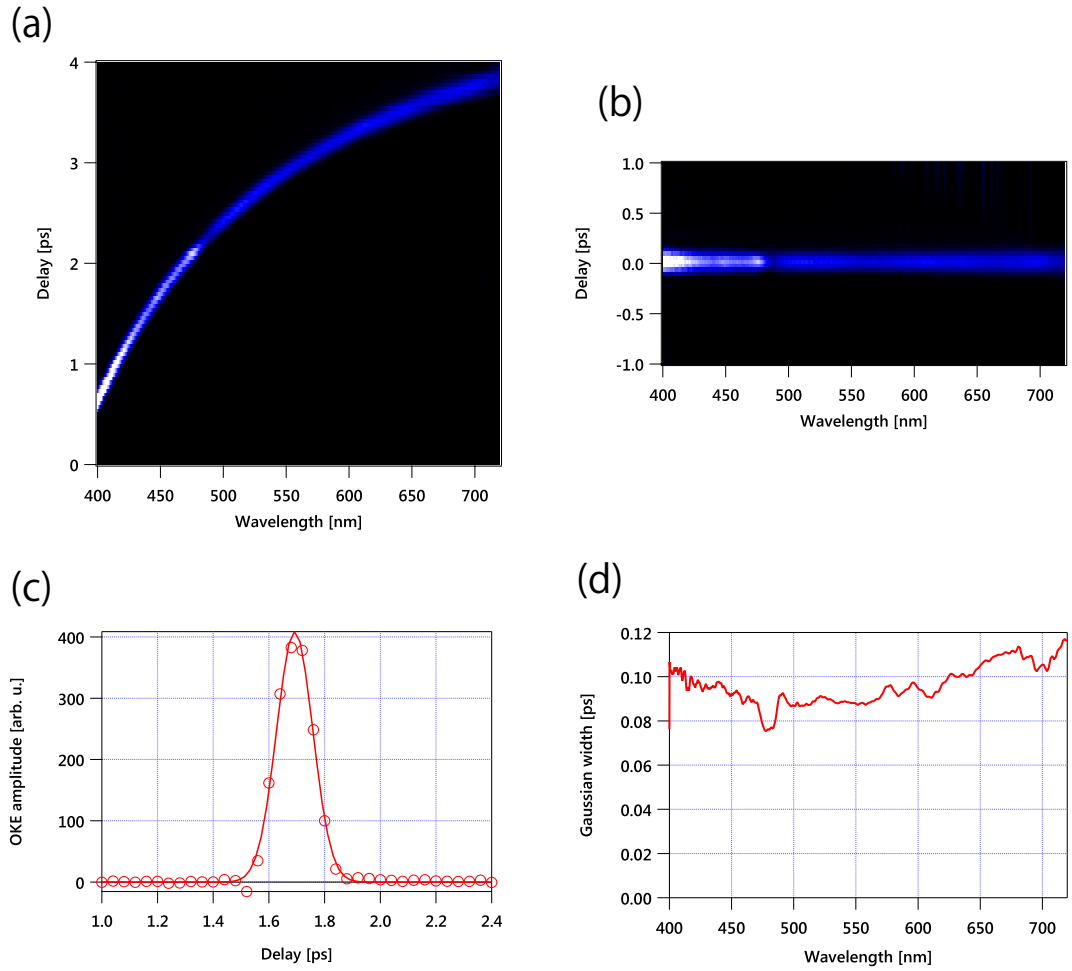

Figure 4.5: (a) 2D-plot of the cross correlation between the pump and probe measured as the OKE of water, (b) 2D-plot of the cross correlation between the pump and probe after the chirp compensation, (c) Typical delay-dependent OKE signal measured at 450 nm, (d) Wavelength dependence of the temporal width of the OKE signal obtained by Gaussian fitting

and without the pump light. Each measurement with and without the pump light is repeated for 20 times for a single delay and the delay stage is moved to the next position.

Prior to the TA and TRCD measurements, I have performed the optical Kerr effect (OKE) measurements of water. Two-dimensional plot of OKE signal is shown in Fig. 4.5 (a). It is seen that the probe light is strongly chirped due to the dispersion of optical components such as polarizers. To compensate the chirp structure of the probe light, the OKE signal is fitted by a Gaussian function (Fig. 4.5 (c)). After the measurements of TA and TRCD, the time origin of them at each wavelength is shifted by the central position of the fitted Gaussian functions. From the 2D plot of the OKE signal after the chirp compensation by the OKE signal itself, which is shown in Fig. 4.5 (b), we see the procedure for the chirp compensation works well. The wavelength-dependent plot of the width of the fitted Gaussians is given in Fig. 4.5 (d). Temporal resolution is about 100 fs in the current setup over the whole spectral range.

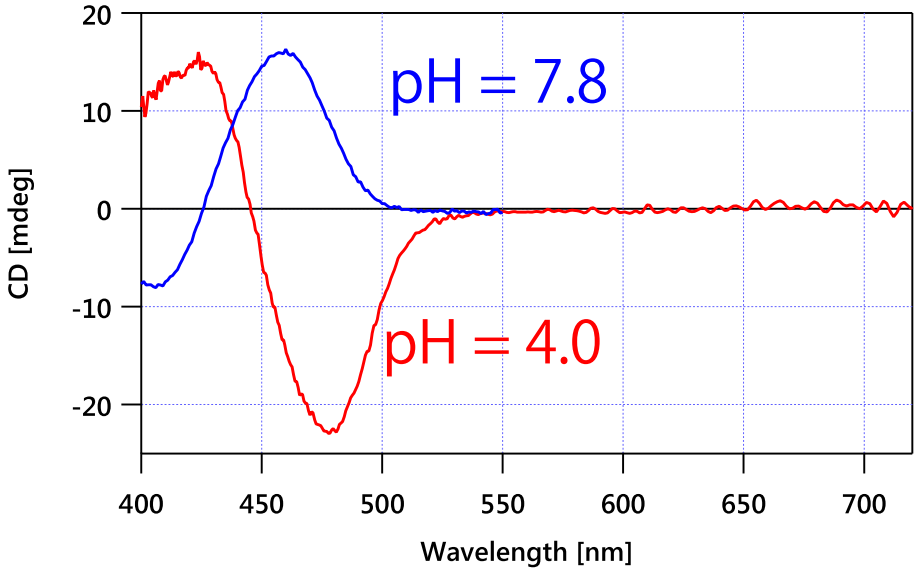

Figure 4.6: Steady-state CD spectra of BR-HSA complex (100 μM) at pH=4.0 and 7.8.

4.3.2 Sample preparation

Complexation of BR to HSA was performed by following the reported procedure [134]. Bilirubin was purchased from Wako and used as received. Human serum albumin was purchased from Wako and defatted by the charcoal treatment [143] prior to use. Albumin (5 g) was dissolved in 50 mL of water and pH of the solution was adjusted to 3.0 by the addition of hydrochloric acid. Charcoal (0.5 g) was added, and the solution was stirred for 1 hour in an ice bath. Charcoal was then removed by centrifuge and filtration (Whatman, GX/X, PVDF, 0.2 μm). The pH of the solution was adjusted to 7.0, and the solution was stored in a refrigerator.

Before BR is mixed with the defatted HSA solution, solid BR is pre-dissolved in NaOH solution ($\sim$ 100 mM). A stock solution of BR and HSA are mixed with the molar ratio of 1:1 and the final concentration was adjusted to 100 μM by adding the buffer solution (acetate buffer for pH=4.0 and Tris-HCl for pH=7.8). Complexation was confirmed by measuring the steady-state CD spectra of BR-HSA complexes at pH=4.0 and 7.8. As reported in the literatures [123–125], CD spectrum is reversed at these two pH values as shown in Fig. 4.6.

4.4 Results and discussion

4.4.1 TA and TRCD spectra of BR-HSA complex at pH=4.0

Figure 4.7 (c) shows the TA spectra of BR-HSA complex at pH=4.0 after the photoexcitation at 490 nm. Pump polarization was set to the magic angle (54.7°). In the wavelength range longer than 500 nm, TA spectra are dominated by the ESA, which is consistent with the previously reported TA data

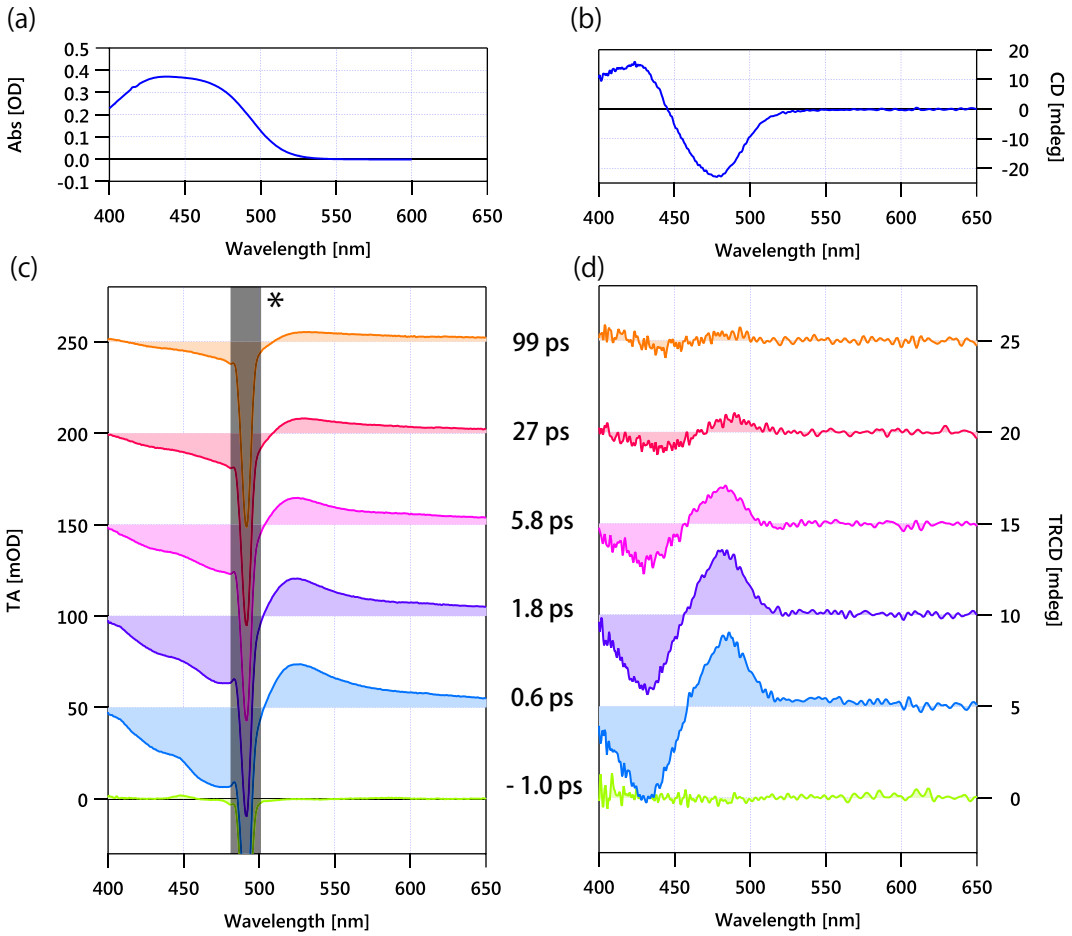

Figure 4.7: Steady-state (a) absorption and (b) CD spectra of the BR-HSA complex (100 μM) at pH=4.0. (c) TA and (d) time-resolved CD spectra of the BR-HSA complex (100 μM) at pH=4.0 after photoexcitation at 490 nm. * Negative peak due to strong scattering from the pump radiation is observed in the hatched region.

of BR in bulk solution and bound to HSA [136–138]. In the wavelength between 400 and 500 nm, the TA spectra look dominated by the GSB but its spectral shape is significantly different from that in the ground-state absorption (Fig. 4.7 (a)). Namely, the absolute magnitude of the TA is stronger at around 470 nm. As we can assume that the molecule is excited mainly to $|\alpha\rangle$ by the 490-nm excitation, the positive ESA at around 430 nm should be observed as with the schematic TA spectrum in Fig.4.2 (c). This ESA partially cancels the negative GSB and the absolute magnitude of the TA signal at 430 nm results in smaller than that at 470 nm.

Figure 4.7 (d) shows TRCD spectra of BR-HSA complex at pH=4.0 after the photoexcitation at 490 nm at selected delays. The spectra in the wavelength range between 400 and 500 nm are reproduced by the superposition of the GSB and ESCD as is the case in the TA. In the TRCD spectra, as opposed to the situation in the TA, the absolute magnitude of the band at the shorter wavelength is stronger than that in the ground-state CD. This is also consistent with the discussion in Section 4.2, in which the ESCD and GSB at 430 nm are constructively added to each other (Fig.4.2 (d)).

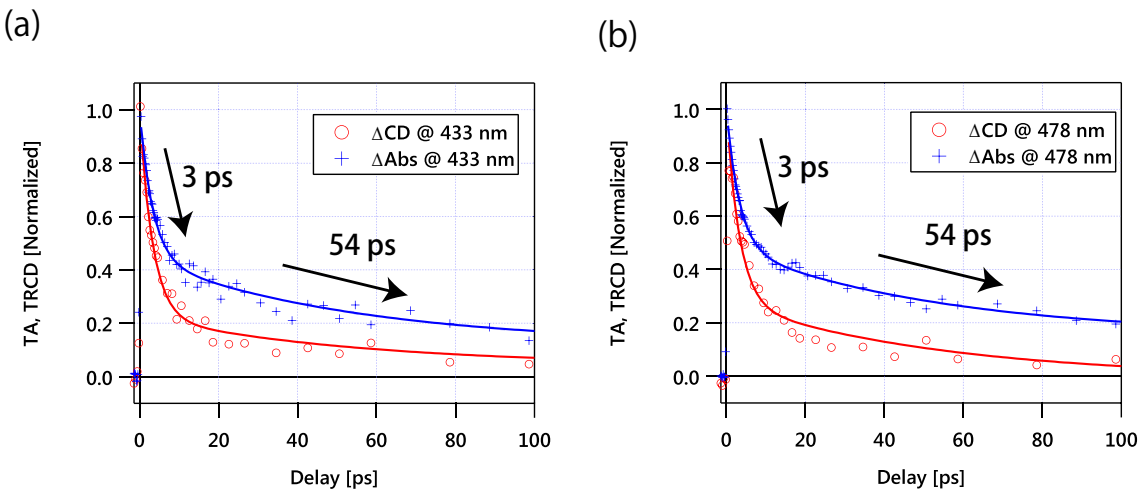

Figure 4.8: Time dependent change of the normalized TA and TRCD at (a) 433 nm and (b) 478 nm.

The temporal change of the TA and TRCD at 433 nm and 478 nm are plotted in Figs. 4.8 (a) and (b), respectively. In these curves, the intensity is normalized by the value at the time origin. The decay at each wavelength is reproduced by bi-exponential function with the time constant of 3 and 54 ps. However, the magnitude of the faster component is significantly larger in the TRCD than in the TA. This indicates that the decay of TRCD does not simply come from the de-excitation to the ground state, where the normalized decay curves of the TRCD and the TA should be the same. These data also cannot be explained by assuming that the BR is racemized by photoexcitation and kept racemized even after the de-excitation. In this case, the TA should decay faster than the TRCD, which is opposite to the data obtained here. We show below that the results obtained here are attributed to the chirality change in the excited state.

To explain both the bi-exponential decay and the difference in the amplitude between the TRCD and TA, the model shown in Fig. 4.9 is developed. BR-HSA complex forms P-conformer in the ground state at pH=4.0 [125]. After the photoexcitation, two possible channels are considered. One is to relax directly to the ground state by the rate constant of k_1 without a significant structural change in the excited state. The other is to undergo the chirality flip to M-conformer by the rate constant of k_2 and then relax to the ground state by k_3. It is assumed that the rate of the chirality change back to the P-conformer in the ground state is much larger than k_3. In this model, temporal change of the population of each state is governed by the following differential equations:

$$\frac{d[\mathrm{M}]}{dt} = k_1[\mathrm{M}^*] + k_3[\mathrm{P}^*], \tag{4.18}$$

$$\frac{d[\mathrm{M}^*]}{dt} = -k_1[\mathrm{M}^*] - k_2[\mathrm{M}^*], \tag{4.19}$$

$$\frac{d[\mathrm{P}^*]}{dt} = k_2[\mathrm{M}^*] - k_3[\mathrm{P}^*]. \tag{4.20}$$

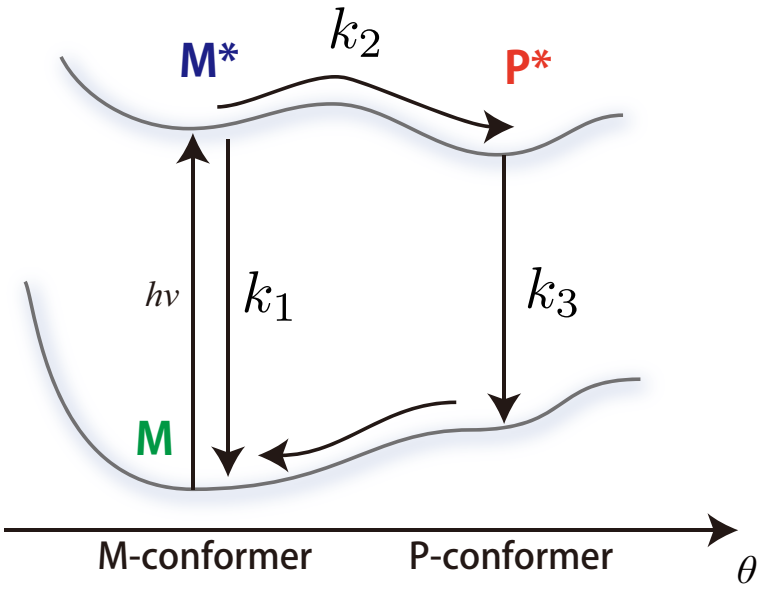

Figure 4.9: A model developed for explaining the observed TA and TRCD.

To actually perform the fitting analysis, the spectral shape of each state needs to be assumed. Obviously, the CD and absorption spectra of M should be the same as those observed in the steady-state (Figs. 4.10 (a,d)). As for M*, both the lower and higher exciton states, $|\alpha\rangle$ and $|\beta\rangle$, are taken into consideration to reproduce the experimental data. First, the complex at $|\alpha\rangle$, which is referred to as M*($|\alpha\rangle$), is considered. In this case, the absorption and CD of M*($|\alpha\rangle$) should be observed at around 430 nm as discussed above. As shown in Eq. (4.16), the dipole strength of the ESA at M*($|\alpha\rangle$) is the same as that of the 470-nm band of the ground-state absorption, which is positive. As shown in Eq. (4.17), the rotational strength of the ESCD at M*($|\alpha\rangle$) is also the same as that of the 470-nm band of the ground-state CD, which is negative. The dipole strength and the rotational strength of the ground-state exciton band were estimated by fitting the ground-state absorption and CD by two Gaussian functions as shown in Figs. 4.10 (a) and (d). The common width and central wavelength of the two gaussian functions were used in the fitting procedure. Then, the absorption and CD spectra of M*($|\alpha\rangle$) become those shown in Figs. 4.10 (b) and (e), respectively. Next, the higher exciton state, M*($|\beta\rangle$) is considered. In this case, the absorption and CD should be observed at around 470 nm. The sign of the CD spectrum of M*($|\beta\rangle$) becomes positive because its rotational strength is the same as that of the 430-nm band in the ground-state CD. Consequently, the absorption and CD spectra of M*($|\beta\rangle$) are assumed to be those shown in Figs. 4.10 (c) and (f), respectively. In the following analysis, the spectral shape of P*($|\alpha\rangle$) and P*($|\beta\rangle$) is assumed to be arbitrary because we do not have enough structural information for predicting it at this stage.

With the absorbance and CD values of state X at wavelength λ, $A_{\mathrm{X},\lambda}$ and $CD_{\mathrm{X},\lambda}$, the time depen-

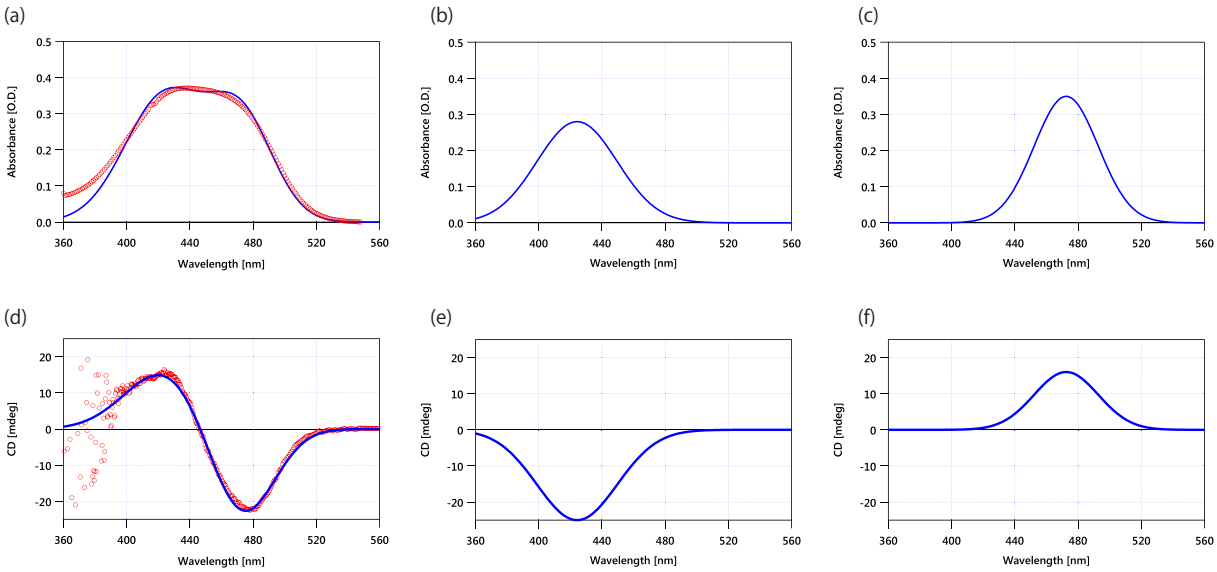

Figure 4.10: (a) Circles: Ground state absorption spectrum of BR-HSA complex at pH=4.0. Line: Fitting result by two gaussian functions. (b, c) Absorption spectra of b: $\mathrm{M}^*(|\alpha\rangle)$ and c: $\mathrm{M}^*(|\beta\rangle)$ estimated by using the exciton coupling theory. (d) Circles: Ground state CD spectrum of BR-HSA complex at pH=4.0. Line: Fitting result by two gaussian functions. (e, f) CD spectra of e: $\mathrm{M}^*(|\alpha\rangle)$ and f: $\mathrm{M}^*(|\beta\rangle)$ estimated by using the exciton coupling theory.

dent change of TA and TRCD at 433 nm and 478 nm are given by the following equations:

$$\begin{aligned}\mathrm{TA}_\lambda(t) = &-(1-[\mathrm{M}](t))A_{\mathrm{M},\lambda} + [\mathrm{M}^*](t)[RA_{\mathrm{M}^*(|\alpha\rangle),\lambda} + (1-R)A_{\mathrm{M}^*(|\beta\rangle),\lambda}] \\ &+ [\mathrm{P}^*](t)[RA_{\mathrm{P}^*(|\alpha\rangle),\lambda} + (1-R)A_{\mathrm{P}^*(|\beta\rangle),\lambda}], \qquad (4.21)\\ \mathrm{TRCD}_\lambda(t) = &-(1-[\mathrm{M}](t))CD_{\mathrm{M},\lambda} + [\mathrm{M}^*](t)[RCD_{\mathrm{M}^*(|\alpha\rangle),\lambda} + (1-R)CD_{\mathrm{M}^*(|\beta\rangle),\lambda}] \\ &+ [\mathrm{P}^*](t)CD_{\mathrm{P}^*,\lambda}, \qquad (4.22)\end{aligned}$$

where λ is the wavelength, which can be 433 nm or 478 nm, and R is the population ratio of $|\alpha\rangle$ to total population of $|\alpha\rangle$ and $|\beta\rangle$. In the above equations, the concentration was normalized by 1, namely $[\mathrm{M}] + [\mathrm{M}^*] + [\mathrm{P}^*] = 1$, and it was assumed that the absorption spectrum of M^* was identical to that of P^*, namely $A_{\mathrm{M}^*(|\alpha,\beta\rangle),\lambda} = A_{\mathrm{P}^*(|\alpha,\beta\rangle),\lambda}$. Therefore, seven parameters, $k_1, k_2, k_3, R, CD_{\mathrm{P}^*,433\mathrm{nm}}$, $CD_{\mathrm{P}^*,478\mathrm{nm}}$ and the initial concentration of $[\mathrm{M}^*]$, determines the temporal change of TA and TRCD in the current model. The experimental data shown in Fig. 4.8 were then fitted by Eqs. (4.21, 4.22) with the solution of Eqs. (4.18, 4.19, 4.20).

The fitting results are shown in Fig. 4.11 (a) and the obtained parameters are shown in Table. 4.1. As seen in Fig. 4.11 (a), the temporal evolution of the TA and TRCD are well reproduced by the current model. After the photoexcitation, a portion of the complex relaxes to the ground state by the internal conversion with the time constant of $1/k_1 = 7.7 \pm 0.3$ ps. The rest of the excited species undergoes the chirality flip with the time constant of $1/k_2 = 10.4 \pm 0.5$ ps and goes back to the ground state with $1/k_3 = 171 \pm 6$ ps. From the fitting analysis, the temporal change of each state is obtained as shown

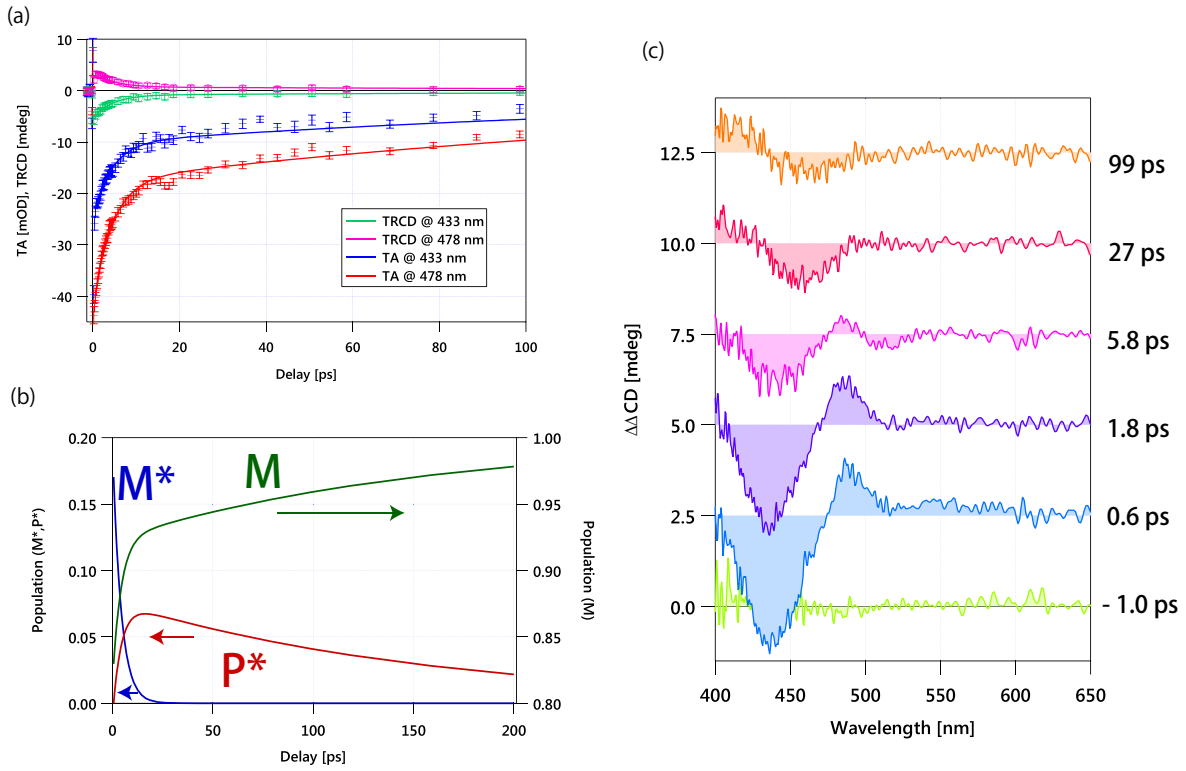

Figure 4.11: (a) Circles: Observed TRCD data at 433 and 478 nm, Crosses: Observed TA data at 433 and 478 nm. Solid lines are reproduced curves by the fitting using Eqs. (4.21, 4.22). (b) Temporal evolution of each state calculated by the fitting analysis. (c) TRCD spectra of BR-HSA complex at pH=4.0 after subtracting the GSB contribution.

in Fig. 4.11 (b). By the excitation, 17% of M is excited to M*. The population of M* immediately relaxes to either M or P*, where the branching ratio is determined by k_1/k_2. In the longer delay, the recovery of M is synchronized with the decay of P*.

In the current model, the time-resolved spectra are assumed to be the superposition of the spectra of M, M*, and P*. Among them, the spectral shape of M is the same as that of the ground-state spectrum without doubt. Thus, the subtraction of the ground-state CD spectra multiplied by $1-[\mathrm{M}](t)$ from the observed TRCD spectra should give the CD spectra of M* and P*. TRCD spectra after the subtraction of the GSB are shown in Fig. 4.11 (c). One can clearly see the sign reversal of the excited-state CD.

Table 4.1: Parameters obtained by the fitting analysis

k_1 [/ps]	k_2 [/ps]	k_3 [/ps]	
0.129 ± 0.005	0.096 ± 0.004	0.0058 ± 0.0002	
R	$CD_{\mathrm{P}^*,433\mathrm{nm}}$ [mdeg]	$CD_{\mathrm{P}^*,478\mathrm{nm}}$ [mdeg]	[M*]$(t=0)$
0.875 ± 0.003	1.1 ± 2.4	-14.8 ± 1.9	0.170 ± 0.002

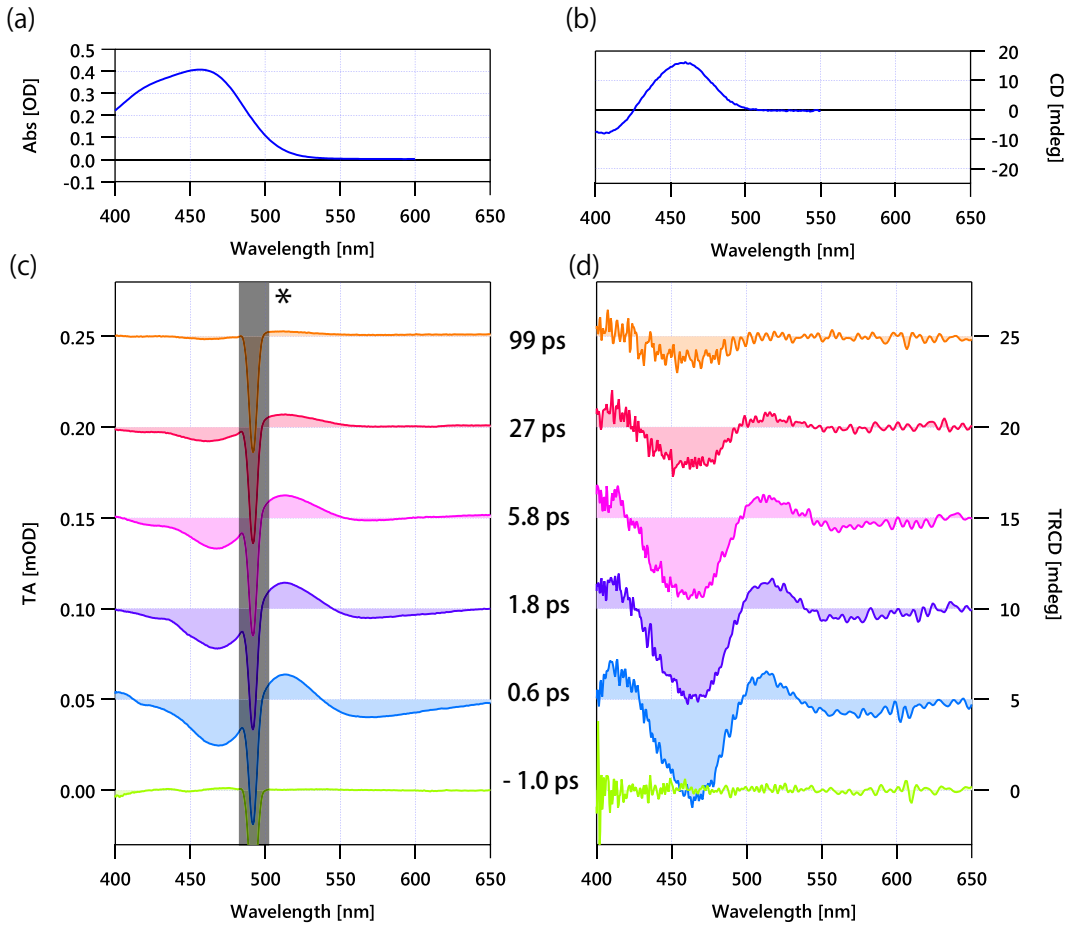

Figure 4.12: Steady-state (a) absorption and (b) CD spectra of the BR-HSA complex (100 μM) at pH=7.8. (c) TA and (d) time-resolved CD spectra of the BR-HSA complex (100 μM) at pH=7.8 after photoexcitation at 490 nm. * Negative peak due to strong scattering from the pump radiation is observed in the hatched region.

4.4.2 TA and TRCD spectra of BR-HSA complex at pH=7.8

I have performed the series of measurements also for BR-HSA complex at pH=7.8. The sample was prepared with basically the same procedure, but the final pH value was adjusted with Tris-HCl buffer solution. The observed TA and TRCD spectra are shown in Fig. 4.12, in which the measurement conditions were the same as those at pH=4.0 except for the pH value. Spectral feature of the TA is similar to that observed at pH=4.0, but stronger SE is observed above 530 nm at early delay times at pH=7.8. For the TRCD spectra, the rotational strength of the ESA and SE observed above 500 nm is larger than that at pH=4.0. These differences imply the excited state dynamics is significantly different between at pH=4.0 and pH=7.8.

The temporal changes of the TA and TRCD at 464 nm are plotted in Fig. 4.13. At pH=7.8, differently from those at pH=4.0, both the TA and TRCD decay single exponentially with the time constant of 16 ps. Here, one notes the TA and TRCD do not decay to zero completely by the single exponential decay. The long-lived ($>$ 1 ns) species was reported in the previous research with the

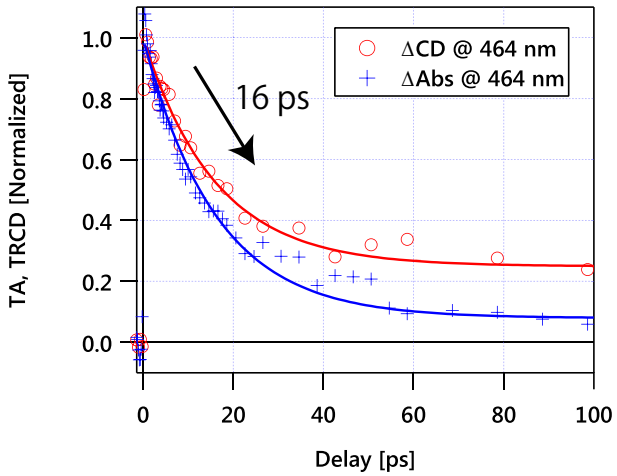

Figure 4.13: Time dependent change of the normalized TA and TRCD at 433 nm.

fluorescence lifetime [25], which they have assigned to the product of the excited-state proton transfer or *trans-cis* isomerization of bilirubin. Now I do not discuss them in detail because the timescale of these dynamics is thought to be much longer than the measurement range in the current experiments.

The simpler model shown in Fig.4.14(a) is considered for the complex at pH=7.8. At pH=7.8, the complex forms P-conformer in the ground state [125]. The single exponential decay indicates that there is no potential barrier over which the complex passes in the excited state like the excited-state dynamics at pH=4.0. Thus, after the photoexcitation, it can be assumed that complex immediately ($<$1 ps) relaxes to the potential well in the excited state and goes back to the ground state with the time constant of 16 ps.

Here it is hard to obtain the temporal change of the population of the excited- and ground-states as was done in Fig. 4.11, because CD and absorption spectra of the metastable state in the excited state are unknown. However, it can be safely assumed that the recovery of the ground-state population is given by a single exponential function with the time constant of 16 ps. The problem is that the initial concentration of the excited state cannot be determined from the data. So I assumed that the amount same as that at pH=4.0 (17 %) is excited by the photoexcitation because the absorption coefficient at 490 nm is almost the same at pH=4.0 and 7.8. The bleach-subtracted CD spectra at pH=4.0 with this assumption are shown in Fig.4.14(b). The spectra show that the shape is time-independent which indicates that the chirality flip does not happen in the excited states. I also calculated the bleach-subtracted spectra with the assumption that 10, 20 and 30 % of the molecules are excited, but no CD spectral change was observed even in these cases.

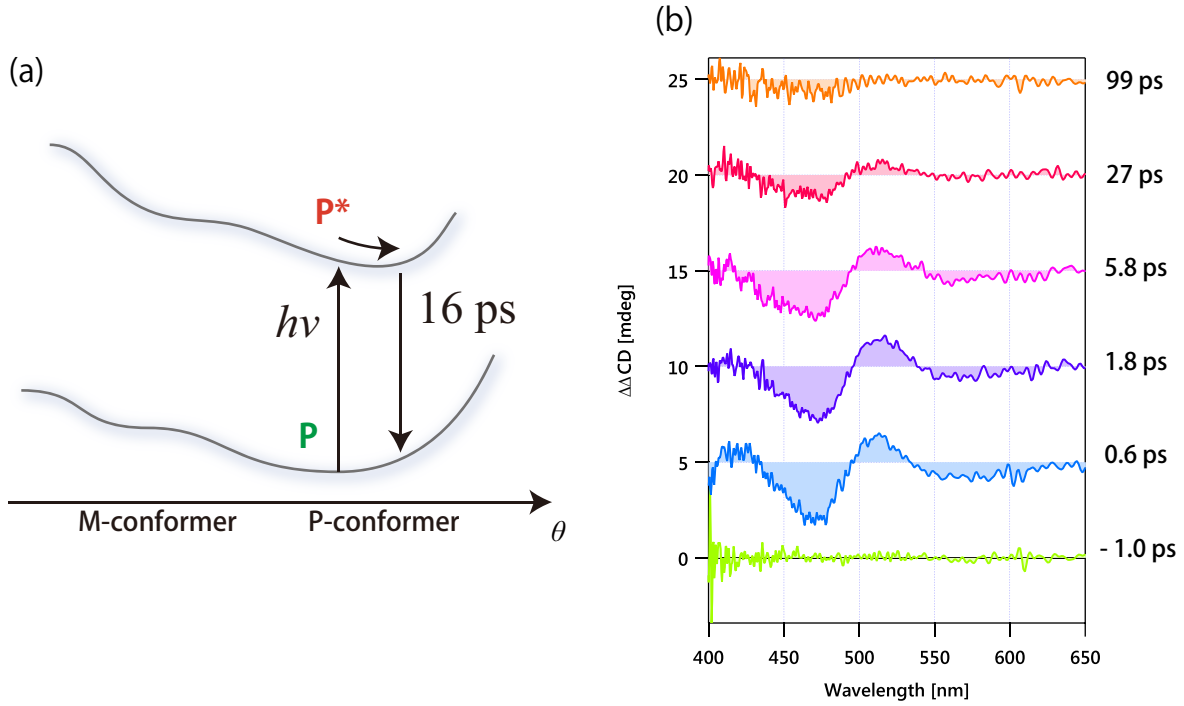

Figure 4.14: (a) A model of excited state dynamics of BR-HSA complex at pH=7.8. (b) TRCD spectra of BR-HSA complex at pH=7.8 after subtracting the GSB contribution.

4.4.3 Comparison with the previous studies

Previously, CD and CPL spectra of BR-HSA complex at pH=4.1, 4.8, 7.4, and 9.0 were measured by Tran *et al* [135, 139]. In general, the sign of CPL spectrum is the same as that of CD spectrum unless the molecule undergoes chirality change [23]. For the BR-HSA complex, the sign of CD and CPL is the same at pH values above 4.8 but is opposite at pH=4.1 [139]. The authors assigned these results to the chirality change in the excited state at pH=4.1, which is consistent with the conclusion obtained by the TRCD spectroscopy here.

In the early time-resolved TA study of BR-HSA complex at pH=7.4 [138], GSB around 470 nm and ESA around 500 nm were clearly observed. They fitted the temporal change both of the GSB and ESA by single exponential functions and determined the lifetime as 19 ± 3 ps, which is consistent with the current results shown in Fig. 4.13. It was concluded that 19-ps decay of the GSB and ESA was associated with trans to cis isomerization of one of the two dipyrrinone groups, which does not accompany the chirality change. The time-resolved spectroscopic study of BR-HSA by Greene *et al.* was followed by that with better time-resolution by Zietz *et al.* [136, 137]. They have reported fluorescence lifetime, and TA of bilirubin mainly in bulk organic solvents and BR-HSA complex was investigated only by fluorescence lifetime, not by TA.

4.5 Conclusion

Excited-state dynamics of BR-HSA complex at pH=4.0 and 7.8 were investigated by femtosecond TRCD and TA spectroscopy. At pH=4.0, both the TA and TRCD decayed bi-exponentially but their decay amplitudes were different, which strongly implied the chirality change in the excited state. The simple three-state model with M, M^* and P^* states, in combination with the exciton coupling theory expanded to transitions from the excited states, well explained the temporal change of TRCD and TA. The results showed bilirubin undergoes chirality flip with the time constant of 10.4 ± 0.5 ps. Chirality flip was more directly confirmed by sign reversal between CD spectra of M^* and P^*, which were extracted by subtracting the GSB from the observed TRCD spectra. At pH=7.8, on the other hand, the bleach subtracted TRCD spectra were almost unchanged over the delay time, which indicate no chirality change happened in the excited state.

To the best of my knowledge, photo-induced ultrafast chirality reversal was directly observed for the first time. The currently studied molecular motion accompanying chirality change is expected to happen widely both in biological systems such as photoisomerization of rhodopsin [144] and in artificial systems such as light-driven molecular rotors [145, 146]. Ultrafast CD spectroscopy is expected to unravel mechanisms of such dynamics and provide a guiding principle for synthesizing new systems to drive motions accompanying chirality change.

Part III

CARS-ROA spectroscopy

Chapter 5

Development of Raman optical activity spectroscopy by coherent Raman scattering

5.1 Introduction

Vibrational optical activity (VOA) such as vibrational circular dichroism (VCD) and Raman optical activity (ROA) has proven to provide a powerful method for determining absolute configuration of chiral molecules and for investigating molecular conformation of biomolecules [27, 28, 83, 147, 148]. Time-resolved VOA, which combines VOA and the pump-probe technique, has a potential to trace the structural evolution of chiral molecules during various bio-processes. Pulsed measurements of VCD and vibrational optical rotatory dispersion (VORD) have already been reported using a femtosecond laser source [71]. On the other hand, ROA measurements with pulsed lasers have not been performed so far. In typical ROA measurements, small (typically 10^{-3} of the Raman intensity) intensity differences between right and left circularly polarized incident or/and scattered Raman radiation are measured. This small ratio of the ROA signal to the achiral background makes the time-resolved ROA measurement difficult because the signal is easily overwhelmed by the background fluctuation.

One possible solution to this problem is to employ nonlinear Raman processes such as coherent anti-Stokes Raman scattering (CARS). ROA measurements with CARS have been proposed by Bjarnason *et al.* and Oudar *et al.*, theoretically [79, 80]. The CARS-ROA approach detects CARS radiation originating from the third-order optical susceptibility components that are negligible in the electric dipole approximation but are significant in the framework including the electric dipole-electric quadrupole or electric dipole-magnetic dipole contributions. In the CARS-ROA scheme, the achiral background can be suppressed by polarization-selective CARS measurement because the polarization of the chirality-induced CARS signal is orthogonal to that of the achiral background. Moreover,

CARS-ROA should be more advantageous than spontaneous ROA in the aspect of accessibility to fluorescent samples. However, CARS-ROA signals are estimated to be about 6 orders of magnitude smaller than typical achiral CARS signals [80]. Therefore, a CARS spectrometer with a high sensitivity and a high polarization selectivity is necessary for the CARS-ROA measurement. Recently, multiplex CARS technique has rapidly evolved with the use of a broadband white-light laser pulse generated from a photonic crystal fiber (PCF) [149–151]. Multiplex CARS spectra with high signal to noise ratio can now be obtained without wavelength scanning [152]. In the present Chapter, we report the observation of the CARS-ROA signal with heterodyne-detected polarization-resolved multiplex CARS spectroscopy. To the best of my knowledge, this is the first report of CARS-ROA, as well as the first ROA observation with a pulsed laser source.

5.2 Basic theory

The third-order optical susceptibility of the CARS process is given by the sum of the nonresonant background and the vibrationally resonant terms[1],

$$\chi_{ijkl}(2\omega_1 - \omega_2; \omega_1, \omega_1, -\omega_2) = \chi^{\mathrm{NR}}_{ijkl} + \chi^{\mathrm{R}}_{ijkl}. \tag{5.1}$$

The vibrationally resonant part is written as

$$\chi^{\mathrm{R}}_{ijkl} = \frac{NR_{ijkl}}{2\hbar(\Omega - \omega_1 + \omega_2 - i\Gamma)}, \tag{5.2}$$

where N is the number of molecules per unit volume, Ω is the frequency of a Raman active vibrational mode, ω_1 and ω_2 are the frequencies of the pump and Stokes incident radiation and Γ is a phenomenological damping constant, respectively. In the electric dipole approximation, R_{1111} and R_{2111} can be written as $R_{1111} = 2a^2 + 8\gamma^2/45$ and $R_{2111} = 0$, where a and γ are the isotropic and anisotropic rotational invariants of the polarizability tensor, respectively. No information about molecular chirality is contained in these invariants. Beyond the electric dipole approximation, as derived in Section 2.3.3, the electric dipole-electric quadrupole and electric dipole-magnetic dipole interactions give non-zero values of the R_{2111} component for the optical activity tensor invariants [79, 80]:

$$R_{1111} = 2a^2 + \frac{8\gamma^2}{45}, \tag{5.3}$$

$$R_{2111} = -4in\Big(aG' + \frac{\gamma_G^2}{45}\Big) + \frac{2in\gamma_A^2}{135c}\Big(1 - \frac{\omega_1 - \omega_2}{2\omega_1}\Big), \tag{5.4}$$

where G' is the isotropic invariant of the electric dipole-magnetic dipole optical activity tensor products, γ_G and γ_A are the anisotropic invariants of the electric dipole-magnetic dipole and electric dipole-

[1] In this chapter, the laboratory coordinates are given by 1, 2, 3 ($i, j, \cdots$ for dummy indices)

electric quadrupole optical activity tensor products, respectively [83].

In spontaneous ROA experiments, the dimensionless circular intensity difference(CID) is measured. The CID is defined as $\Delta = (I_R - I_L)/(I_R + I_L)$. Here I_R and I_L are the Raman intensities obtained with the right- and left-circularly polarized incident light. The CID for forward (0°) scattering is written in terms of the tensor invariants [83, 153]:

$$\Delta(0^\circ) = \frac{4n(45aG' + \gamma_G^2 - \gamma_A^2/6c)}{45a^2 + 7\gamma^2}. \tag{5.5}$$

By comparing eqs. (5.4) and (5.5), R_{2111} is approximated by the product of $\Delta(0^\circ)$ and R_{1111}

$$R_{2111} \simeq -\frac{i}{2}\Delta(0^\circ)R_{1111}. \tag{5.6}$$

Thus, the third-order susceptibilities are expressed as

$$\chi_{1111} = \chi_{1111}^{\mathrm{NR}} + \sum_{i=1}^{n} \frac{A_i}{\Omega_i - \omega_1 + \omega_2 - i\Gamma_i}, \tag{5.7}$$

$$\chi_{2111} \simeq \chi_{2111}^{\mathrm{NR}} + \sum_{i=1}^{n} \frac{-i\Delta_i(0^\circ)A_i/2}{\Omega_i - \omega_1 + \omega_2 - i\Gamma_i}. \tag{5.8}$$

If the polarizations of the two incident beams are parallel to each other, the observed CARS spectrum is formulated as follows:

$$I(\omega_1 - \omega_2, \theta) \propto |\cos(\theta - \theta_0)\chi_{2111} + \sin(\theta - \theta_0)\chi_{1111}|^2 \tag{5.9}$$

$$= \cos^2(\theta - \theta_0)|\chi_{2111}|^2 + \sin^2(\theta - \theta_0)|\chi_{1111}|^2 + 2\cos(\theta - \theta_0)\sin(\theta - \theta_0)\mathrm{Re}(\chi_{2111}^*\chi_{1111}), \tag{5.10}$$

where the definition of the angle difference $\theta - \theta_0$ is depicted in Fig. 5.1(a). In the present study, θ_0 is set to be close to zero. In Eq. (5.10), the first and second terms correspond to the homodyne-detected signal of the chiral and achiral components, respectively. The last cross term in Eq. (5.10) expresses the interference between the achiral and chiral signals. By using the achiral signal as a local oscillator (LO), the detection sensitivity to the chiral signal can be enhanced through the scheme of heterodyne detection. Heterodyne detection enables us to retrieve the phase of the chiral signal, which corresponds to the signs of Δ_i in Eq. (5.8). We can simply extract the cross-term in Eq. (5.10) as a difference spectrum between $\theta = \theta_0 + \theta_1$ and $\theta = \theta_0 - \theta_1$ as

$$I(\omega_1 - \omega_2, \theta_0 + \theta_1) - I(\omega_1 - \omega_2, \theta_0 - \theta_1) \propto 2\sin\theta_1\cos\theta_1\mathrm{Re}(\chi_{2111}^*\chi_{1111}) \tag{5.11}$$

$$= \sum_{i=1}^{n} \frac{2\chi_{1111}^{\mathrm{NR}}\Delta_i A_i \Gamma_i \sin\theta_1}{(\Omega_i - \omega_1 + \omega_2)^2 + \Gamma_i^2}. \tag{5.12}$$

In Eq. (5.12), $\chi^{\mathrm{NR}}_{2111}$ is assumed to be 0 for simplicity. On the other hand, spontaneous ROA line shape is written as follows:

$$I_R(\omega) - I_L(\omega) \propto \sum_{i=0}^{n} \frac{\Delta_i A_i \Gamma_i}{(\Omega_i - \omega)^2 + \Gamma_i^2}. \tag{5.13}$$

Eqs. (5.12) and (5.13) suggest that the spontaneous ROA spectrum in the forward scattering and the difference CARS spectrum between $\theta = \theta_0 \pm \theta_1$ provide the same spectral profile.

5.3 Experimental

The schematic diagram of our heterodyne-detected polarization-resolved multiplex CARS system is shown in Fig. 5.1 (b). The laser source is a passively Q-switched sub-nanosecond 1064 nm microchip laser with a repetition rate of 33 kHz. The output of the laser is divided into two. One is used as the narrow band pump pulses of the CARS process. The other is introduced into a 6-m long air-silica PCF to generate a supercontinuum (white-light laser) with $>$100 μW/nm spectral power density from 1.05 μm to 1.6 μm and is used as the broadband Stokes pulses of the CARS process. After eliminating the anti-Stokes spectral component of the pump and Stokes pulses with several filters, the two pulses propagate collinearly, and are superimposed at the sample with an achromatic lens (AC254-100-C, Thorlabs). The polarizations of the two incident beams are set parallel to each other by a Gran-Taylor prism just before the sample. The polarization of the generated CARS field is selected by an analyzer (Gran-Taylor prism) just after the sample. For the precise polarization selection of the CARS field, the analyzer is mounted on a motorized rotational stage (SGSP-60YAW-0B, Sigma Koki). The angle of the analyzer can be controlled with a minimum increment of 0.0025° and with repeatability of 0.02°. After selecting the polarization of the generated CARS field, the incident beams are spectrally blocked by a notch filter and a short-pass filter. Finally, the CARS radiation is introduced into a polychromator (LS785, Princeton Instruments) and is detected by a CCD camera (PIXIS 100BR eXcelon, Princeton Instruments). In order to evaluate our CARS-ROA system, we performed proof-of-principle experiments on liquid (-)-β-pinene. Liquid (-)-β-pinene was purchased from Aldrich and used as received. The sample was set in a quartz cell with a path-length of 1.0 mm. The pulse energies of the pump and Stokes radiation were 6 μJ and 2 μJ, respectively.

5.4 Results and discussion

5.4.1 Polarization-resolved CARS spectra

Figure. 5.2 shows a series of polarization-resolved CARS spectra of liquid (-)-β-pinene at the analyzer angle $\theta = 10.0^\circ$ and at $\theta = -0.075^\circ$ to 0.075° with 0.025° increments. The collection time for the

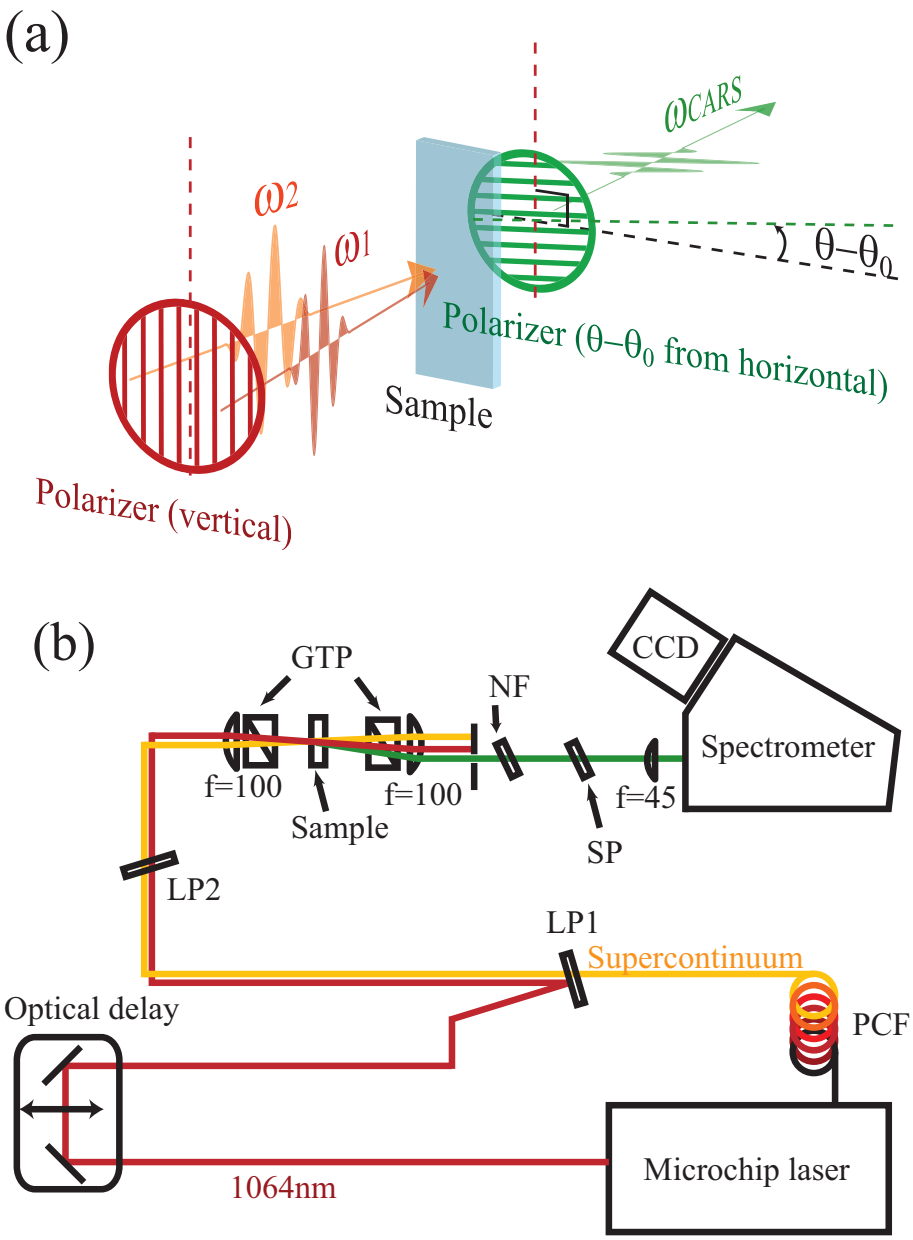

Figure 5.1: (a) Schematics of the experimental configuration around the sample. θ represents the angle of the analyzer and θ_0 is the angle at which the polarizers before and after the sample are perpendicular. (b) Schematic of our heterodyne-detected polarization-resolved CARS spectroscopic system: LP1, 1064nm long-pass filter; LP2, 1050nm long-pass filter; GTP, Gran-Taylor Prisms; NF, 1064nm notch filter; SP, 1050nm short-pass filter. The polarizations of the indent and CARS radiation are precisely (extinction ratio $\sim 1:10^{-7}$) set by Gran-Taylor prisms.

CARS spectrum with $\theta = 10.0^\circ$ is 100 seconds (100 times accumulation of one second exposure) and 30 minutes for the other spectra (from $\theta = -0.075^\circ$ to 0.075°). The spontaneous anti-Stokes Raman scattering signal generated by the pump pulse was subtracted from all the spectra. After this subtraction, all the spectra were divided by the non-resonant background spectrum obtained from water to compensate the spectral profile of the Stokes pulse.

5.4.2 Fitting analysis

Based on the previous report [155], the 716 cm^{-1} and 767 cm^{-1} Raman bands of (-)-β-pinene have large ROA in the forward scattering. Therefore, we focus on the spectral region ranging from 600 cm^{-1} to 800 cm^{-1}. We do not obtain the homodyne chiral component (the first term in Eq. (5.10)) around $\theta = 0^\circ$, which indicates that the homodyne chiral signal is overwhelmed by the noise of the background signal. In order to extract the ROA signal, we analyze the spectra according to the following procedure. First, we determine the parameters $\chi^{\rm NR}_{1111}$ and A_i, Ω_i, Γ_i for the three peaks, where the indices $i = 1, 2, 3$ denote the Raman modes at 640 cm^{-1}, 716 cm^{-1} and 767 cm^{-1}, respectively, by fitting the CARS spectrum at $\theta = 10.0^\circ$ with the second term in Eq. (5.10). For $\theta = 10.0^\circ$, the chiral signal is negligible in comparison with the achiral signal (the second term $\gg$ the first and third terms). Next, using these parameters, all the seven spectra we observed from $\theta = -0.075^\circ$ to $\theta = 0.075^\circ$ with 0.025° increments are fitted simultaneously by the following equation:

$$\begin{aligned} I(\omega_1 - \omega_2, \theta) =& C_{\rm main}|\chi_{2111} + \sin(\theta - \theta_0)\chi_{1111}|^2 \\ &+ C_{\rm leak}|\chi_{1111}|^2, \end{aligned} \tag{5.14}$$

where $C_{\rm main}$ and $C_{\rm leak}$ represent the magnitudes of the spectral component properly oriented by the analyzer and the leaked signal of the large χ_{1111} signal due to the non-zero extinction ratio of the analyzer ($\sim 10^{-7}$), respectively.

The least-squares-fitted results are shown as solid curves in Fig. 5.2. They agree with the observed spectra (shown as circles) very well. The optical activity parameters were determined to be $\chi^{\rm NR}_{2111}/\chi^{\rm NR}_{1111} = 0 \pm 1 \times 10^{-5}$, $\Delta_1 = (0.38 \pm 0.03) \times 10^{-3}$, $\Delta_2 = (-1.17 \pm 0.14) \times 10^{-3}$, $\Delta_3 = (0.52 \pm 0.08) \times 10^{-3}$. It should be noted that Δ_i have significant non-zero values and the signs and the order of these values is consistent with those obtained with the spontaneous ROA study [155]. The fitted results with Δ_i fixed to be zero are also shown as dashed curves in Fig. 5.2. In this case, the fitted results cannot reproduce the experimental results in particular around Ω_2. This fact suggests that the ROA components certainly contribute to the observed CARS spectra.

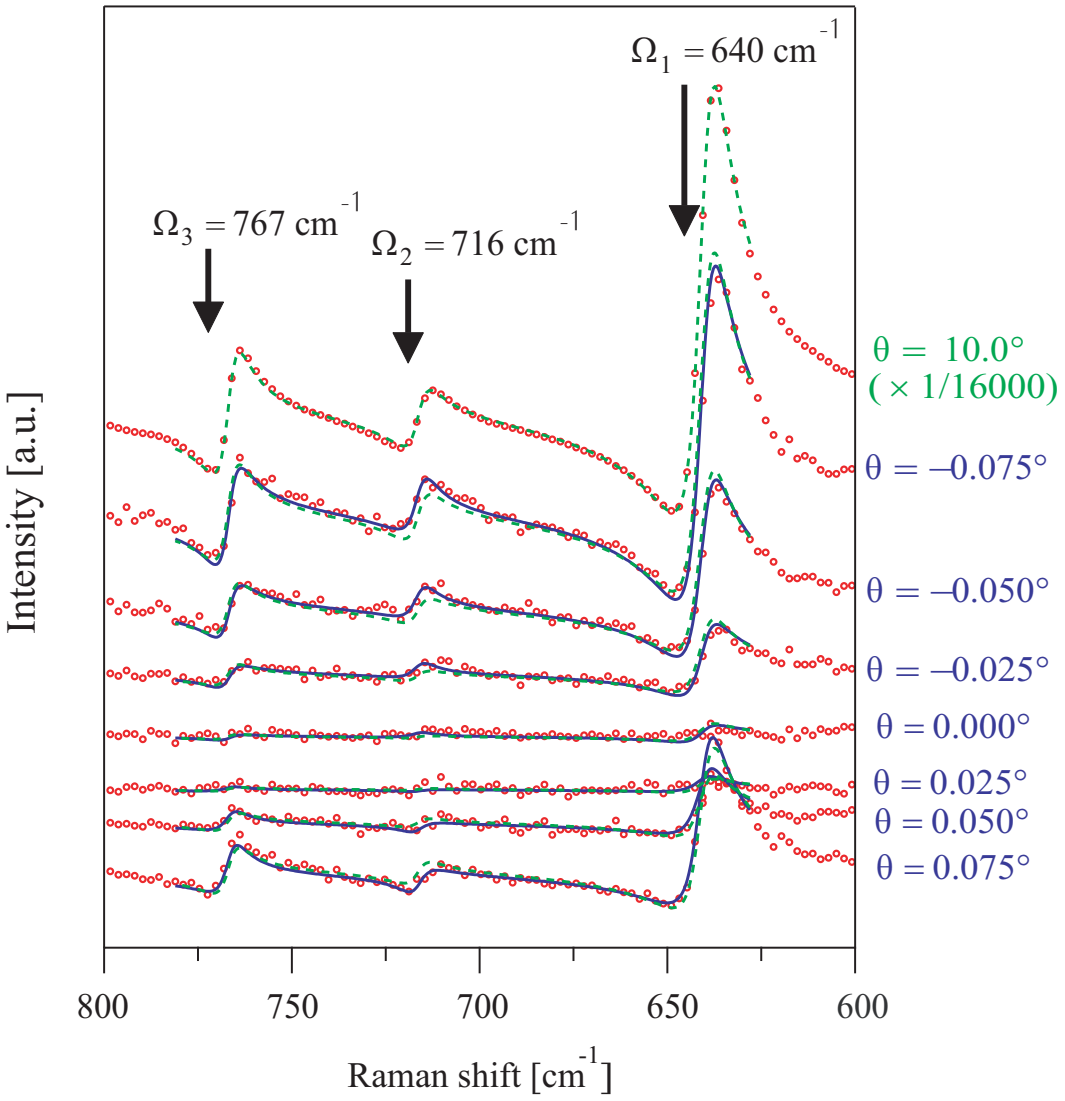

Figure 5.2: Circles: A set of observed polarization-resolved CARS spectra of the liquid (-)-β-pinene. (the collection time; 100 seconds (100 times accumulation of one second exposure) for the spectrum at $\theta = 10.0°$, 30 minutes for the other spectra, the incident power; $\sim$ 200 mW for ω_1 and $\sim$ 70 mW for ω_2) The spectra are normalized by the collection time. The spectrum at $\theta = 10.0°$ is minified by 1/16000.
Dashed lines: Curves fitted by using Eq. (5.14) with χ_{2111} and $C_{\rm leak}$ are fixed to be 0. From the spectrum at $\theta = 10.0°$, the parameters were obtained as $\chi^{\rm NR}_{1111} = 3.2 \times 10^{-14}$ [esu], $\omega_i = 640.39 \pm$ 0.027, 716.28 $\pm$ 0.16, 766.74 $\pm$ 0.80 [cm^{-1}], $A_i = (17.4 \pm 0.1) \times 10^{-14}$, $2.2 \pm 0.1) \times 10^{-14}$, $(4.2 \pm 0.1) \times 10^{-14}$ [esu], $\Gamma_i = 4.94 \pm 0.05$, 3.76 ± 0.25, 3.49 ± 0.13 [cm^{-1}] ($i = 1, 2, 3$ respectively)
Solid lines: Curves fitted by using Eq. (5.14) with free χ_{2111} and $C_{\rm leak}$. From the spectra at $\theta = -0.075°, -0.050° \cdots 0.075°$, the parameters were obtained as $\chi^{\rm NR}_{2111} = 0 \pm 3 \times 10^{-19} \times 10^{-19}$ [esu], $C_{\rm main} = (6.35 \pm 0.03) \times 10^2$, $C_{\rm leak} = (3.65 \pm 0.35) \times 10^{-6}$, $\theta_0 = 0.016° \pm 0.0006°$, $\Delta_1 = (0.38 \pm 0.03) \times 10^{-3}$, $\Delta_2 = (-1.17 \pm 0.14) \times 10^{-3}$, $\Delta_3 = (0.52 \pm 0.08) \times 10^{-3}$. The absolute magnitudes of third-order optical susceptibilities are evaluated by using the value of the nonresonant third-order susceptibility of water as a standard [154].

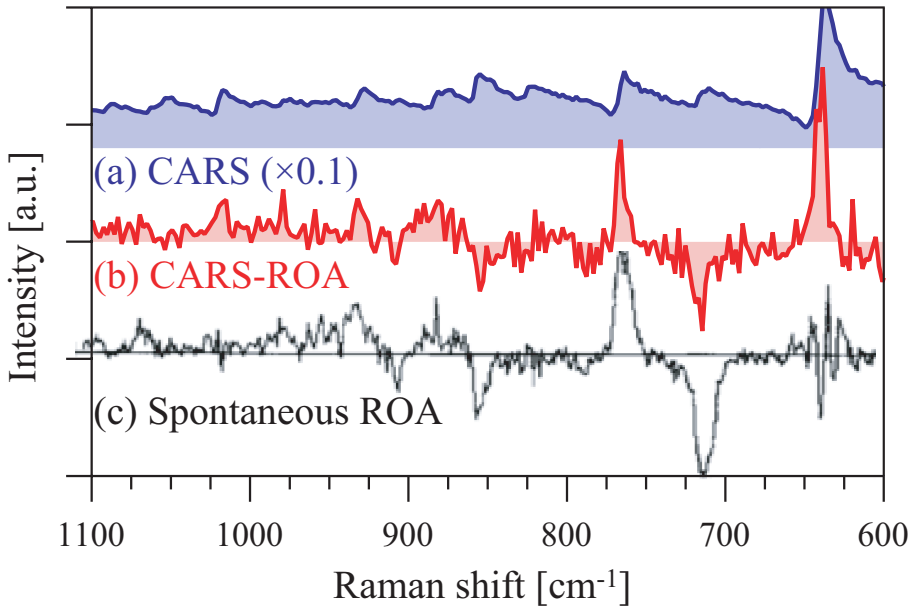

Figure 5.3: (a): The sum of CARS spectra with weight coefficients: $I_{\rm sum} = I(0.075^\circ - \theta_0) + I(-0.075^\circ - \theta_0)\sin(0.075^\circ - \theta_0)/\sin(-0.075^\circ - \theta_0)$
(b): The difference of CARS spectra with weight coefficients: $I_{\rm dif} = I(0.075^\circ - \theta_0) - I(-0.075^\circ - \theta_0)\sin(0.075^\circ - \theta_0)/\sin(-0.075^\circ - \theta_0)$
(c): Spontaneous ROA spectrum reproduced from ref [155] .

5.4.3 Extraction of ROA spectrum

Based on these results, we can extract an ROA spectrum by using Eq. (5.12). The sum and difference spectra between the $\theta = -0.075^\circ$ and $\theta = 0.075^\circ$ spectra with appropriate coefficients are shown in Fig. 5.3 (a) and (b). The coefficients are determined by using Eq. (5.10) so that the sum and difference spectra are proportional to $|\chi_{1111}|^2$ and $\mathrm{Re}(\chi^*_{2111}\chi_{1111})$, respectively. Two ROA peaks at 716 cm^{-1} and 767 cm^{-1} are clearly observed in the spectrum obtained with this procedure. All the spectral features in Fig. 5.3(b) except for 640 cm^{-1} band quantitatively agree with those in the spontaneous ROA spectrum (Fig. 5.3(c)) obtained by Barron *et al* [155]. The band at 640 cm^{-1} is strongly polarized and has been discussed to be unreliable in the ROA study [153, 156].

The contrast between the ROA signal and the achiral background is determined by $|\Delta| = |(I_R - I_L)/(I_R + I_L)|$ in the spontaneous ROA measurement. Those of the 716 cm^{-1} and 767 cm^{-1} Raman bands of (-)-β-pinene are estimated to be around 1×10^{-3}. In our CARS-ROA measurement, the contrast is determined as $2\mathrm{Re}(\chi^*_{2111}\chi_{1111})/(\sin(\theta - \theta_0)|\chi_{1111}|^2)$. Note that the contrast is the function of the parameter of θ that can be controlled experimentally. At $\theta = 0.075^\circ$, the signal to background ratio experimentally determined by the ratios between the peak intensities of the CARS-ROA and CARS spectra are about 1×10^{-1} for the same two peaks (Fig. 5.3(a),(b)).

Besides CARS-ROA, several nonlinear spectroscopic techniques sensitive to molecular chirality have been proposed and developed. Especially, it is worthwhile to compare CARS-ROA with Bio-

CARS, which is a chiral sensitive $\chi^{(4)}$ Raman spectroscopy proposed by Koroteev [157]. Like chiral $\chi^{(2)}$ spectroscopy [90, 94], chirality-induced signal can be obtained without achiral background in BioCARS because even-order nonlinear susceptibilities are zero in the achiral liquid. Up to present, however, BioCARS has not been observed primarily due to the extremely small $\chi^{(4)}$ value (estimated to be 10^{-22} esu). To obtain BioCARS signal of the energy 6×10^{-12} J in each pulse, incident pulses with 1ps pulse-width and 50 μJ pulse energy focused into a spot with diameter 60 μm are needed in the electronically preresonant conditions [157]. In CARS-ROA, the magnitudes of the optically active third-order susceptibilities are estimated to be $|\chi^{\mathrm{R}}_{2111}| = |\Delta\chi^{\mathrm{R}}_{1111}/2| \sim 10^{-17}$ esu in the off-resonance condition. To obtain the CARS-ROA pulse (the signal of the heterodyne term in Eq. (12)) with the same energy as above discussion (6×10^{-12} J in each pulse), incident pulses with 1ps pulse width and only 2 μJ energy are necessary [2].

5.5 Conclusion

In summary, a new technique of ROA based on coherent Raman spectroscopy, heterodyne-detected polarization-resolved CARS spectroscopy is reported in this chapter. This technique is applied to measure the Raman optical activity of liquid (-)-β-pinene successfully, which is the first report not only on CARS-ROA but also on ROA using a pulsed laser. Thanks to the coherent nature of the CARS signal, the large achiral CARS electric field can be used as a local oscillator, and it enables us to extract the amplitude and phase of the weak chiral signal. Our results show that the achiral background can be significantly reduced by adjusting the polarizations, making the measurements robust over fluctuations of an optical system. This technique will be applied to time-resolved ROA measurements for unraveling the dynamics of transient chiral molecules and biomolecules in aqueous solutions, to which infrared VCD is not applicable.

The contents of this chapter were published in Ref. [158].

[2] Estimated by using the formulation of the CARS intensity written in J. F. Reintjes, *Nonlinear Optical Parametric Processes in Liquids and Gases* (Academic Press, New York, 1984). Completely phase matched condition is assumed.

Chapter 6

CARS-ROA spectroscopy by spectral interferometry

6.1 Introduction

In the previous chapter, I reported an ROA measurement system with the small achiral background by using coherent anti-Stokes Raman scattering (CARS-ROA) [158], which opened up the possibility to measure ultrafast ROA spectra. In the reported CARS-ROA method, ROA spectra are measured as follows. Chirality-induced CARS is generated as an electromagnetic field polarized perpendicular to the polarizations of the incident fields, which are parallel to each other. To amplify the exceptionally weak chirality-induced CARS signal, the polarization-resolved heterodyne-detected CARS scheme was employed in the previous setup. In this scheme, the polarizer for the generated CARS radiation was slightly tilted from the perpendicular configuration so that the strong achiral CARS signal was introduced as a local oscillator (LO). The obtained spectral intensity was then proportional to $|\sin\theta\chi_{1111} + \cos\theta\chi_{2111}|^2$, where χ was the third-order optical susceptibility tensor and θ represented the analyzer angle from the perpendicular configuration. By taking difference between CARS spectra at $\theta = \pm\theta_1$, the homodyne terms were canceled out and only the heterodyne term was obtained. The heterodyne term was proportional to χ_{2111} and enabled us to retrieve both the amplitudes and the phases of the chiral signal. Although the contrast ratio of the chiral signal to the achiral background was considerably improved in CARS-ROA in comparison with spontaneous ROA, it was not still easy to obtain an artifact-free CARS-ROA spectrum because residuals of the homodyne term after the spectral subtraction sometimes gave rise to artificial peaks in a CARS-ROA spectrum. Moreover, it has remained unclear in the previous paper how large the optically active non-resonant part of the susceptibility $\chi_{2111}^{\mathrm{NR}}$ contributed to the CARS-ROA spectrum. It was mainly because the previous method was less sensitive to the optically active nonresonant background.

In this Chapter, an interferometric coherent Raman optical activity (iCROA) technique using an ex-

ternal LO is demonstrated. By introducing the external LO, only the heterodyne terms can be extracted by Fourier transform spectral interferometry (FTSI) [107]. FTSI is used to obtain both the amplitude and phase of the generated electric signals in CARS [159, 160], sum frequency generation [161, 162], vibrational/electronic optical activity free induction decay [71, 72]. In iCROA, the chiral signal from a sample is combined with the CARS radiation generated in the LO arm with the time difference τ. The heterodyne terms between the signals from the sample and the reference can then be extracted by Fourier transformation (FT) because fringes with the frequency of $1/\tau$ are incorporated only in the heterodyne terms. By using this scheme, it is shown that a CARS-ROA spectrum can be obtained free from the achiral background of the sample, that the amount of $\chi^{\mathrm{NR}}_{2111}$ is evaluated and shown to be pure imaginary for (-)-β-pinene, and that artificial signals due to optical rotatory dispersion (ORD) of chiral samples are experimentally distinguished.

6.2 Experimental

The schematic diagram of the iCROA setup is shown in Fig. 6.1. The light source is a 1064 nm microchip laser (Hamamatsu, L11435) with a repetition rate of 25 kHz, a pulse width of 400 ps and output power of 20 μJ. The pump and Stokes pulses are narrow-band fundamental and broadband white-light continuum (from 1100 nm to $>$1300 nm) generated by a 2.5-m long photonic crystal fiber (SC-5.0-1040, NKT Photonics), respectively. Incident pulses are divided into two, namely the sample arm and the LO arm, by a half wave plate and polarized beam splitter. Optical configuration of the sample arm is the same as the reported one [158]. The polarizations of pump and Stokes pulses are set parallel to each other by the Glan-Taylor prism placed before the sample. Generated chirality-induced CARS field whose polarization is near perpendicular to the incident polarization is selected by the second Glan-Taylor prism (Fig. 6.2). In the LO arm, CARS field from the reference (water in the present setup) is generated without polarizers and combined with the CARS from the sample with the optical delay of τ. It should be noted that although the polarizations of the incident beams in the two arms are perpendicular after the PBS, the polarizations of the chirality-induced CARS from the sample and the achiral CARS field from the reference are almost parallel and interfere with each other. The reflected and transmitted beams of the BS are dispersed by a polychromator (LS785, Princeton Instruments) and then focused onto the different columns of the CCD camera (PIXIS 100BR eXcelon, Princeton Instruments). The incident energies are 8 μJ (pump in the sample arm), 0.4 μJ (Stokes in the sample arm), 1.5 μJ (pump in the reference arm), and 0.07 μJ (Stokes in the reference arm) at the sample. In order to evaluate our iCROA method, I performed proof-of-principle experiments on liquid (-)-β-pinene. Liquid (-)-β-pinene was purchased from Aldrich and used as received. The sample was set in a quartz cell with a path length of 1.0 mm.

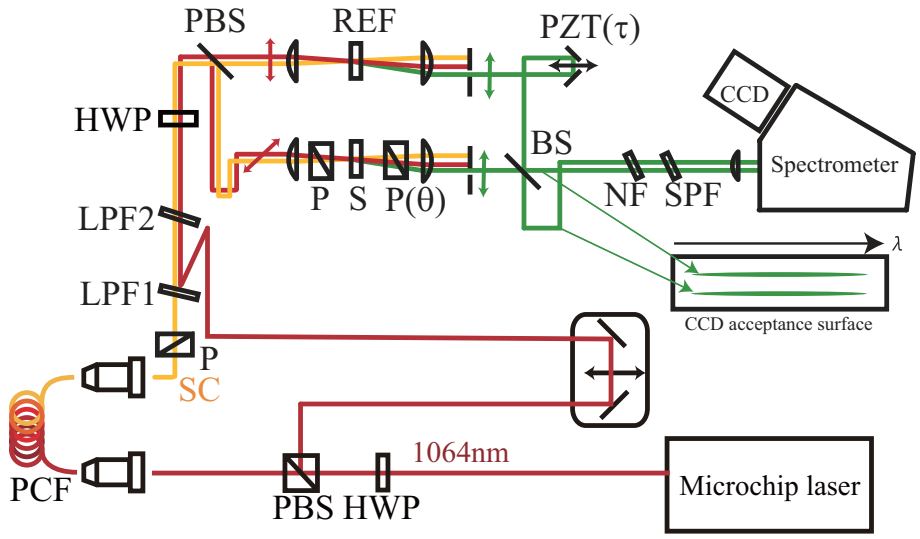

Figure 6.1: Experimental setup. PCF: photonic crystal fiber, PBS: polarized beam splitter, HWP: half wave plate, P: polarizer, LPF1: long pass filter (cutoff @ 1064 nm), LPF2: long pass filter (cutoff @ 1050 nm), REF: reference (water), S: sample ((-)-β-pinene, BS: beam splitter, PZT(τ): piezo stage for optical delay $\tau = \tau_0 + \tau_1 n$, NF: notch filter (1064 nm), SPF: short pass filter (cutoff @ 1050 nm).

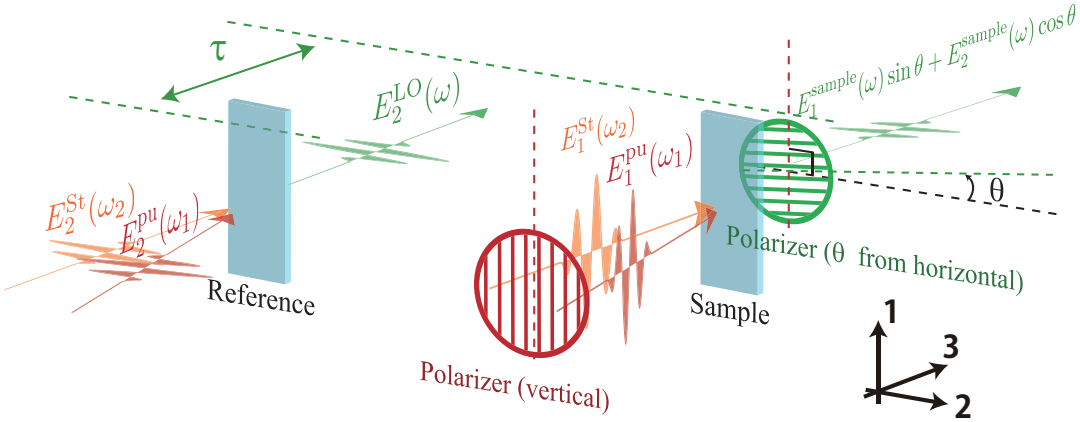

Figure 6.2: Schematic diagram of experimental configuration around the sample and the reference.

6.3 Basic theory

In the polarization configuration depicted in Fig. 6.2, the total electric field in the frequency domain is expressed as a sum of CARS fields generated from the reference and the sample [1]:

$$\begin{aligned} E(\omega,\theta) &= E_1^{\mathrm{sample}}(\omega)\sin\theta + E_2^{\mathrm{sample}}(\omega)\cos\theta + E_2^{\mathrm{LO}}(\omega)e^{-i\omega\tau} \\ &= [A(\chi_{1111}^{\mathrm{sample}}(\omega)\sin\theta + \chi_{2111}^{\mathrm{sample}}(\omega)\cos\theta) + B\chi_{1111}^{\mathrm{LO}}e^{-i\omega\tau}]E_1^{\mathrm{pu}}(\omega_1)E_1^{\mathrm{pu}}(\omega_1)E_1^{\mathrm{St}*}(\omega_2), \end{aligned} \tag{6.1}$$

where $\omega, \omega_1, \omega_2$ represent the angular frequencies of the CARS, pump and Stokes pulses, which satisfy $\omega = 2\omega_1 - \omega_2$, A and B are real positive constants, τ is the time delay between the LO and the CARS field from the sample and the subscripts of E represent the direction of the polarization (in Cartesian coordinates, see Fig. 6.2).

The observed CARS intensity is formulated as the absolute square of the electromagnetic field as

$$\begin{aligned} I(\omega,\theta) &= |E_1^{\mathrm{sample}}(\omega)\sin\theta + E_2^{\mathrm{sample}}(\omega)\cos\theta + E_2^{\mathrm{LO}}(\omega)e^{-i\omega\tau}|^2 \\ &\propto A^2|\chi_{1111}^{\mathrm{sample}}(\omega)|^2\sin^2\theta + A^2|\chi_{2111}^{\mathrm{sample}}(\omega)|^2\cos^2\theta + B^2|\chi_{1111}^{\mathrm{LO}}|^2 \\ &\quad + A^2\sin\theta\cos\theta\mathrm{Re}[\chi_{1111}^{\mathrm{sample}}(\omega)\chi_{2111}^{\mathrm{sample}*}(\omega)] \\ &\quad + AB\sin\theta\mathrm{Re}[\chi_{1111}^{\mathrm{sample}}(\omega)\chi_{1111}^{\mathrm{LO}*}\exp(i\omega\tau)] \\ &\quad + AB\cos\theta\mathrm{Re}[\chi_{2111}^{\mathrm{sample}}(\omega)\chi_{1111}^{\mathrm{LO}*}\exp(i\omega\tau)]. \end{aligned} \tag{6.2}$$

In the previous CARS-ROA study without the external LO [158], the fourth term of Eq. (6.2) has been observed as a chirality sensitive term. The observed raw spectra were mainly dominated by the achiral background $|\chi_{1111}^{\mathrm{sample}}(\omega)|^2$. Thus it has been needed to take difference between spectra at $\theta = \pm\theta_1$ to obtain a CARS-ROA spectrum. In this study, fairly strong external LO is introduced ($A \ll B$) and the raw spectra are dominated by $|\chi_{1111}^{\mathrm{LO}}|^2$, which does not have vibrational peaks.

The last two terms of Eq. (6.2) were extracted by following three procedures:

1. Obtaining both signals transmitted and reflected by the beam splitter and taking difference spectrum between them.

2. Modulating the time difference as $\tau = \tau_0 + \tau_1 n$ (n represents the data number) by moving the piezo stage and performing Fourier transformation to extract only the modulated components.

3. Extracting $t = \tau_0$ component by multiplying window function by the time domain interferogram (FTSI [107]).

[1] Although the LO term should be written as $E_2^{\mathrm{LO}}(\omega)e^{-i\omega\tau}\cos\theta$ in a precise sense, $\cos\theta$ can be approximated by 1 because θ changes between -0.125° and 0.125° in this study.

By the above procedures, only the positive time delay components of the Eq. (6.2):

$$S(\omega,\theta) = \sin\theta\chi_{1111}^{\mathrm{sample}}(\omega)\exp(i\omega\tau_0) + \cos\theta\chi_{2111}^{\mathrm{sample}}(\omega)\exp(i\omega\tau_0) \tag{6.3}$$

are extracted.

6.4 Results and discussion

6.4.1 Direct observation of χ_{2111}

In order to extract the heterodyne term, 20 spectra with different time delay τ were measured. Then the extracted spectra of the heterodyne term were averaged over 150 times to increase the signal to noise ratio. With 4.8 s exposure time of a single raw spectrum, the total collection time to obtain the final spectrum $S(\omega,\theta)$ was 4.2 h for one polarizer angle θ. The magnitudes of the extracted heterodyne terms at $\theta = 0.000^\circ$ and $\theta = -0.125^\circ$ are shown in Fig. 6.3(a). At $\theta = -0.125^\circ$, the achiral homodyne CARS line shape is observed. The spectral profile of the achiral CARS is formulated by

$$\begin{aligned}|\chi_{1111}| &= \left(\left|\chi_{1111}^{\mathrm{NR}} + \frac{A}{\Omega-\omega_{\mathrm{R}}-i\Gamma}\right|^2\right)^{\frac{1}{2}} \\ &= \left((\chi_{1111}^{\mathrm{NR}})^2 + \frac{2\chi_{1111}^{\mathrm{NR}}A(\Omega-\omega_{\mathrm{R}})}{(\Omega-\omega_{\mathrm{R}})^2+\Gamma^2} + \frac{A^2}{(\Omega-\omega_{\mathrm{R}})^2+\Gamma^2}\right)^{\frac{1}{2}},\end{aligned} \tag{6.4}$$

where A, Ω, and Γ are the amplitude, the frequency, and the damping constant of the Raman active vibrational mode, respectively, $\omega_{\mathrm{R}} = \omega - \omega_1$ is Raman shift. The dispersive line shape of the spectrum is due to the second term in the square root and the phases of all the peaks are the same because A is positive for all the bands. In $|S(\omega, 0.000^\circ)|$ spectrum, four peaks at 640 cm^{-1}, 717 cm^{-1}, 767 cm^{-1}, 855 cm^{-1} are clearly observed. These peaks have also the dispersive line shape but the phases of each peak are not monosignate. Namely, the phases of 717, 855 cm^{-1} are the same as the phases of the achiral CARS spectrum and the phases of the other peaks are opposite. The spectrum at $\theta = 0.000^\circ$ is formulated as

$$|\chi_{2111}| = \left(|\chi_{2111}^{\mathrm{NR}}|^2 + \frac{\mathrm{Im}(\chi_{2111}^{\mathrm{NR}})\Delta A(\Omega-\omega_{\mathrm{R}})}{(\Omega-\omega_{\mathrm{R}})^2+\Gamma^2} + \frac{\Delta^2A^2/4}{(\Omega-\omega_{\mathrm{R}})^2+\Gamma^2}\right)^{\frac{1}{2}}, \tag{6.5}$$

where, Δ is the circular intensity difference measured in forward-scattered spontaneous ROA studies [83, 147]. In Eq. (6.5), $\chi_{2111}^{\mathrm{NR}}$ is assumed to be pure imaginary, which is experimentally verified below. The different phases of each peak of $|S(\omega, 0.000^\circ)|$ are explained by the fact that the signs of Δ are different in general for different peaks.

The real and imaginary parts of the extracted $S(\omega,\theta)$ spectra of (-)-β-pinene at $\theta = -0.125^\circ, 0.000^\circ$, and 0.125° are shown in Fig. 6.3(b). The interference fringes of Fig. 6.3(b) are due to the time

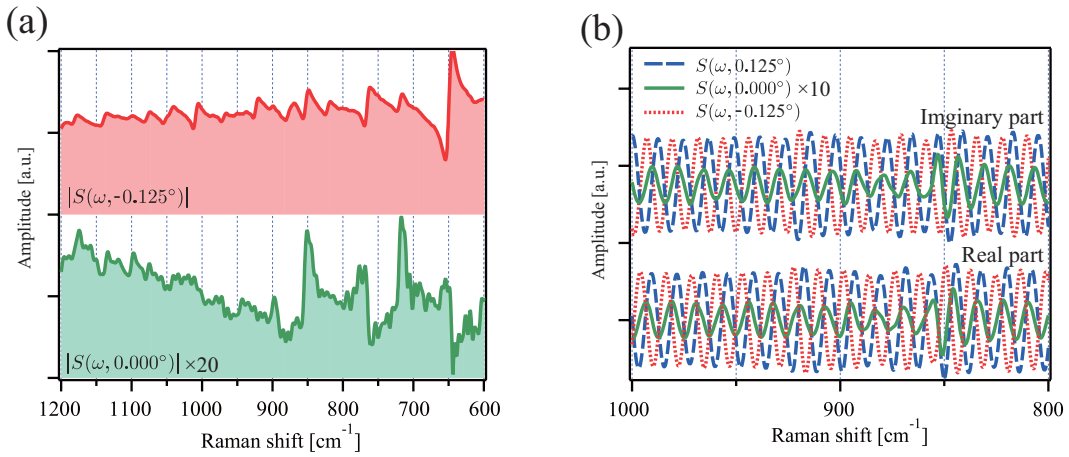

Figure 6.3: (a): $|S(\omega,\theta)|$ spectra of (-)-β-pinene at $\theta = -0.125°$(top, red) and $0.000°$ (bottom, green). (b)Imaginary(top) and real(bottom) parts of $S(\omega,\theta)$ spectra of (-)-β-pinene at $\theta = -0.125°$ (red dotted line), $0.000°$ (green solid line) and $0.125°$ (blue dashed line).

delay τ_0 ($\simeq$ 1.8 ps in this study). The fringes of the spectra at $\theta = \pm 0.125°$ are obviously in anti-phase. It is because the first term of Eq. (6.3) is dominant in $S(\omega, \pm 0.125°)$ and is odd function of θ. The oscillation feature is also found in the $S(\omega, 0.000°)$ spectrum. The phase of $S(\omega, 0.000°)$ in the spectral range without vibrational peaks is different by $\mp\pi/2$ from those of $S(\omega, \pm 0.125°)$. Considering the fact that $\chi^{\mathrm{NR}}_{1111}$ is real, it can be concluded that $\chi^{\mathrm{NR}}_{2111}$ is pure imaginary. The value of $\chi^{\mathrm{NR}}_{2111}$ relative to $\chi^{\mathrm{NR}}_{1111}$ is calculated as $\chi^{\mathrm{NR}}_{2111} \simeq -9 \times 10^{-5} \times \chi^{\mathrm{NR}}_{1111} i$ by taking the average value of $\sin(0.125°)S(\omega, 0.000°)/S(\omega, 0.125°)$ over the frequency range without vibrational peaks. This result is consistent with our previous estimation ($|\mathrm{Im}(\chi^{\mathrm{NR}}_{2111}/\chi^{\mathrm{NR}}_{1111})| < 4 \times 10^{-4}$) in the supporting information of Ref. [158]. The capability to detect the sign and absolute magnitude of this term provides a possibility to investigate the excited electronic states by iCROA. It should be noted that the optically active non-resonant background is definitely distinguishable from the achiral non-resonant background due to experimental imperfections such as non-zero extinction ratio of the analyzer. It is because $\pi/2$ phase difference of the non-resonant background cannot be explained only by the first term of Eq. (6.3).

6.4.2 Extraction of ROA spectrum and compensation of artificial signal due to ORD

The CARS-ROA spectrum is obtained as [158]

$$\mathrm{Re}(\chi^*_{1111}\chi_{2111}) = \sum_{i=1}^{n} \frac{(\Delta_i \chi^{\mathrm{NR}}_{1111} + \mathrm{Im}(\chi^{\mathrm{NR}}_{2111}))A_i\Gamma_i}{(\Omega_i - \omega_{\mathrm{R}})^2 + \Gamma_i^2}. \tag{6.6}$$

If ORD of the sample is negligible in the whole spectral range, CARS-ROA can be obtained as $\mathrm{Re}[S(\omega, 0.000°)S^*(\omega, 0.125°)] \propto \mathrm{Re}(\chi^*_{1111}\chi_{2111})$. If this is not the case, $\mathrm{Re}[S(\omega, 0.000°)S^*(\omega, 0.125°)]$

spectrum includes not only CARS-ROA but also the achiral CARS components;

$$\begin{aligned}\mathrm{Re}[S(\omega, 0.000^\circ)S^*(\omega, 0.125^\circ)] &\simeq \mathrm{Re}[\sin(0.125^\circ)\chi_{1111}e^{i\omega\tau}(\chi^*_{2111} + \sin\alpha(\omega)\chi^*_{1111})e^{-i\omega\tau}] \\ &\propto \mathrm{Re}(\chi^*_{1111}\chi_{2111}) + \sin\alpha(\omega)|\chi_{1111}|^2, \end{aligned} \tag{6.7}$$

where $\alpha(\omega)$ represents the ORD. It should be noted that $\alpha(\omega)$ represents the ORD both of the Stokes and of the CARS radiation. The CARS-ROA spectrum of (-)-β-pinene is shown in the top of Fig. 6.4. A broad offset due to the second term of Eq. (6.7) is observed in the whole spectral range. The offset can be canceled by subtracting the achiral contribution with an appropriate coefficient $c(\omega)$ as

$$\begin{aligned} S'(\omega, 0.000^\circ) &= S(\omega, 0.000^\circ) - c(\omega)S(\omega, 0.125^\circ) \\ &\propto \chi_{2111}\exp(i\omega\tau). \end{aligned} \tag{6.8}$$

The coefficient is assumed to be a spline function and determined by fitting so that the phase of $S'(\omega, 0.000^\circ)/S(\omega, 0.125^\circ)$ is equal to $-\pi/2$ in the range without vibrational peaks. After the compensation, the CARS-ROA spectrum is calculated as $\mathrm{Re}[S'(\omega, 0.000^\circ)S^*(\omega, 0.125^\circ)]$, which is shown in the bottom of Fig. 6.4. The broad offset due to the ORD is substantially reduced by using the phase information of the non-resonant background signal.

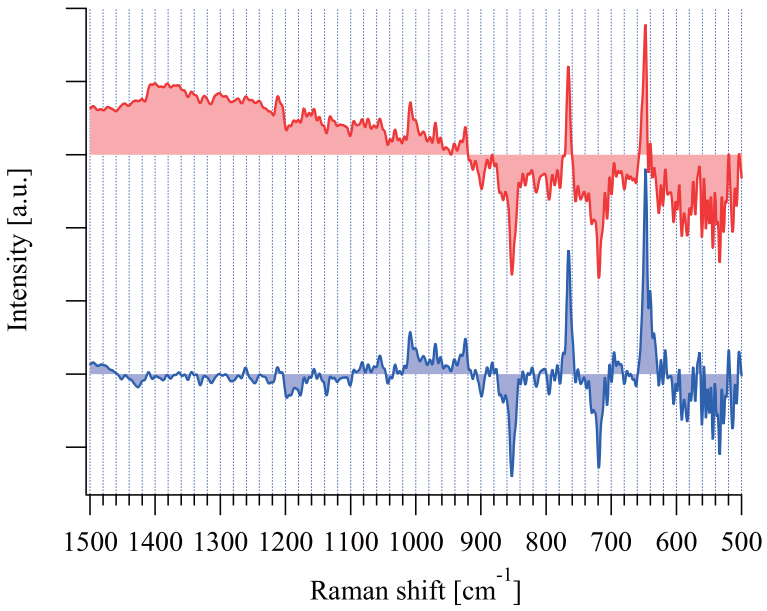

Figure 6.4: CARS-ROA spectra of (-)-β-pinene before (top) and after (bottom) the compensation to cancel the achiral contribution. The top spectrum is calculated as $\mathrm{Re}[S(\omega, 0.000^\circ)S^*(\omega, 0.125^\circ)]$ and the bottom one is calculated as $\mathrm{Re}[S'(\omega, 0.000^\circ)S^*(\omega, 0.125^\circ)]$.

6.5 Conclusion

I have reported a novel CARS-ROA measurement method with CARS spectral interferometry, iCROA. Only the heterodyne terms between the CARS fields from the sample and the reference are selectively extracted by the analyses. The non-resonant background susceptibility is shown to be pure imaginary and the sign and the magnitude is also determined for (-)-β-pinene. The artifact due to the ORD of the chiral sample is reduced by exploiting the phase sensitivity of iCROA.

The contents of this chapter were reported in Ref. [109].

Chapter 7

Visible-excited multiplex CARS-ROA spectroscopy

7.1 Introduction

I reported novel ROA spectroscopy with using coherent anti-Stokes Raman scattering (CARS-ROA) in the previous chapters. In CARS-ROA spectroscopy, both the phase and amplitude of CARS radiation polarized perpendicular to the incident polarization is measured with a heterodyne technique, in which achiral CARS field generated from the sample itself or external reference material was used as a local oscillator. One of the most striking advantages of CARS-ROA spectroscopy over conventional spontaneous ROA spectroscopy is its higher contrast ratio of the chirality-induced signal to the achiral background. In the previous setups, it was demonstrated that the contrast ratio of CARS-ROA measurement of β-pinene is two orders of magnitudes higher than that of spontaneous ROA measurement [158]. This improvement is significantly important in view of a future application to time-resolved ROA spectroscopy, which is a great challenge because the time-dependent change of extremely weak ROA signal needs to be extracted from its huge achiral background. In order to improve the detection sensitivity by compensating the laser fluctuation, scattered circularly polarized (SCP)-ROA spectroscopy has been reported [163]. However, this technique still requires the extraction of the weak ROA signal from the huge achiral background *after* the signal detection. On the other hand, our CARS-ROA spectroscopy enables us to suppress the achiral background *before* the signal detection. Measurements less susceptible to the laser fluctuation are, therefore, realized in CARS-ROA spectroscopy. However, SNR of the spectra obtained in CARS-ROA spectroscopy was so far not satisfactory in comparison with the conventional ROA spectroscopy due to weak signal.

The weak signal intensity in our previous setups is partly due to near-infrared (NIR) excitation; we employed 1064-nm and supercontinuum (SC) ranging from 1.1 μm to 1.6μm light source for ω_1 and ω_2, respectively. Although NIR excitation has several merits such as low photodamage to sample

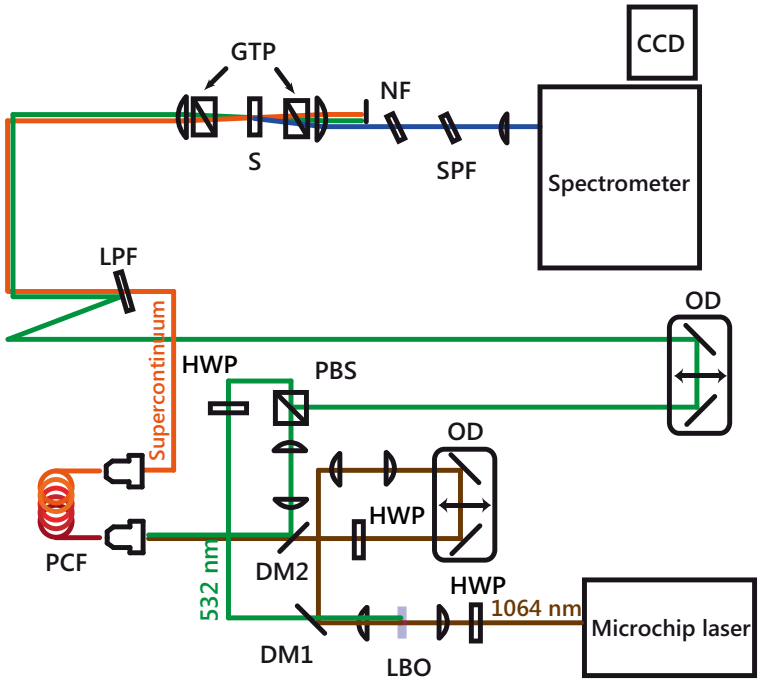

Figure 7.1: Schematic diagram of the visible excited CARS-ROA spectrometer. HWP: Half wave plate, DM1: Short-pass dichroic mirror (Thorlabs, DMSP805), DM2: Long-pass dichroic mirror (Thorlabs, DMLP900), PBS: Polarized beam splitter (Thorlabs, PBS201), PCF: Custom-made photonic crystal fiber, OD: Optical Delay, LPF: Long-pass filter (Semrock, BLP01-532R-25), GTP: Glan-Taylor prism (Thorlabs, GT5), S: Sample , NF: Notch filter (Semrock, NF03-532/1064E-25), SPF: Short-pass filter (Semrock, SP01-532RU-25).

and weak fluorescence interference [164, 165], it significantly sacrifices SNR because ROA signal is proportional to the fifth power of the incident frequency [97,164]. Herein, we have developed a CARS-ROA spectrometer with visible (532 nm) excitation and improved the SNR of ROA significantly.

7.2 Experimental

The schematic of our visible excited CARS-ROA spectrometer is shown in Fig. 7.1. A 25-kHz microchip laser (Hamamatsu, L11475), which provides 400 ps pulses at the wavelength of 1064 nm, is used as a light source. The output of the laser is frequency-doubled by a LBO crystal and the generated second harmonic is separated from the residual fundamental. The major part ($\sim$ 100 mW) of the 532-nm radiation is used as narrowband ω_1 and the other is used to excite a PCF. In this study, we employ the dual pumping scheme, in which PCF is pumped both with 532-nm and 1064-nm radiation [166, 167]. The spectra of SC generated by the PCF with different pumping schemes are shown in Fig. 7.2. The spectral profile of the SC pumped only by 532 nm is dominated by spiky peaks originating from stimulated Raman processes, which is unsuitable for multiplex CARS spectroscopy. When the PCF is excited both with 532 nm and 1064 nm, broad and intense SC, which covers almost all the fingerprint region, is generated in the current experimental condition. The optical configura-

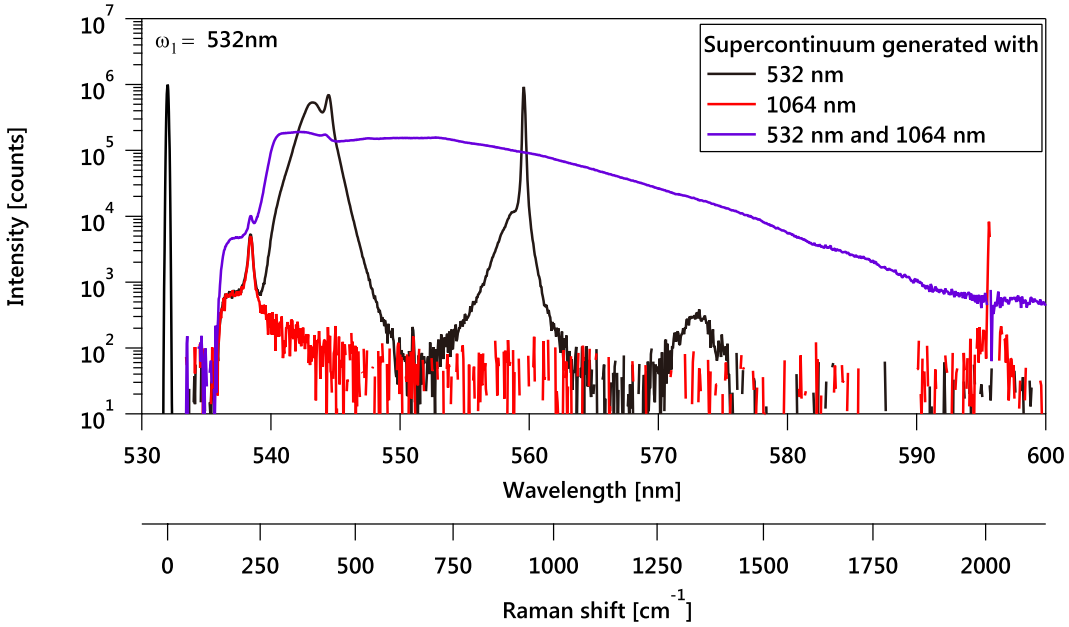

Figure 7.2: Spectra of the SC generated with the different pump schemes. These are measured as nonresonant CARS spectra of water.

tion around the sample is basically the same as what we previously reported in the NIR-CARS-ROA spectroscopy [158]. Incident ω_1 and ω_2 polarizations are set parallel to each other with a single Glan-Taylor polarizer. The polarization of the CARS field is selected by the second Glan-Taylor polarizer after the sample, which is slightly tilted from the perpendicular configuration (referred to as θ) so that the small portion of achiral CARS field passes through the polarizer and acts as a local oscillator. Spectra are obtained with a polychromator (Acton SP2300, Princeton Instruments) and a CCD camera(PIXIS 100BR eXcelon, Princeton Instruments). Simulation of CARS-ROA spectrum is performed by using density functional theory with Gaussian 03 [168]. The minimum energy structure was optimized with B3PW91 functional and aug-cc-pVDZ basis set and Raman/ROA properties were calculated with B3LYP functional and 6-31G** basis set. A scaling factor of 0.97 was applied for comparison with the observed spectra.

7.3 Method

The procedure for extracting CARS-ROA spectra is based on that previously reported [158]. We have measured CARS spectra at $\theta = \pm 0.5^\circ$ and CARS-ROA spectrum can be obtained as the difference spectrum between these. As we previously discussed [109], however, CARS-ROA spectra are distorted by optical rotatory dispersion (ORD) of the sample itself. With ORD (here denoted as α), CARS spectrum obtained at θ is written as

$$I(\theta) \propto |\sin(\theta - \alpha)\chi_{1111} + \cos(\theta - \alpha)\chi_{2111}|^2. \tag{7.1}$$

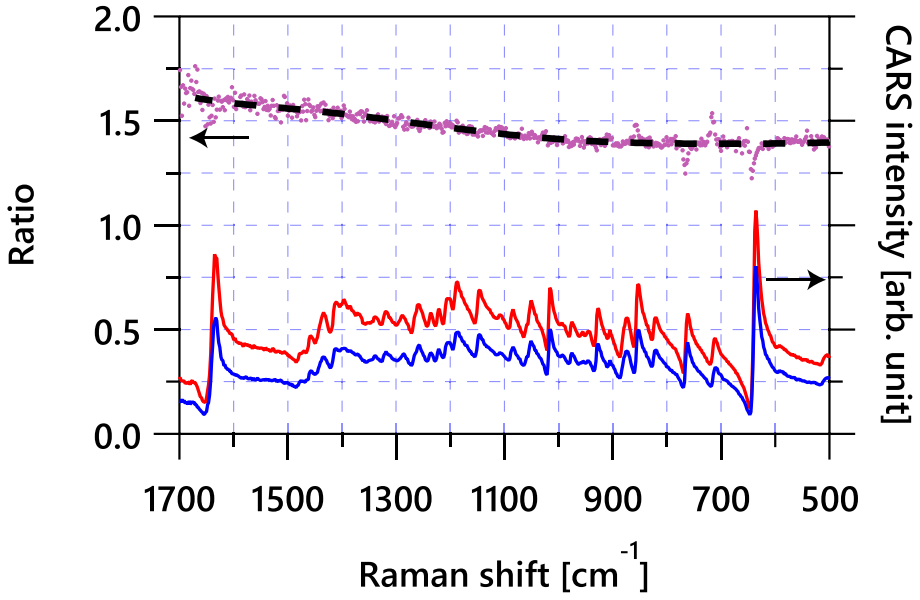

Figure 7.3: CARS spectra of (+)-β-pinene measured at $\theta = 0.5°$ (red curve) and $\theta = -0.5°$ (blue curve). Dots represent the ratio of these two CARS spectra $I(\theta)/I(-\theta)$ and dashed curve is from the spline fitting.

Thus, the calculated difference spectrum between $I(\theta)$ and $I(-\theta)$ becomes

$$I(\theta) - I(-\theta) \propto 2\theta\alpha|\chi_{1111}|^2 + 4\theta\mathrm{Re}[\chi^*_{1111}\chi_{2111}], \tag{7.2}$$

where $|\chi_{1111}|^2$ and $\mathrm{Re}[\chi^*_{1111}\chi_{2111}]$ correspond to CARS and ROA intensity, respectively. In Eq. (7.2), the term of $|\chi_{2111}|^2$ is neglected. The dispersive CARS spectrum is superposed on the calculated difference spectrum with the weight coefficient of $2\theta\alpha$. In order to remove this contribution, here we fit the $I(\theta)/I(-\theta)$ spectrum with a spline function (Fig. 7.3). The fitted spectrum can be approximated by $[(\theta-\alpha)/(\theta+\alpha)]^2$ because the sharp vibrational peaks do not significantly affect the result of the fitting procedure with a spline function. Then, ROA spectrum is extracted by calculating

$$\frac{\theta+\alpha}{\theta-\alpha}\left[I(\theta) - \left(\frac{\theta-\alpha}{\theta+\alpha}\right)^2 I(-\theta)\right] \propto \theta\mathrm{Re}[\chi^*_{1111}\chi_{2111}]. \tag{7.3}$$

7.4 Results and discussion

CARS and CARS-ROA spectra of β-pinene measured with the 532-nm setup developed in this work are shown in Fig. 7.4-(a,b,c). For comparison, CARS-ROA spectrum of (-)-β-pinene obtained with the previous 1064-nm setup is shown in Fig. 7.4-(d). In the NIR-CARS-ROA spectrum, which was measured with 1-hour exposure time, although several characteristic peaks between 600 cm^{-1} and 900 cm^{-1} were measured, weak ROA signals in the higher wavenumber region were severely buried

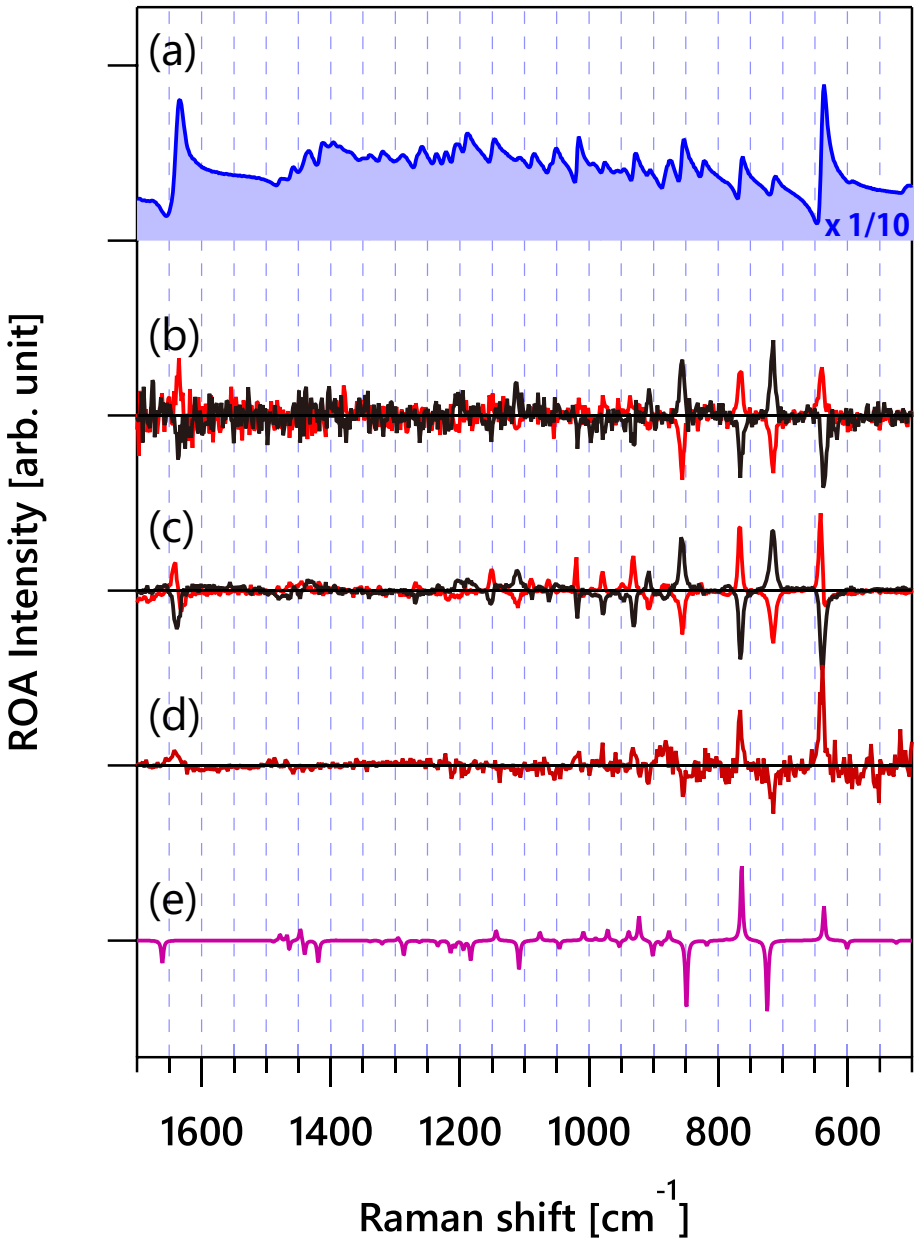

Figure 7.4: (a) CARS spectrum of $(-)$-β-pinene with 1 hour exposure time with the 532 nm setup developed in this research (reduced to 1/10 for comparison). (b) CARS-ROA spectra of $(+)$-β-pinene (black) and $(-)$-β-pinene (red) obtained the 532 nm setup. The exposure time was 1 minute, and the excitation power was 100 mW for ω_1 and 20 mW for ω_2. (c) CARS-ROA spectra of $(+)$ and $(-)$-β-pinene obtained with 1-hour exposure. Measurements conditions other than exposure time are the same as (b). (d) CARS-ROA spectrum of $(-)$-β-pinene obtained with the previous 1064 nm setup with the 1-hour exposure. The excitation power was 200 mW for ω_1 and 70 mW for ω_2. (e) Calculated CARS-ROA spectrum.

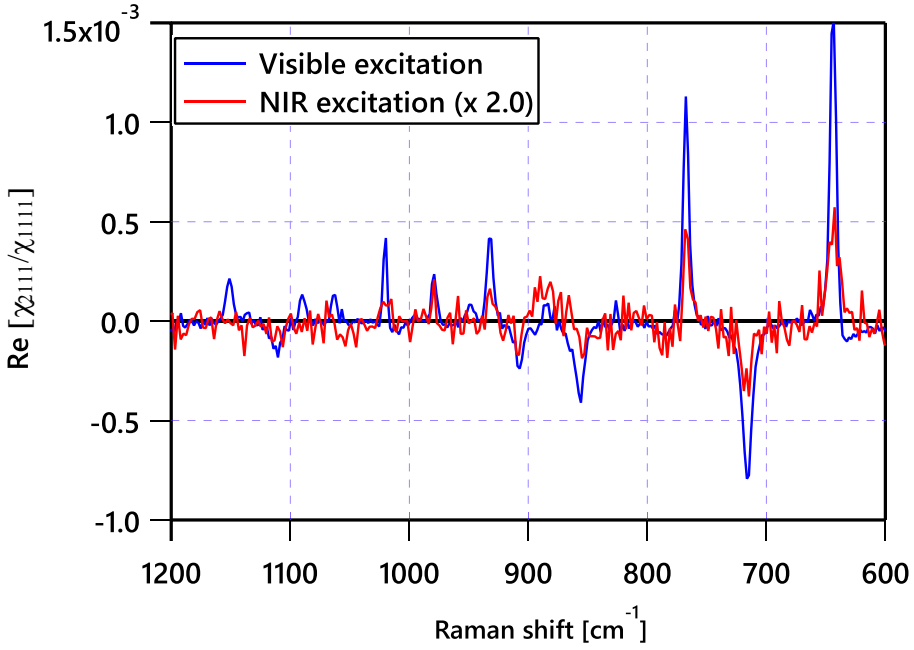

Figure 7.5: Comparison of the spectra of $\mathrm{Re}[\chi^*_{1111}\chi_{2111}]/|\chi_{1111}|^2$ calculated from the VIS- and NIR-CARS-ROA measurements.

in noises (Fig. 7.4-(d)). In the VIS-CARS-ROA spectroscopy, these characteristic peaks are clearly observed only by 1-minute exposure (Fig. 7.4-(b)). With 1-hour exposure time (Fig. 7.4-(c)), VIS-CARS-ROA spectrum was obtained with high SNR and almost all the peaks are in the mirror image of the enantiomer's spectrum. Nearly all the spectral features in the measured spectrum also show good consistency with those in the spectrum simulated with quantum chemical calculations.

Although it is difficult to quantitatively compare the VIS-CARS-ROA spectrum to the NIR-CARS-ROA spectrum because of the difference in the instrumental performance, the ratio $\mathrm{Re}[\chi^*_{1111}\chi_{2111}]/|\chi_{1111}|^2$ is independent of instrumental response and can be directly compared. This ratio is calculated as

$$\frac{\mathrm{Re}[\chi^*_{1111}\chi_{2111}]}{|\chi_{1111}|^2} = \frac{A\Gamma}{2\chi^{\mathrm{NR}}_{1111}} \frac{\Delta}{[(\Omega + A/\chi^{\mathrm{NR}}_{1111}) - \omega]^2 + \Gamma^2}, \tag{7.4}$$

where A, Ω, Γ, and Δ are the amplitude, frequency, damping constant and circular intensity difference of the Raman active mode, respectively, and ω is the Raman shift. Based on the previous measurements [109, 158], contribution of $\chi^{\mathrm{NR}}_{2111}$ is neglected in Eq. (7.4). Due to linear frequency dependence of Δ value [97], Eq. (7.4) should be proportional to the frequency of the scattered light. Thus, it is expected that the ratio is 1.8 - 2.0 times larger in the visible excitation than the NIR excitation.

These ratios for NIR- and VIS-CARS-ROA spectra are shown in Fig. 7.5. The ratio calculated for the visible excitation is even greater than two times of that for the NIR excitation, which is probably due to electronic pre-resonance. This enhancement, in addition to the reduction of the achiral background in CARS-ROA spectroscopy, makes measurements even easier.

7.5 Conclusion

A visible-excited CARS-ROA spectrometer was reported in this chapter. By employing the dual pumping scheme, we have generated broad and intense SC around 532 nm, which enables multiplex visible CARS-ROA spectroscopy. We have measured CARS-ROA spectra of (+)- and (-)-β-pinene with the visible excitation as a demonstration of the setup. The obtained spectra in VIS-CARS-ROA are well consistent with both the spectrum measured in the previously developed NIR-CARS-ROA setup and that simulated by quantum chemical calculation. In the visible excitation, SNR higher than that in the NIR excitation was realized mainly due to large scattering cross-section and optical activity tensor.

The contents of this chapter were published in Ref. [73].

Part IV

Summary

Chapter 8

Summary and prospects

8.1 Summary of this thesis

Despite its importance in the mechanistic study of biochemical reactions, the ultrafast chiroptical spectroscopy has been applied to just a few chemical species so far due to the experimental difficulty of measuring extremely weak chiroptical signals. The present study was motivated by the need for ultrafast chiroptical methods which are more sensitive and easier to apply to biochemical samples. The development of the new ultrafast electronic and vibrational chiroptical techniques and its application to the detection of the ultrafast chirality flip were reported in this thesis.

In Chapter 3, the development of the femtosecond TRCD spectroscopy using the polarization-resolved phase-sensitive method was reported. Proof-of-principle experiments were performed with Δ- and Λ-Ru(bpy)$_3^{2+}$ complexes. The results show that the sensitivity better than 0.4 mdeg with the broadband detection covering from 415 to 720 nm was accomplished in the developed spectrometer. The obtained sensitivity was about one order of magnitude better than the previous reported TRCD spectrometer designed for the single wavelength detection. The broadband detection was proven to be remarkably beneficial for TRCD spectroscopy because the artificial spectral component due to the photo-induced anisotropy can be separated from the genuine CD spectrum in combination with the singular value decomposition.

Application of the developed TRCD spectroscopy to biomolecular dynamics was demonstrated in Chapter 4. Transient absorption and TRCD spectra of the bilirubin-human serum albumin complex at pH=4.0 and 7.8 were measured. At pH=4.0, the different temporal behavior between the TA and TRCD of the complex indicating the chirality change in the excited state was observed. The experimental data were quantitatively analyzed by assuming the three-state model with the initial ground state, the excited state without the conformational change, and the excited state with the opposite handedness. To calculate the spectral shape of the excited-state species, the exciton coupling theory was extended to the transitions from the one-exciton states to the two-exciton state. The temporal change of the TA

and TRCD were well fitted by the solution of the differential equations of the model with the spectra calculated by the extended exciton coupling theory. The fitting analysis showed that the chirality flip undergoes with the time constant of 10.4 ± 0.5 ps. From the time-dependent population change of each state computed by the fitting analysis, the bleach-subtracted excited-state CD spectra were extracted, which clearly showed that the CD spectrum was inverted by the time evolution. At pH=7.8, on the other hand, the bleach-subtracted spectra did not show the sign reversal; no chirality reversal happened. It was demonstrated that photo-induced chirality change in the excited states could be directly probed by using the developed TRCD spectroscopy.

In Chapter 5, a novel method to measure ROA by coherent anti-Stokes Raman scattering (CARS-ROA) was demonstrated. In general, ROA spectroscopy is structurally more informative than electronic CD spectroscopy but measurement is more challenging due to the weaker signal. Coherent ROA spectroscopy has potential to open up not only the ultrafast time-resolved ROA spectroscopy but also wider applications of ROA such as ROA imaging or rapid ($\sim$ second) real-time tracking of conformational change of biomolecules. The basic idea of measurement is the same as what was employed in the TRCD spectrometer presented above; the incident pump and Stokes radiation is linearly polarized parallel to each other, and the CARS radiation perpendicular to the incident polarization is phase-sensitively detected by the optical heterodyne detection. With (-)-β-pinene as a sample, a ROA spectrum was obtained by CARS and consistent with the previously reported ROA spectrum obtained by the spontaneous Raman scattering. The contrast ratio of the chirality induced signal to the achiral background was improved by two orders of magnitude as compared to the conventional spontaneous ROA spectroscopy.

Another method for characterizing the phase of CARS-ROA field by using the active heterodyne detection was demonstrated in Chapter 6. The local oscillator was introduced externally with certain temporal delay. The spectral fringe originating to the interference between the CARS-ROA field and the LO is analyzed by the spectral interferometry. Although the signal to noise ratio was not better than that by the methods reported in Chapters 5 and 7, it was shown that the active heterodyne method was efficient for eliminating the artificial signal coming from the ORD of the sample. It is expected the active-heterodyne-detected CARS-ROA is advantageous when the fluorescent sample is measured because the spectral interferometry can almost perfectly remove the background signal such as fluorescence and room light.

With the aim of better signal to noise ratio, the extension of CARS-ROA spectroscopy from the near-infrared (1064 nm) to the visible (532 nm) spectral region was reported in Chapter 7. For multiplex CARS detection in the visible range, broad and intense supercontinuum was generated by pumping the photonic crystal fiber both with 532 and 1064 nm. As demonstrated in the actual experiment, the signal to noise ratio of the VIS-CARS-ROA spectra obtained with 1-min exposure was even better than that of the NIR-CARS-ROA spectra obtained with 1-hour exposure. Such improvement was

attributable to the ν^5 dependence of ROA signal intensity, and weak resonance with the electronic absorption in the deep-UV region.

8.2 Prospects

8.2.1 Possible improvements in performance of the ultrafast CD spectroscopy

The performance of TRCD spectroscopy is mainly characterized by time resolution, sensitivity, spectral range, and freeness from the anisotropic artifacts.

The time resolution achieved in the current study is 100 - 300 fs, which is fast enough for measuring dynamics such as electronic relaxation, proton transfer, protein internal motion, and photochemical isomerization [59]. For directly probing faster dynamics such as vibrational motion, photodissociation, photoionization, and electronic dephasing, a better temporal resolution is required. In the developed TRCD spectrometer, time resolution is determined by the cross-correlation between the pump and probe. A chirp-compensated output of a noncollinear optical parametric amplifier (NOPA) as short as 6.5 fs was reported to be used in solution-phase ultrafast spectroscopy [169]. So by combining the chirp compensating technique with the TRCD spectrometer, it will be possible to track even faster chirality change. In the gas phase spectroscopy, attempts to develop faster chiroptical methods have been made [170, 171]. However, currently these are in the stage of developing elemental techniques and no time-resolved measurement has been reported to the best of my knowledge.

Sub-millidegree sensitivity was realized in the current setup. In optical spectroscopic measurements, the sample concentration is usually adjusted so that the optical density becomes about 1. If the concentration is too high, no light can pass through the sample; if it is too low, no signal is observed. In such cases, a magnitude of ground-state CD is typically 10^{-3} o.d. in the absorbance unit and 33 mdeg in the ellipticity unit. Thus, the sub-millidegree sensitivity is enough for many applications because the ΔCD value as much as about 3 mdeg is expected when 10% of molecules is excited, which is typical condition employed in the time-resolved spectroscopy. For special applications such as ultrafast detection of enantiomeric excess generated by circularly polarized pump pulse, as will be described in the next section, much higher sensitivity is required. In the current measurement condition, the noise level is determined by the shot noise of the local oscillator, where the signal to noise ratio is proportional to the total input energy of probe light ($\propto \sqrt{\mathrm{time} \times \mathrm{power}}$). The most straightforward way to improve the sensitivity is thus to increase the power of the probe light. This can be realized by increasing either the energy of each pulse or the repetition rate. To make the pulse energy higher, one can use an output of NOPA for the probe, which provides the pulse energy one or two orders of magnitudes higher than the currently used continuum by the self-phase modulation but the spectral range becomes narrower. We can increase the repetition rate by using recently released high-repetition-rate femtosecond lasers such as Pharos (Light Conversion Ltd.) up to 1 MHz. With 1-MHz repetition rate, the sensitivity

becomes about 31 times better than that of the current 1-kHz system.

Extension of the spectral range down to the ultraviolet region is one of the most demanded improvements of the TRCD spectroscopy. Especially for application to proteins, an extension to the deep-UV region is needed because strong and characteristic CD spectrum, which is correlated with their secondary structures, is observed in the deep-UV range. Thus, deep-UV TRCD spectroscopy will be able to directly probe changes in the secondary structure of proteins induced by optical absorption [173] or temperature jump [174]. Measurement wavelength range is currently determined by the spectral width of the white-light continuum generated by the self-phase modulation of water, which spans down to about 400 nm. Using calcium fluoride for the medium of the self-phase modulation, it will be possible to obtain the continuum down to about 320 nm [172]. Generation of a broadband pulse in the deep-UV range is, however, still technically challenging. Ultrashort pulse down to about 275 nm can be generated by achromatic frequency doubling [175] or self-phase modulation [176] but convenient and stable generation of continuum below 250 nm has not been reported to the best of my knowledge. Technical advancement in deep-UV continuum generation is needed for the extension of the spectral range of TRCD spectroscopy.

For the rejection of the anisotropic artifact, currently post-processing such as the singular value decomposition is employed. However, the best solution is, of course, doing measurement under the condition where anisotropy is not induced by the pump radiation. Such a condition is, in principle, realized by employing circularly polarized light as the pump light. However, due to the spectral broadness of femtosecond pulses, retardation by the quarter wave plate is not constant for each spectral component of the pump light. It is a nontrivial question whether one can generate polarization state where the anisotropic artifact is smaller than the currently used linearly polarized excitation by using imperfect quarter wave plate. It will be needed to carefully design the optical arrangement of polarizers and waveplates to reduce the anisotropic artifacts as much as possible.

8.2.2 Future applications of the ultrafast CD spectroscopy

Biomolecules

In the electronic CD spectroscopy of proteins, measurement wavelength range is conveniently divided into three: the deep-UV range below 250 nm, the UV range from 250 to 300 nm, and the wavelength region above 300 nm. CD spectra in the wavelength range below 250 nm are dominated mainly by the $n - \pi^*$ transitions of amides and sensitive to the secondary structure. In the deep-UV range between 250 and 300 nm, CD bands of the $\pi - \pi^*$ transitions of aromatic side chains are observed, which are sensitive to the tertiary structure. When proteins have chromophores such as heme and flavin, they show CD peaks which induced by asymmetric interaction between the chromophore and surrounding amino acid residues. TRCD spectroscopy is currently experimentally practical for the wavelength

range above 400 nm and will be extendable down to about 320 nm using white-light continuum from calcium fluoride. In the foreseeable future, therefore, application to proteins with chromophores will be important. Heme proteins such as myoglobin and hemoglobin have been investigated by ultrafast spectroscopy [177–181]. Especially the detachment process of carbon monoxide bound to heme has attracted much attention [102, 179, 182]. The peak position of CD spectra of myoglobin and hemoglobin observed in the range between 400 and 450 nm changes when the carbon monoxide is attached the heme [183]. It is expected that detailed structural change of heme-induced by the CO dissociation like the doming motion [184] can be elucidated by broadband TRCD spectroscopy. Another interesting example is light-sensitive receptor proteins such as rhodopsin [185] and photoactive yellow protein [186], whose structural change is triggered by photoisomerization of the chromophore. It is expected that the isomerization undergoes in an unidirectional sense when the chromophores are surrounded by proteins. TRCD spectroscopy is a promising tool for probing the direction of the isomerization, which is difficult to distinguish in the conventional ultrafast spectroscopy.

Molecular machines

Molecular machines such as rotors [146, 187], tweezers [188], shuttles [189], and pinchers [190] have recently been synthesized as parts of molecular devices. Among them, the unidirectional rotary motion is important for continuous movement of devices as seen in biological systems [191]. In recently synthesized molecular motors [145, 146], unidirectional rotation can be induced by successive light irradiation and thermal relaxation. TRCD will be able to capture the structure of transition states during the rotation. Understanding of structural evolution during the rotation will be a guiding principle for improving the performance of the rotor and for using it as a part of a molecular device. Also in molecular machines with achiral motions, chiral moieties are often used in molecular machines. One typical example is rotaxane used in molecular shuttles [189]. In such machines, cyclodextrin including azobenzene moves back and forth like a shuttle. Azobenzene shows induced CD signal when it is included by cyclodextrins and its sign varies by the relative position of the cyclodextrin moiety [192, 193]. Thus, the time-dependent change of induced CD of azobenzene, which should by synchronized with the position of cyclodextrin, can directly probe the nanoscale shuttle movement.

CD measurement of short-lived chiral species

Ultrafast TRCD spectroscopy will be also useful for obtaining CD spectrum of achiral species. Here, I used the term achiral for denoting achiral as a time-averaged structure. Because no molecule is still, any molecule can be chiral if one takes a snapshot of it. This is schematically described in Fig. 8.1. Even for achiral molecules, each molecule can have non-zero CD spectrum at each moment as shown in Fig. 8.1 (a), but it becomes zero if the spectra are averaged over ensemble as seen in Fig. 8.1 (b). Thus, in the steady-state CD spectroscopy, it is impossible to obtain CD spectrum of achiral molecule

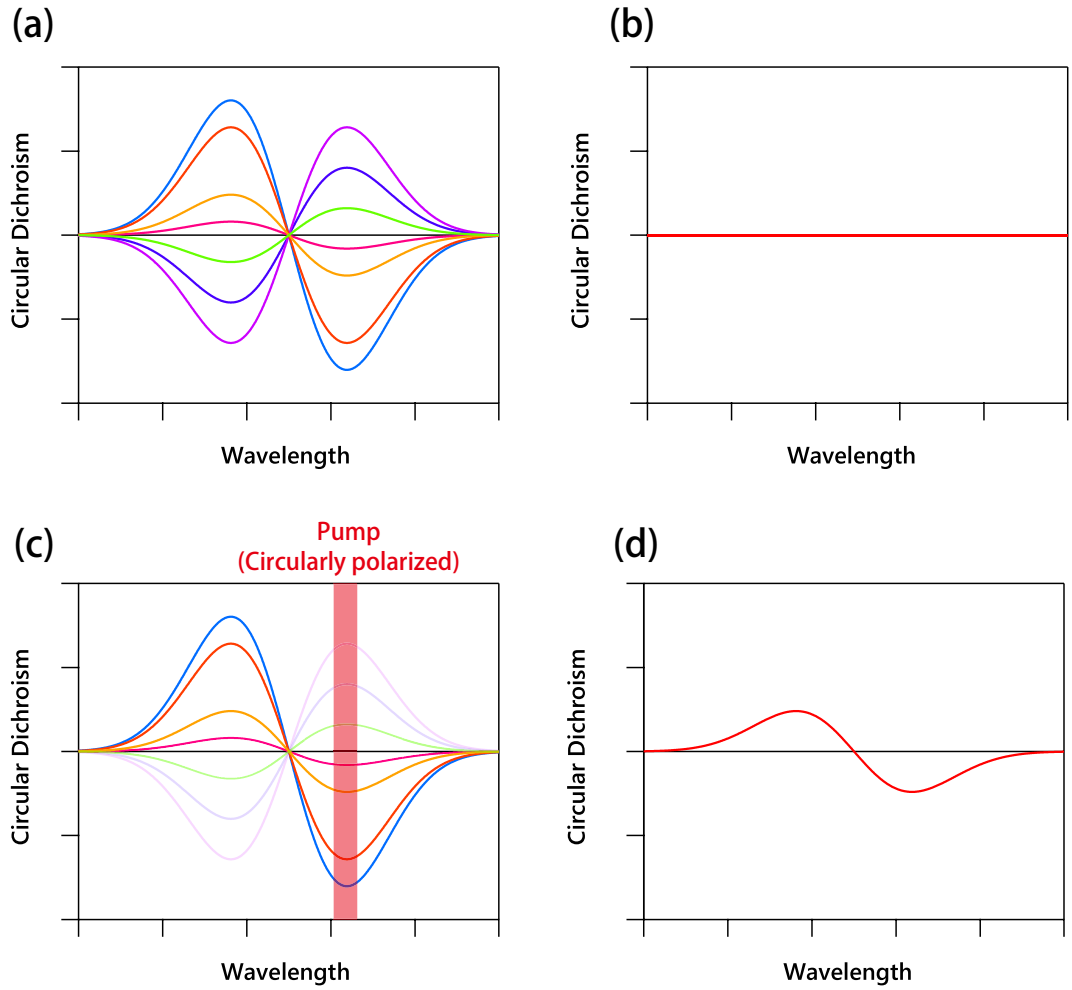

Figure 8.1: (a) Schematic CD spectra of each molecule of achiral solution. (b) Experimentally observable ensemble-averaged CD spectrum of achiral solution. (c) Schematic CD spectra of each achiral molecule after photoexcitation with circularly polarized pump radiation. (d) Ensemble-averaged CD spectrum of achiral solution after the photoexcitation.

even though CD spectra of individual molecules provide plentiful molecular structural information such as the dihedral angle between two chromophores. CD spectroscopy of achiral molecules is, however, possible using TRCD spectroscopy. If the ensemble is excited by the circularly polarized pump radiation (Fig. 8.1 (c)), non-zero enantiomeric excess is artificially generated to show non-zero ensemble averaged CD as seen in Fig. 8.1 (d). The observed CD spectrum should correspond to one enantiomeric form of molecule, which is achiral after time- or ensemble-averaging. By measuring the temporal evolution of the TRCD spectra after the excitation, it will also be possible to track the racemization process.

8.2.3 Possible improvements in performance of the CARS-ROA spectroscopy

The first and most serious problem in ROA spectroscopy is that extremely long exposure is needed. With a commercially available ROA spectrometer from BioTools, several hours to several days ex-

posure with sub-watt to several-watts incident laser power is required to take a ROA spectrum of a protein solution (see [194] for example). In the spontaneous ROA spectroscopy, signal to noise ratio is proportional to the square root of the total input laser energy. Maximum power usable in experiments is limited by damage threshold of samples, which is usually several watts at most. Thus, it is probably difficult to dramatically improve the signal to noise ratio in the spontaneous ROA spectroscopy in the future. In the coherent ROA spectroscopy, on the other hand, the signal intensity can be higher by employing input pulses with higher peak power with keeping the average power. As the absolute intensity of CARS signal is determined by various experimental conditions such as concentration, optical path length, confocal parameter, dispersion of refractive index, and the angle between the two incident beams, it is difficult to directly compare the signal to noise ratio of the spontaneous ROA and coherent ROA. However, in typical experimental condition for concentrated bulk solution, the signal to noise ratio at the quantum limit becomes higher in coherent Raman scattering [78]. Thus, it is expected that better signal to noise ratio is also obtained in coherent ROA spectroscopy.

In the context of developments of rapid bio-imaging tools, a variety of CARS spectrometers have been reported recently [195–200]. These are broadly grouped into two categories: frequency-domain measurement [195, 198, 200] and time-domain measurements [196, 199]. In the both methods, two or three input pulses, corresponding to the pump, Stokes, and probe, are employed. These techniques can readily be extended to CARS-ROA by setting the incident polarization parallel to each other and detecting both the phase and amplitude the CARS field perpendicular the incident polarization.

In the current study, I have demonstrated CARS-ROA spectroscopy as the first example of ROA spectroscopy by coherent Raman scattering. Besides CARS, several coherent Raman processes such as stimulated Raman scattering (SRS) and Raman-induced Kerr effect (RIKE) are widely used for bio-imaging [201–203] and ultrafast measurements [204–206]. It is also possible to make them chiroptical by a scheme similar to CARS-ROA [80]. One important advantage of SRS and RIKE over CARS in ROA measurement is that the counter-propagating configuration, where the two incident beams counter-propagate, is allowed in SRS and RIKE because the phase matching condition is automatically fulfilled in these processes. In such a condition, backward-scattered ROA spectrum [97] can also be obtained in the coherent ROA spectroscopy; only the forward-scattered ROA spectrum can be obtained in the CARS-ROA spectroscopy.

8.2.4 Future applications of CARS-ROA spectroscopy

I believe sub-nanosecond CARS-ROA system developed in the present study can be applied to nanosecond time-resolved measurement with slight modifications. To realize time-resolved measurements, it is needed to introduce the pump pulses synchronized with the probe pulses with a certain delay. In nanosecond time-resolved spectroscopy, two electronically triggered laser sources are usually used for the pump and probe. However, the currently used passively Q-switched microchip laser cannot be

triggered externally. Therefore, it needs to be replaced by an actively Q-switched laser in addition to installing a pump laser that can also be externally triggered.

As an application, relatively slow dynamics of proteins occurring on the nanosecond to millisecond time scale will be able to be investigated in great detail by time-resolved ROA spectroscopy. For one, protein folding, a process that a protein achieves its native structure, has attracted great attention as a "missing link" between a gene sequence and protein functionality [207]. A variety of spectroscopic methods such as fluorescence, CD, X-ray scattering, absorption, IR, and NMR have been used for tracking dynamic change toward the natively folded structure [207]. Also computational studies have greatly contributed to the mechanistic understanding of protein folding [208]. Although lots of theories have been proposed so far, no consensus has been reached probably due to the difficulty to compare proposed theories with experimental data [209]. ROA spectroscopy provides more structural parameters than the above spectroscopic techniques with time resolution fast enough for tracking any protein dynamics. Time-resolved ROA spectroscopy will be a promising tool for advancing the research on protein folding.

Bibliography

[1] Y. Nambu and G. Jona-Lasinio, Dynamical Model of Elementary Particles Based on an Analogy with Superconductivity. I, *Phys. Rev.*, **122**, 345–358 (1961).

[2] P. Cintas, Chirality of living systems: a helping hand from crystals and oligopeptides., *Angew. Chem. Int. Ed. Engl.*, **41**, 1139–45 (2002).

[3] D. F. Arago, Sur une modification remarquable qu'éprouvent les rayons lumineux dans leur passage à travers certains corps diaphanes et sur quelques autres nouveaux phénomènes d'optique, *Mem. L'Inst.*, **12**, 93 (1811).

[4] J. B. Biot, Phénomènes de polarisation successive, observés dans des fluides homogènes., *Bull. Soc. Philomath.*, page 190 (1815).

[5] U. Weiss, H. Ziffer, and E. Charney, Optical activity of non-planar conjugated dienes-I, *Tetrahedron*, **21**, 3105–3120 (1965).

[6] E. Charney, H. Ziffer, and U. Weiss, Optical activity of non-planar conjugated dienes-II, *Tetrahedron*, **21**, 3121–3126 (1965).

[7] H. E. Smith, Chiroptical Properties of the Benzene Chromophore. A Method for the Determination of the Absolute Configurations of Benzene Compounds by Application of the Benzene Sector and Benzene Chirality Rules, *Chem. Rev.*, **98**, 1709–1740 (1998).

[8] S. Mason, R. Seal, and D. Roberts, Optical activity in the biaryl series, *Tetrahedron*, **30**, 1671–1682 (1974).

[9] T. Nakano and Y. Okamoto, Synthetic helical polymers: Conformation and function, *Chem. Rev.*, **101**, 4013–4038 (2001).

[10] Bodie E . Douglas and Yoshihiko Saito. *Stereochemistry of Optically Active Transition Metal Compounds*, volume 119 of *ACS Symposium Series*. AMERICAN CHEMICAL SOCIETY, WASHINGTON, D. C., (1980).

[11] L. I. Katzin and E. Gulyas, Absorption, rotatory dispersion, and circular dichroism studies on some hydroxy and amino acids, *J. Am. Chem. Soc.*, **90**, 247–251 (1968).

[12] G. Holzwarth and P. Doty, The Ultraviolet Circular Dichroism of Polypeptides 1, *J. Am. Chem. Soc.*, **87**, 218–228 (1965).

[13] Y.-H. Chen, J. T. Yang, and K. H. Chau, Determination of the helix and β form of proteins in aqueous solution by circular dichroism, *Biochemistry*, **13**, 3350–3359 (1974).

[14] S. W. Provencher and J. Gloeckner, Estimation of globular protein secondary structure from circular dichroism, *Biochemistry*, **20**, 33–37 (1981).

[15] Y.-H. Chen, J. T. Yang, and H. M. Martinez, Determination of the secondary structures of proteins by circular dichroism and optical rotatory dispersion, *Biochemistry*, **11**, 4120–4131 (1972).

[16] S. M. Kelly, T. J. Jess, and N. C. Price, How to study proteins by circular dichroism., *Biochim. Biophys. Acta*, **1751**, 119–39 (2005).

[17] C. A. Sprecher and W. C. Johnson, Circular dichroism of the nucleic acid monomers., *Biopolymers*, **16**, 2243–64 (1977).

[18] G. C. Causley and W. C. Johnson, Polynucleotide conformation from flow dichroism studies., *Biopolymers*, **21**, 1763–80 (1982).

[19] L. Rosenfeld, Quantenmechanische Theorie der naturlichen optischen Aktivitat von Flussigkeiten und Gasen, *Z. Phys.*, **52**, 161–174 (1929).

[20] W. Moffitt, R. B. Woodward, A. Moscowitz, W. Klyne, and C. Djerassi, Structure and the Optical Rotatory Dispersion of Saturated Ketones, *J. Am. Chem. Soc.*, **83**, 4013–4018 (1961).

[21] N. Harada and K. Nakanishi, Determining the chiralities of optically active glycols, *J. Am. Chem. Soc.*, **91**, 3989–3991 (1969).

[22] N. J. Greenfield and G. D. Fasman, Computed circular dichroism spectra for the evaluation of protein conformation, *Biochemistry*, **8**, 4108–4116 (1969).

[23] F. S. Richardson and J. P. Riehl, Circularly polarized luminescence spectroscopy, *Chem. Rev.*, **77**, 773–792 (1977).

[24] I. Z. Steinberg, Circular polarization of luminescence: biochemical and biophysical applications., *Annu. Rev. Biophys. Bioeng.*, **7**, 113–37 (1978).

[25] C. D. Tran and G. S. Beddard, Excited state properties of bilirubin and its photoproducts using picosecond flourescence and ciruclarly polarized luminescence spectroscopy, *Biochim. Biophys. Acta - Gen. Subj.*, **678**, 497–504 (1981).

[26] T. Freedman, X. Cao, R. Dukor, and L. Nafie, Absolute configuration determination of chiral molecules in the solution state using vibrational circular dichroism, *Chirality*, **758**, 743–758 (2003).

[27] J. Haesler, I. Schindelholz, E. Riguet, C. G. Bochet, and W. Hug, Absolute configuration of chirally deuterated neopentane., *Nature*, **446**, 526–9 (2007).

[28] J. Costante, L. Hecht, P. Polavarapu, A. Collet, and L. Barron, Absolute configuration of bromochlorofluoromethane from experimental and ab initio theoretical vibrational Raman optical activity, *Angew. Chem. Int. Ed.*, **36**, 885–887 (1997).

[29] K. M. Spencer, S. J. Cianciosi, J. E. Baldwin, T. B. Freedman, and L. A. Nafie, Determination of Enantiomeric Excess in Deuterated Chiral Hydrocarbons by Vibrational Circular Dichroism Spectroscopy, *Appl. Spectrosc.*, **44**, 235–238 (1990).

[30] L. Hecht, A. L. Phillips, and L. D. Barron, Determination of enantiomeric excess using Raman optical activity, *J. Raman Spectrosc.*, **26**, 727–732 (1995).

[31] C. Guo, R. D. Shah, R. K. Dukor, X. Cao, T. B. Freedman, and L. A. Nafie, Determination of enantiomeric excess in samples of chiral molecules using fourier transform vibrational circular dichroism spectroscopy: simulation of real-time reaction monitoring., *Anal. Chem.*, **76**, 6956–66 (2004).

[32] M. Diem, P. J. Gotkin, J. M. Kupfer, A. G. Tindall, and L. A. Nafie, Vibrational circular dichroism in amino acids and peptides. 1. Alanine, *J. Am. Chem. Soc.*, **99**, 8103–8104 (1977).

[33] M. Diem, P. L. Polavarapu, M. Oboodi, and L. A. Nafie, Vibrational circular dichroism in amino acids and peptides. 4. Vibrational analysis, assignments, and solution-phase Raman spectra of deuterated isotopomers of alanine, *J. Am. Chem. Soc.*, **104**, 3329–3336 (1982).

[34] M. Diem, P. J. Gotkin, J. M. Kupfer, and L. A. Nafie, Vibrational circular dichroism in amino acids and peptides. 2. Simple alanyl peptides, *J. Am. Chem. Soc.*, **100**, 5644–5650 (1978).

[35] B. B. Lal and L. A. Nafie, Vibrational circular dichroism in amino acids and peptides. 7. Amide stretching vibrations in polypeptides., *Biopolymers*, **21**, 2161–83 (1982).

[36] T. Keiderling, Vibrational CD of biopolymers, *Nature*, **322**, 851 (1986).

[37] P. Xie, Q. Zhou, and M. Diem, Conformational studies of β-turns in cyclic peptides by vibrational circular dichroism., *J. Am. Chem. Soc.*, **117**, 9502–9508 (1995).

[38] P. Pancoska, S. C. Yasui, and T. A. Keiderling, Enhanced sensitivity to conformation in various proteins. Vibrational circular dichroism results, *Biochemistry*, **28**, 5917–5923 (1989).

[39] V. Baumruk and T. A. Keiderling, Vibrational circular dichroism of proteins in water solution, *J. Am. Chem. Soc.*, **115**, 6939–6942 (1993).

[40] T. J. Measey and R. Schweitzer-Stenner, Vibrational circular dichroism as a probe of fibrillogenesis: the origin of the anomalous intensity enhancement of amyloid-like fibrils., *J. Am. Chem. Soc.*, **133**, 1066–76 (2011).

[41] D. Kurouski, R. a. Lombardi, R. K. Dukor, I. K. Lednev, and L. a. Nafie, Direct observation and pH control of reversed supramolecular chirality in insulin fibrils by vibrational circular dichroism., *Chem. Commun.*, **46**, 7154–6 (2010).

[42] A. R. Gargaro, L. D. Barron, and L. Hecht, Vibrational Raman optical activity of simple amino acids, *J. Raman Spectrosc.*, **24**, 91–96 (1993).

[43] I. H. McColl, E. W. Blanch, A. C. Gill, A. G. O. Rhie, M. A. Ritchie, L. Hecht, K. Nielsen, and L. D. Barron, A New Perspective on β-Sheet Structures Using Vibrational Raman Optical Activity: From Poly(L-lysine) to the Prion Protein., *J. Am. Chem. Soc.*, **125**, 10019–26 (2003).

[44] J. Kapitán, F. Zhu, L. Hecht, J. Gardiner, D. Seebach, and L. D. Barron, Solution Structures of β Peptides from Raman Optical Activity, *Angew. Chem. Int. Ed.*, **120**, 6492–6494 (2008).

[45] Z. Q. Wen, L. D. Barron, and L. Hecht, Vibrational Raman optical activity of monosaccharides, *J. Am. Chem. Soc.*, **115**, 285–292 (1993).

[46] A. F. Bell, L. Hecht, and L. D. Barron, Disaccharide Solution Stereochemistry from Vibrational Raman Optical Activity, *J. Am. Chem. Soc.*, **116**, 5155–5161 (1994).

[47] A. F. Bell, L. Hecht, and L. D. Barron, New Evidence for Conformational Flexibility in Cyclodextrins from Vibrational Raman Optical Activity, *Chem-Eur. J.*, **3**, 1292–1298 (1997).

[48] I. H. McColl, E. W. Blanch, L. Hecht, and L. D. Barron, A Study of α-Helix Hydration in Polypeptides, Proteins, and Viruses Using Vibrational Raman Optical Activity, *J. Am. Chem. Soc.*, **126**, 8181–8188 (2004).

[49] F. Zhu, N. Isaacs, L. Hecht, G. Tranter, and L. Barron, Raman optical activity of proteins, carbohydrates and glycoproteins, *Chirality*, **115**, 103–115 (2005).

[50] A. F. Bell, L. Hecht, and L. D. Barron, Vibrational Raman Optical Activity as a Probe of Polyribonucleotide Solution Stereochemistry, *J. Am. Chem. Soc.*, **119**, 6006–6013 (1997).

[51] A. F. Bell, L. Hecht, and L. D. Barron, Vibrational Raman optical activity of pyrimidine nucleosides, *J. Chem. Soc. Faraday. T.*, **93**, 553–562 (1997).

[52] A. F. Bell, L. Hecht, and L. D. Barron, Vibrational Raman Optical Activity of DNA and RNA, *J. Am. Chem. Soc.*, **120**, 5820–5821 (1998).

[53] L. D. Barron, L. Hecht, I. H. McColl, and E. W. Blanch, Raman optical activity comes of age, *Mol. Phys.*, **102**, 731–744 (2004).

[54] E. W. Blanch, L. A. Morozova-Roche, D. A. Cochran, A. J. Doig, L. Hecht, and L. D. Barron, Is polyproline II helix the killer conformation? A Raman optical activity study of the amyloidogenic prefibrillar intermediate of human lysozyme., *J. Mol. Biol.*, **301**, 553–63 (2000).

[55] V. N. Uversky, Natively unfolded proteins: a point where biology waits for physics., *Protein Sci.*, **11**, 739–56 (2002).

[56] H. Dyson and P. Wright, Intrinsically unstructured proteins and their functions, *Nat. Rev. Mol. Cell. Bio.*, **6**, 197–208 (2005).

[57] A. L. Schawlow and C. H. Townes, Infrared and Optical Masers, *Phys. Rev.*, **112**, 1940–1949 (1958).

[58] T. H. Maiman, Stimulated Optical Radiation in Ruby, *Nature*, **187**, 493–494 (1960).

[59] G. Fleming. *Chemical applications of ultrafast spectroscopy*. Oxford University Press,New York, NY, (1986).

[60] V. Sundström, Femtobiology., *Annu. Rev. Phys. Chem.*, **59**, 53–77 (2008).

[61] G. R. Fleming and M. Cho, CHROMOPHORE-SOLVENT DYNAMICS, *Annu. Rev. Phys. Chem.*, **47**, 109–134 (1996).

[62] E. T. J. Nibbering, H. Fidder, and E. Pines, Ultrafast chemistry: using time-resolved vibrational spectroscopy for interrogation of structural dynamics., *Annu. Rev. Phys. Chem.*, **56**, 337–67 (2005).

[63] H. Hamaguchi and T. L. Gustafson, Ultrafast Time-Resolved Spontaneous and Coherent Raman Spectroscopy: The Structure and Dynamics of Photogenerated Transient Species, *Ann. Rev. Phys. Chem.*, **45**, 593–622 (1994).

[64] J. Tenboer, S. Basu, N. Zatsepin, K. Pande, D. Milathianaki, M. Frank, M. Hunter, S. Boutet, G. J. Williams, J. E. Koglin, D. Oberthuer, M. Heymann, C. Kupitz, C. Conrad, J. Coe, S. Roy-Chowdhury, U. Weierstall, D. James, D. Wang, T. Grant, A. Barty, O. Yefanov, J. Scales, C. Gati, C. Seuring, V. Srajer, R. Henning, P. Schwander, R. Fromme, A. Ourmazd, K. Moffat, J. J. Van Thor, J. C. H. Spence, P. Fromme, H. N. Chapman, and M. Schmidt, Time-resolved serial crystallography captures high-resolution intermediates of photoactive yellow protein, *Science*, **346**, 1242–1246 (2014).

[65] F. A. Ferrone, The measurement of transient circular dichroism: A new kinetic technique, *Rev. Sci. Instrum.*, **45**, 1392 (1974).

[66] I. Tabushi, K. Yamamura, and T. Nishiya, Stopped-flow circular dichroism (SFCD) spectroscopy. Implication of significant conformational differences in the redox mechanism of cytochrome c, *J. Am. Chem. Soc.*, **101**, 2785–2787 (1979).

[67] J. W. Lewis, R. F. Tilton, C. M. Einterz, S. J. Milder, I. D. Kuntz, and D. S. Kliger, New technique for measuring circular dichroism changes on a nanosecond time scale. Application to (carbonmonoxy)myoglobin and (carbonmonoxy)hemoglobin, *J. Phys. Chem.*, **89**, 289–294 (1985).

[68] X. Xie and J. D. Simon, Picosecond time-resolved circular dichroism spectroscopy: experimental details and applications, *Rev. Sci. Instrum.*, **60**, 2614 (1989).

[69] J. W. Lewis, R. A. Goldbeck, D. S. Kliger, X. Xie, R. C. Dunn, and J. D. Simon, Time-resolved circular dichroism spectroscopy: experiment, theory, and applications to biological systems, *J. Phys. Chem.*, **96**, 5243–5254 (1992).

[70] C. Niezborala and F. Hache, Measuring the dynamics of circular dichroism in a pump-probe experiment with a Babinet-Soleil compensator, *J. Opt. Soc. Am. B*, **23**, 2418–2424 (2006).

[71] H. Rhee, Y.-G. June, J.-S. Lee, K.-K. Lee, J.-H. Ha, Z. H. Kim, S.-J. Jeon, and M. Cho, Femtosecond characterization of vibrational optical activity of chiral molecules., *Nature*, **458**, 310–3 (2009).

[72] I. Eom, S. Ahn, H. Rhee, and M. Cho, Single-Shot Electronic Optical Activity Interferometry: Power and Phase Fluctuation-Free Measurement, *Phys. Rev. Lett*, **108**, 103901 (2012).

[73] K. Hiramatsu, P. Leproux, V. Couderc, T. Nagata, and H. Kano, Raman optical activity spectroscopy by visible-excited coherent anti-Stokes Raman scattering, *Opt. Lett.*, **40**, 4170 (2015).

[74] L. Mendonça, F. Hache, P. Changenet-Barret, P. Plaza, H. Chosrowjan, S. Taniguchi, and Y. Imamoto, Ultrafast Carbonyl Motion of the Photoactive Yellow Protein Chromophore Probed by Femtosecond Circular Dichroism., *J. Am. Chem. Soc.*, **135**, 14637–14643 (2013).

[75] M. Bonmarin and J. Helbing, A picosecond time-resolved vibrational circular dichroism spectrometer, *Opt. Lett.*, **33**, 2086 (2008).

[76] B. Dutta and J. Helbing, Optimized interferometric setup for chiral and achiral ultrafast IR spectroscopy, *Opt. Express*, **23**, 16449 (2015).

[77] C. Ruckebusch, S. Aloïse, L. Blanchet, J. P. Huvenne, and G. Buntinx, Reliable multivariate curve resolution of femtosecond transient absorption spectra, *Chemom. Intell. Lab. Syst.*, **91**, 17–27 (2008).

[78] M. D. Levenson and S. Kano. *Introduction to Nonlinear Laser Spectroscopy*. Academic Press, New York, (1987).

[79] J. O. Bjarnason, H. C. Andersen, and B. S. Hudson, Quantum theory of coherent Raman scattering by optically active isotropic materials, *J. Chem. Phys.*, **72**, 4132 (1980).

[80] J. L. Oudar, C. Minot, and B. A. Garetz, Polarization spectroscopy as a probe of Raman optical activity, *J. Chem. Phys.*, **76**, 2227 (1982).

[81] E. A. Power and S. Zienau, Coulomb Gauge in Non-Relativistic Quantum Electro-Dynamics and the Shape of Spectral Lines, *Philos. Trans. R. Soc. A Math. Phys. Eng. Sci.*, **251**, 427–454 (1959).

[82] D. Abramavicius and S. Mukamel, Coherent third-order spectroscopic probes of molecular chirality., *J. Chem. Phys.*, **122**, 134305 (2005).

[83] L. D. Barron. *Molecular Light Scattering and Optical Activity*. Cambridge University Press, Cambridge, (2004).

[84] R. C. JONES, A New Calculus for the Treatment of Optical Systems, *J. Opt. Soc. Am.*, **31**, 488 (1941).

[85] Y. Shen. *Principles of nonlinear optics*. Wiley-Interscience,New York, NY, USA, (1984).

[86] J. A. Giordmaine, Nonlinear Optical Properties of Liquids, *Phys. Rev.*, **138**, A1599–A1606 (1965).

[87] M. a. Belkin † and Y. R. Shen ‡, Non-linear optical spectroscopy as a novel probe for molecular chirality, *Int. Rev. Phys. Chem.*, **24**, 257–299 (2005).

[88] M. Belkin, S. Han, X. Wei, and Y. Shen, Sum-Frequency Generation in Chiral Liquids near Electronic Resonance, *Phys. Rev. Lett.*, **87**, 1–4 (2001).

[89] W. De Boeij, G. Lucassen, C. Otto, and J. Greve, Resonance polarization and phase-mismatched CARS of pheophytin b excited in the Qy band, *J. Raman Spectrosc.*, **24**, 383–396 (1993).

[90] M. Belkin, T. Kulakov, K. Ernst, L. Yan, and Y. Shen, Sum-frequency vibrational spectroscopy on chiral liquids: A novel technique to probe molecular chirality, *Phys. Rev. Lett.*, **85**, 4474–4477 (2000).

[91] L. Fu, J. Liu, and E. C. Y. Yan, Chiral sum frequency generation spectroscopy for characterizing protein secondary structures at interfaces., *J. Am. Chem. Soc.*, **133**, 8094–7 (2011).

[92] M. Okuno and T.-a. Ishibashi, Chirality Discriminated by Heterodyne-Detected Vibrational Sum Frequency Generation, *J. Phys. Chem. Lett.*, **5**, 2874–2878 (2014).

[93] M. Okuno and T.-a. Ishibashi, Heterodyne-Detected Achiral and Chiral Vibrational Sum Frequency Generation of Proteins at Air/Water Interface, *J. Phys. Chem. C*, **119**, 9947–9954 (2015).

[94] N. Ji, V. Ostroverkhov, M. Belkin, Y.-J. Shiu, and Y.-R. Shen, Toward chiral sum-frequency spectroscopy., *J. Am. Chem. Soc.*, **128**, 8845–8 (2006).

[95] M. Belkin and Y. Shen, Doubly Resonant IR-UV Sum-Frequency Vibrational Spectroscopy on Molecular Chirality, *Phys. Rev. Lett.*, **91**, 213907 (2003).

[96] M. Okuno and T.-a. Ishibashi, Sensitive and Quantitative Probe of Molecular Chirality with Heterodyne-Detected Doubly Resonant Sum Frequency Generation Spectroscopy, *Anal. Chem.*, **87**, 10103–10108 (2015).

[97] L. D. Barron. *Molecular Light Scattering and Optical Activity*. Cambridge University Press, (2004).

[98] J. S. Gold, S. J. Milder, J. W. Lewis, and D. S. Kliger, Transient circular dichroism of the luminescent state of Ru(bpy)32+, *J. Am. Chem. Soc.*, **107**, 8285–8286 (1985).

[99] J. Meyer-Ilse, D. Akimov, and B. Dietzek, Ultrafast circular dichroism study of the ring opening of 7-dehydrocholesterol, *J. Phys. Chem. Lett.*, **3**, 182–185 (2012).

[100] C. Niezborala and F. Hache, Conformational changes in photoexcited (R)-(+)-1,1'-bi-2-naphthol studied by time-resolved circular dichroism., *J. Am. Chem. Soc.*, **130**, 12783–6 (2008).

[101] X. Xie and J. D. Simon, Picosecond circular dichroism spectroscopy: a Jones matrix analysis, *J. Opt. Soc. Am. B*, **7**, 1673 (1990).

[102] T. Dartigalongue and F. Hache, Observation of sub-100ps conformational changes in photolyzed carbonmonoxy-myoglobin probed by time-resolved circular dichroism, *Chem. Phys. Lett.*, **415**, 313–316 (2005).

[103] A. Trifonov, I. Buchvarov, A. Lohr, F. Würthner, and T. Fiebig, Broadband femtosecond circular dichroism spectrometer with white-light polarization control., *Rev. Sci. Instrum.*, **81**, 043104 (2010).

[104] T. Dartigalongue and F. Hache, Precise alignment of a longitudinal Pockels cell for time-resolved circular dichroism experiments, *J. Opt. Soc. Am. B*, **20**, 1780 (2003).

[105] I. Eom, S.-H. Ahn, H. Rhee, and M. Cho, Broadband near UV to visible optical activity measurement using self-heterodyned method., *Opt. Express*, **19**, 10017–28 (2011).

[106] R. C. Jones, A New Calculus for the Treatment of Optical Systems VII Properties of the N-Matrices, *J. Opt. Soc. Am.*, **38**, 671 (1948).

[107] L. Lepetit, G. Chériaux, and M. Joffre, Linear techniques of phase measurement by femtosecond spectral interferometry for applications in spectroscopy, *J. Opt. Soc. Am. B*, **12**, 2467 (1995).

[108] V. Joshi and P. K. Ghosh, Spectral evidence of spontaneous racemic and pseudoracemic interactions between optically active poly(pyridyl) metal chelates adsorbed on smectite clays, *J. Am. Chem. Soc.*, **111**, 5604–5612 (1989).

[109] K. Hiramatsu, H. Kano, and T. Nagata, Raman optical activity by coherent anti-Stokes Raman scattering spectral interferometry, *Opt. Express*, **21**, 13515 (2013).

[110] F. Harris, On the use of windows for harmonic analysis with the discrete Fourier transform, *Proc. IEEE*, **66**, 51–83 (1978).

[111] G. Fleming, A. Knight, J. Morris, R. Robbins, and G. Robinson, Rotational diffusion of the mode-locking dye dodci and its photoisomer, *Chem. Phys. Lett.*, **49**, 1–7 (1977).

[112] D. Waldeck, A. J. C. Jr., D. B. McDonald, and G. R. Fleming, Picosecond pulse induced transient molecular birefringence and dichroism, *J. Chem. Phys.*, **74**, 3381 (1981).

[113] J. S. Toll, Causality and the Dispersion Relation: Logical Foundations, *Phys. Rev.*, **104**, 1760–1770 (1956).

[114] C. Houssier and H. G. Kuball, Electro-optical properties of nucleic acids and nucleoproteins. 3. Kramers-Kronig relationships in linear birefringence and dichroism. Application to a DNA-proflavine complex., *Biopolymers*, **10**, 2421–33 (1971).

[115] A. N. Tarnovsky, W. Gawelda, M. Johnson, C. Bressler, and M. Chergui, Photexcitation of aqueous ruthenium(II)-tris-(2,2'-bipyridine) with high-intensity femtosecond laser pulses., *J. Phys. Chem. B*, **110**, 26497–505 (2006).

[116] K. Kalyanasundaram, Photophysics, photochemistry and solar energy conversion with tris(bipyridyl)ruthenium(II) and its analogues, *Coord. Chem. Rev.*, **46**, 159–244 (1982).

[117] A. J. McCaffery, S. F. Mason, and B. J. Norman, Optical rotatory power of co-ordination compounds. Part XII. Spectroscopic and configurational assignments for the tris-bipyridyl and -phenanthroline complexes of the di- and tri-valent iron-group metal ions, *J. Chem. Soc. A Inorganic, Phys. Theor.*, page 1428 (1969).

[118] G. V. Buxton, C. L. Greenstock, W. P. Helman, A. B. Ross, and W. Tsang, Critical Review of rate constants for reactions of hydrated electronsChemical Kinetic Data Base for Combustion Chemistry. Part 3: Propane, *J. Phys. Chem. Ref. Data*, **17**, 513 (1988).

[119] M. Mizuno and T. Tahara, Picosecond Time-Resolved Resonance Raman Study of the Solvated Electron in Water, *J. Phys. Chem. A*, **107**, 2411–2421 (2003).

[120] L. Vítek and J. D. Ostrow, Bilirubin chemistry and metabolism; harmful and protective aspects., *Curr. Pharm. Des.*, **15**, 2869–2883 (2009).

[121] P. A. Zunszain, J. Ghuman, A. F. McDonagh, and S. Curry, Crystallographic analysis of human serum albumin complexed with 4Z,15E-bilirubin-IXalpha., *J. Mol. Biol.*, **381**, 394–406 (2008).

[122] Y. Z. Hsieh and M. D. Morris, Resonance Raman spectroscopic study of bilirubin hydrogen bonding in solutions and in the albumin complex, *J. Am. Chem. Soc.*, **110**, 62–67 (1988).

[123] G. Blauer, D. Harmatz, and a. Naparstek, Circular dichroism of bilirubin-human serum albumin complexes in aqueous solution, *FEBS Lett.*, **9**, 53–55 (1970).

[124] G. Blauer, D. Harmatz, and J. Snir, Optical properties of bilirubin-serum albumin complexes in aqueous solution, *Biochim. Biophys. Acta - Protein Struct.*, **278**, 68–88 (1972).

[125] G. Blauer and D. Harmatz, Optical properties of bilirubin-serum albumin complexes in aqueous solution, *Biochim. Biophys. Acta - Protein Struct.*, **278**, 89–100 (1972).

[126] G. H. Beaven, A. D'Albis, and W. B. Gratzer, The Interaction of Bilirubin with Human Serum Albumin, *Eur. J. Biochem.*, **33**, 500–509 (1973).

[127] G. Blauer and G. Wagnière, Conformation of bilirubin and biliverdin in their complexes with serum albumin., *J. Am. Chem. Soc.*, **97**, 1949–1954 (1975).

[128] D. Harmatz and G. Blauer, Optical properties of bilirubin-serum albumin complexes in aqueous solution. A comparison among albumins from different species, *Arch. Biochem. Biophys.*, **170**, 375–383 (1975).

[129] D. Harmatz and G. Blauer, Optical properties of bilirubin-serum albumin complexes in aqueous solution. A comparison among albumins from different species., *Arch. Biochem. Biophys.*, **170**, 375–83 (1975).

[130] J. R. Rodriguez and A. E. García, OPTICAL PROPERTIES OF BILIRUBIN-SERUM ALBUMIN COMPLEXES IN AQUEOUS SOLUTION, *Interdiscip. Sci. Comput. Life Sci.*, **3**, 272–282 (2011).

[131] D. A. Lighnter, W. M. Wijekoon, and M. H. Zhang, Understanding bilirubin conformation and binding. Circular dichroism of human serum albumin complexes with bilirubin and its esters., *J. Biol. Chem.*, **263**, 16669–16676 (1988).

[132] R. V. Person, B. R. Peterson, and D. A. Lightner, Bilirubin conformational analysis and circular dichroism, *J. Am. Chem. Soc.*, **116**, 42–59 (1994).

[133] F. Zsila, Circular dichroism spectroscopy is a sensitive tool for investigation of bilirubin-enzyme interactions., *Biomacromolecules*, **12**, 221–7 (2011).

[134] I. Goncharova, S. Orlov, and M. Urbanová, The location of the high- and low-affinity bilirubin-binding sites on serum albumin: ligand-competition analysis investigated by circular dichroism., *Biophys. Chem.*, **180-181**, 55–65 (2013).

[135] C. Tran and G. S. Beddard, Interactions between bilirubin and albumins using picosecond fluorescence and circularly polarized luminescence spectroscopy, *J. Am. Chem. Soc.*, **104**, 6741–6747 (1982).

[136] B. Zietz, A. N. Macpherson, and T. Gillbro, Resolution of ultrafast excited state kinetics of bilirubin in chloroform and bound to human serum albumin, *Phys. Chem. Chem. Phys.*, **6**, 4535 (2004).

[137] B. Zietz and T. Gillbro, Initial photochemistry of bilirubin probed by femtosecond spectroscopy., *J. Phys. Chem. B*, **111**, 11997–2003 (2007).

[138] B. I. Greene, A. A. Lamola, and C. V. Shank, Picosecond primary photoprocesses of bilirubin bound to human serum albumin., *Proc. Natl. Acad. Sci. U. S. A.*, **78**, 2008–12 (1981).

[139] C. D. Tran and A. F. Drake, Circularly polarised luminescence of bilirubin bound to human serum albumin, *Biochem. Biophys. Res. Commun.*, **101**, 76–82 (1981).

[140] N. Berova, P. L. Polavarapu, K. Nakanishi, and R. W. Woody. *Comprehensive Chiroptical Spectroscopy*. John Wiley and Sons, Inc.: New York, (2012).

[141] V. Y. Plavskii, V. a. Mostovnikov, G. R. Mostovnikova, and a. I. Tret'yakova, Spectral fluorescence and polarization characteristics of Z,Z-bilirubin IXα, *J. Appl. Spectrosc.*, **74**, 120–132 (2007).

[142] G. Cerullo and S. De Silvestri, Ultrafast optical parametric amplifiers, *Rev. Sci. Instrum.*, **74**, 1 (2003).

[143] R. F. Chen, Removal of Fatty Acids from Serum Albumin by Charcoal Treatment Removal of Fatty Acids by Charcoal Treatment from Serum Albumin, *J. Biol. Chem.*, **242**, 173–181 (1967).

[144] R. Schoenlein, L. Peteanu, R. Mathies, and C. Shank, The first step in vision: femtosecond isomerization of rhodopsin, *Science (80-.).*, **254**, 412–415 (1991).

[145] N. Koumura, R. W. Zijlstra, R. a. v. Delden, N. Harada, and B. L. Feringa, Light-driven monodirectional molecular rotor., *Nature*, **401**, 152–5 (1999).

[146] J. C. M. Kistemaker, P. Štacko, J. Visser, and B. L. Feringa, Unidirectional rotary motion in achiral molecular motors, *Nat. Chem.*, **7** (2015).

[147] L. Nafie. *Vibrational Optical Activity: Principles and Applications*. Wiley, New York, (2011).

[148] R. Silva, J. Kubelka, P. Bour, S. M. Decatur, and T. A. Keiderling, Site-specific conformational determination in thermal unfolding studies of helical peptides using vibrational circular dichroism with isotopic substitution, *Proc. Natl. Acad. Sci. U.S.A.*, **97**, 8318 (2000).

[149] H. N. Paulsen, K. M. Hilligse, J. Thøgersen, S. R. Keiding, and J. J. Larsen, Coherent anti-Stokes Raman scattering microscopy with a photonic crystal fiber based light source, *Opt. Lett.*, **28**, 1123 (2003).

[150] H. Kano and H. Hamaguchi, Ultrabroadband ($>$2500 cm^{-1}) multiplex coherent anti-Stokes Raman scattering microspectroscopy using a supercontinuum generated from a photonic crystal fiber, *Appl. Phys. Lett.*, **86**, 121113 (2005).

[151] M. Okuno, H. Kano, P. Leproux, V. Couderc, J. P. R. Day, M. Bonn, and H. Hamaguchi, Quantitative CARS molecular fingerprinting of single living cells with the use of the maximum entropy method., *Angew. Chem. Int. Ed.*, **49**, 6773–7 (2010).

[152] P. Leproux, V. Couderc, A. d. Angelis, M. Okuno, H. Kano, and H. Hamaguchi, New opportunities offered by compact sub-nanosecond supercontinuum sources in ultra-broadband multiplex CARS microspectroscopy, *J. Raman Spectrosc.*, **42**, 1871–1874 (2011).

[153] L. Hecht and L. D. Barron, Magic angle Raman optical activity:[beta]-pinene and nopinone, *Spectrochim. Acta, Part A*, **45**, 671–674 (1989).

[154] R. L. Sutherland. *Handbook of Nonlinear Optics*. Marcel Dekker, New York, (1996).

[155] L. D. Barron, L. Hecht, A. R. Gargaro, and W. Hug, Vibrational Raman optical activity in forward scattering: Trans-pinane and β-pinene, *J. Raman Spectrosc.*, **21**, 375–379 (1990).

[156] L. D. Barron and J. R. Escribano, Polarized raman optical activity of β-pinene: electric quadrupole contributions, *Chem. Phys. Lett.*, **126**, 461–464 (1986).

[157] N. Koroteev, BioCARS-a novel nonlinear optical technique to study vibrational spectra of chiral biological molecules in solution, *Biospectroscopy*, **1**, 341–350 (1995).

[158] K. Hiramatsu, M. Okuno, H. Kano, P. Leproux, V. Couderc, and H.-o. Hamaguchi, Observation of Raman Optical Activity by Heterodyne-Detected Polarization-Resolved Coherent Anti-Stokes Raman Scattering, *Phys. Rev. Lett.*, **109**, 083901 (2012).

[159] C. L. Evans, E. O. Potma, and X. S. Xie, Coherent anti-Stokes Raman scattering spectral interferometry: determination of the real and imaginary components of nonlinear susceptibility $\chi^{(3)}$ for vibrational microscopy., *Opt. Lett.*, **29**, 2923–5 (2004).

[160] E. O. Potma, C. L. Evans, and X. S. Xie, Heterodyne coherent anti-Stokes Raman scattering (CARS) imaging, *Opt. Lett.*, **31**, 241–3 (2006).

[161] I. V. Stiopkin, H. D. Jayathilake, A. N. Bordenyuk, and A. V. Benderskii, Heterodyne-Detected Vibrational Sum Frequency Generation Spectroscopy., *J. Am. Chem. Soc.*, **130**, 2271–5 (2008).

[162] S. Yamaguchi and T. Tahara, Heterodyne-detected electronic sum frequency generation: "up" versus "down" alignment of interfacial molecules., *J. Chem. Phys.*, **129**, 101102 (2008).

[163] W. Hug and G. Hangartner, A novel high-throughput Raman spectrometer for polarization difference measurements, *J. Raman Spectrosc.*, **30**, 841–852 (1999).

[164] L. A. Nafie, B. E. Brinson, X. Cao, D. A. Rice, O. M. Rahim, R. K. Dukor, and N. J. Halas, Near-infrared excited Raman optical activity., *Appl. Spectrosc.*, **61**, 1103–6 (2007).

[165] M. Unno, T. Kikukawa, M. Kumauchi, and N. Kamo, Exploring the active site structure of a photoreceptor protein by Raman optical activity., *J. Phys. Chem. B*, **117**, 1321–5 (2013).

[166] P.-A. Champert, V. Couderc, P. Leproux, S. Février, V. Tombelaine, L. Labonté, P. Roy, C. Froehly, and P. Nérin, White-light supercontinuum generation in normally dispersive optical fiber using original multi-wavelength pumping system., *Opt. Express*, **12**, 4366–4371 (2004).

[167] M. Okuno, H. Kano, P. Leproux, V. Couderc, and H.-o. Hamaguchi, Ultrabroadband (2000 cm^{-1}) multiplex coherent anti-Stokes Raman scattering spectroscopy using a subnanosecond supercontinuum light source., *Opt. Lett.*, **32**, 3050–3052 (2007).

[168] M. J. Frisch, G. W. Trucks, H. B. Schlegel, G. E. Scuseria, M. A. Robb, J. R. Cheeseman, J. A. Montgomery Jr., T. Vreven, K. N. Kudin, J. C. Burant, J. M. Millam, S. S. Iyengar, J. Tomasi, V. Barone, B. Mennucci, M. Cossi, G. Scalmani, N. Rega, G. A. Petersson, H. Nakatsuji, M. Hada, M. Ehara, K. Toyota, R. Fukuda, J. Hasegawa, M. Ishida, T. Nakajima, Y. Honda, O. Kitao, H. Nakai, M. Klene, X. Li, J. E. Knox, H. P. Hratchian, J. B. Cross, V. Bakken, C. Adamo, J. Jaramillo, R. Gomperts, R. E. Stratmann, O. Yazyev, A. J. Austin, R. Cammi, C. Pomelli, J. W. Ochterski, P. Y. Ayala, K. Morokuma, G. A. Voth, P. Salvador, J. J. Dannenberg, V. G. Zakrzewski, S. Dapprich, A. D. Daniels, M. C. Strain, O. Farkas, D. K. Malick, A. D. Rabuck, K. Raghavachari, J. B. Foresman, J. V. Ortiz, Q. Cui, A. G. Baboul, S. Clifford, J. Cioslowski, B. B. Stefanov, G. Liu, A. Liashenko, P. Piskorz, I. Komaromi, R. L. Martin, D. J. Fox, T. Keith, M. A. Al-Laham, C. Y. Peng, A. Nanayakkara, M. Challacombe, P. M. W. Gill, B. Johnson, W. Chen, M. W. Wong, C. Gonzalez, and J. A. Pople. Gaussian 03, Revision E.01, (2004).

[169] H. Kuramochi, S. Takeuchi, K. Yonezawa, H. Kamikubo, M. Kataoka, and T. Tahara. Probing Ultrafast Structural Dynamics of Photoactive Yellow Protein with Femtosecond Time-Domain Raman Spectroscopy. In *19th Int. Conf. Ultrafast Phenom.*, page 10.Thu.D.5, Washington, D.C., (2014). OSA.

[170] O. Kfir, P. Grychtol, E. Turgut, R. Knut, D. Zusin, D. Popmintchev, T. Popmintchev, H. Nembach, J. M. Shaw, A. Fleischer, H. Kapteyn, M. Murnane, and O. Cohen, Generation of bright

phase-matched circularly-polarized extreme ultraviolet high harmonics, *Nat. Photonics*, **9**, 99–105 (2014).

[171] R. Cireasa, A. E. Boguslavskiy, B. Pons, M. C. H. Wong, D. Descamps, S. Petit, H. Ruf, N. Thiré, A. Ferré, J. Suarez, J. Higuet, B. E. Schmidt, A. F. Alharbi, F. Légaré, V. Blanchet, B. Fabre, S. Patchkovskii, O. Smirnova, Y. Mairesse, and V. R. Bhardwaj, Probing molecular chirality on a sub-femtosecond timescale, *Nat. Phys.*, **11**, 654–658 (2015).

[172] a. Brodeur and S. Chin, Band-Gap Dependence of the Ultrafast White-Light Continuum, *Phys. Rev. Lett.*, **80**, 4406–4409 (1998).

[173] P. Wittung-Stafshede, J. C. Lee, J. R. Winkler, and H. B. Gray, Cytochrome b562 folding triggered by electron transfer: approaching the speed limit for formation of a four-helix-bundle protein., *Proc. Natl. Acad. Sci. U. S. A.*, **96**, 6587–90 (1999).

[174] M. Gruebele, J. Sabelko, R. Ballew, and J. Ervin, Laser temperature jump induced protein refolding, *Acc. Chem. Res.*, **31**, 699–707 (1998).

[175] P. Baum, S. Lochbrunner, and E. Riedle, Tunable sub-10-fs ultraviolet pulses generated by achromatic frequency doubling., *Opt. Lett.*, **29**, 1686–1688 (2004).

[176] C. Nagura, A. Suda, H. Kawano, M. Obara, and K. Midorikawa, Generation and characterization of ultrafast white-light continuum in condensed media., *Appl. Opt.*, **41**, 3735–42 (2002).

[177] K. a. Jongeward, K. a. Jongeward, D. Magde, D. Magde, D. J. Taube, D. J. Taube, J. C. Marsters, J. C. Marsters, T. G. Traylor, T. G. Traylor, V. S. Sharma, and V. S. Sharma, Picosecond and Nanosecond Geminate Recombination of Myoglobin with Co, O-2, No, and Isocyanides, *J. Am. Chem. Soc.*, **110**, 380–387 (1988).

[178] M. Lim, T. A. Jackson, and P. A. Anfinrud, Nonexponential protein relaxation: dynamics of conformational change in myoglobin., *Proc. Natl. Acad. Sci.*, **90**, 5801–5804 (1993).

[179] Y. Mizutani and T. Kitagawa, Direct observation of cooling of heme upon photodissociation of carbonmonoxy myoglobin, *Science*, **278**, 443 (1997).

[180] J. W. Petrich, C. Poyart, and J. L. Martin, Photophysics and reactivity of heme proteins: a femtosecond absorption study of hemoglobin, myoglobin, and protoheme., *Biochemistry*, **27**, 4049–4060 (1988).

[181] M. Levantino, G. Schirò, H. T. Lemke, G. Cottone, J. M. Glownia, D. Zhu, M. Chollet, H. Ihee, A. Cupane, and M. Cammarata, Ultrafast myoglobin structural dynamics observed with an X-ray free-electron laser, *Nat. Commun.*, **6**, 6772 (2015).

[182] T. Dartigalongue, C. Niezborala, and F. Hache, Subpicosecond UV spectroscopy of carbonmonoxy-myoglobin: absorption and circular dichroism studies., *Phys. Chem. Chem. Phys.*, **9**, 1611–5 (2007).

[183] R. W. Woody and M.-C. Hsu, Origin of the heme Cotton effects in myoglobin and hemoglobin, *J. Am. Chem. Soc.*, **93**, 3515–3525 (1971).

[184] X. Ye, D. Ionascu, F. Gruia, A. Yu, A. Benabbas, and P. M. Champion, Temperature-dependent heme kinetics with nonexponential binding and barrier relaxation in the absence of protein conformational substates., *Proc. Natl. Acad. Sci. U. S. A.*, **104**, 14682–7 (2007).

[185] P. Kukura, D. W. McCamant, S. Yoon, D. B. Wandschneider, and R. A. Mathies, Structural observation of the primary isomerization in vision with femtosecond-stimulated Raman., *Science*, **310**, 1006–9 (2005).

[186] K. J. Hellingwerf, J. Hendriks, and T. Gensch, Photoactive Yellow Protein, A New Type of Photoreceptor Protein: Will This "Yellow Lab" Bring Us Where We Want to Go?, *J. Phys. Chem. A*, **107**, 1082–1094 (2003).

[187] N. Koumura, E. M. Geertsema, M. B. v. Gelder, A. Meetsma, and B. L. Feringa, Second generation light-driven molecular motors. Unidirectional rotation controlled by a single stereogenic center with near-perfect photoequilibria and acceleration of the speed of rotation by structural modification., *J. Am. Chem. Soc.*, **124**, 5037–51 (2002).

[188] H. Yoon, J. M. Lim, H. C. Gee, C. H. Lee, Y. H. Jeong, D. Kim, and W. D. Jang, A porphyrin-based molecular tweezer: Guest-induced switching of forward and backward photoinduced energy transfer, *J. Am. Chem. Soc.*, **136**, 1672–1679 (2014).

[189] H. Murakami, a. Kawabuchi, K. Kotoo, M. Kunitake, and N. Nakashima, A light-driven molecular shuttle based on a rotaxane, *J. Am. Chem. Soc.*, **119**, 7605–7606 (1997).

[190] T. Muraoka, K. Kinbara, and T. Aida, Mechanical twisting of a guest by a photoresponsive host., *Nature*, **440**, 512–5 (2006).

[191] H. C. BERG and R. A. ANDERSON, Bacteria Swim by Rotating their Flagellar Filaments, *Nature*, **245**, 380–382 (1973).

[192] M. Kodaka, A general rule for circular dichroism induced by a chiral macrocycle, *J. Am. Chem. Soc.*, **115**, 3702–3705 (1993).

[193] S. Allenmark, Induced circular dichroism by chiral molecular interaction, *Chirality*, **422**, 409–422 (2003).

[194] S. Ostovarpour and E. W. Blanch, Phosphorylation detection and characterization in ribonucleotides using Raman and Raman optical activity (ROA) spectroscopies., *Appl. Spectrosc.*, **66**, 289–93 (2012).

[195] K. P. Knutsen, B. M. Messer, R. M. Onorato, and R. J. Saykally, Chirped coherent anti-stokes Raman scattering for high spectral resolution spectroscopy and chemically selective imaging., *J. Phys. Chem. B*, **110**, 5854–64 (2006).

[196] M. Cui, J. Skodack, and J. P. Ogilvie, Chemical imaging with Fourier transform coherent anti-Stokes Raman scattering microscopy., *Appl. Opt.*, **47**, 5790–8 (2008).

[197] K. B. Shi, H. F. Li, Q. Xu, D. Psaltis, and Z. W. D. O. P. Liu, Coherent Anti-Stokes Raman Holography for Chemically Selective Single-Shot Nonscanning 3D Imaging, *Phys. Rev. Lett.*, **104** (2010).

[198] A. Wipfler, J. Rehbinder, T. Buckup, and M. Motzkus, Elimination of two-photon excited fluorescence using a single-beam coherent anti-Stokes Raman scattering setup, *J. Raman Spectrosc.*, **44**, 1379–1384 (2013).

[199] T. Ideguchi, S. Holzner, B. Bernhardt, G. Guelachvili, N. Picqué, and T. W. Hänsch, Coherent Raman spectro-imaging with laser frequency combs, *Nature*, **502**, 355–358 (2013).

[200] B. Littleton, T. Kavanagh, F. Festy, and D. Richards, Spectral interferometric implementation with passive polarization optics of coherent anti-stokes raman scattering, *Phys. Rev. Lett.*, **111**, 2–6 (2013).

[201] P. O. Brown, D. Botstein, M. Lapidot, Y. Pilpel, A. Mazo, J. W. Hodgson, S. Petruk, Y. Sedkov, H. W. Brock, J. a. Timmons, L. Good, P. Kapranov, a. T. Willingham, T. R. Gingeras, O. Yazgan, J. E. Krebs, M. E. Fahey, T. F. Moore, D. G. Higgins, B. Lehner, G. Williams, R. D. Campbell, C. M. Sanderson, J. Shendure, G. M. Church, H. Kiyosawa, I. Yamanaka, N. Osato, S. Kondo, Y. Hayashizaki, D. J. Lipman, G. G. Carmichael, a. J. Simpson, S. J. D. Souza, a. a. Camargo, R. R. Brentani, B. a. Williams, K. Mccue, L. Schaeffer, B. Wold, S. Edwards, D. Shoemaker, and E. E. Schadt, Label-Free Biomedical Imaging with, *Science*, **1857**, 1857–1861 (2008).

[202] C. W. Freudiger, W. Min, G. R. Holtom, B. Xu, M. Dantus, and X. Sunney Xie, Highly specific label-free molecular imaging with spectrally tailored excitation-stimulated Raman scattering (STE-SRS) microscopy, *Nat. Photonics*, **5**, 103–109 (2011).

[203] Y. Ozeki, W. Umemura, and Y. Otsuka, High-speed molecular spectral imaging of tissue with stimulated Raman scattering, *Nat. Photonics*, **6**, 845–851 (2012).

[204] C. Fang, R. R. Frontiera, R. Tran, and R. A. Mathies, Mapping GFP structure evolution during proton transfer with femtosecond Raman spectroscopy., *Nature*, **462**, 200–4 (2009).

[205] S. Shim and R. A. Mathies, Femtosecond Raman-induced Kerr effect spectroscopy, *J. Raman Spectrosc.*, **39**, 1526–1530 (2008).

[206] D. W. McCamant, P. Kukura, S. Yoon, and R. A. Mathies, Femtosecond broadband stimulated Raman spectroscopy: Apparatus and methods., *Rev. Sci. Instrum.*, **75**, 4971–80 (2004).

[207] S. E. Radford, Protein folding: progress made and promises ahead., *Trends Biochem. Sci.*, **25**, 611–8 (2000).

[208] S. A. Adcock and J. A. McCammon, Molecular dynamics: Survey of methods for simulating the activity of proteins, *Chem. Rev.*, **106**, 1589–1615 (2006).

[209] T. R. Sosnick and D. Barrick, The folding of single domain proteins-have we reached a consensus?, *Curr. Opin. Struct. Biol.*, **21**, 12–24 (2011).

Acknowledgments

First of all, I would like to thank Prof. Takashi Nagata for providing the wonderful environment for carrying out the research projects and for his helpful advices. I have learned lots of things from his thorough understanding of science and logical discussions. I am grateful to him also for his kind financial support for attending conferences and studying abroad.

Secondly, my special gratitude goes to Prof. Hiro-o Hamaguchi. I started my research career under his guidance as an undergraduate student. I thank him for giving me opportunities to work on fascinating and challenging research projects and for fruitful discussions.

I am sincerely grateful to Prof. Hideaki Kano for giving me the opportunity for conducting CARS-ROA experiments in his laboratory at University of Tsukuba. I am also thankful to him for many interesting and stimulating discussions, in which the idea of CARS-ROA spectroscopy was born.

I gratefully acknowledge Prof. Kaoru Yamanouchi, my secondary supervisor in the Advanced Leading Graduate Course for Photon Science (ALPS). His advice from different viewpoints helps me to recognize my research objectively.

Discussion with the members of Nagata group, especially with Prof. Jonathan Woodward, Dr. Ryuzo Nakanishi, Dr. Joshua Beardmore, and Dr. Korenobu Matsuzaki has been markedly fruitful for my works. Also the time spending with the group members of Hamaguchi group, Dr. Rintaro Shimada, Dr. Hajime Okajima, and Dr. Masanari Okuno, in particular, have immensely helped my research advance.

I thank the financial support from JSPS fellowship for young researchers (DC1) both for living costs and for research expenses, from ALPS program of the University of Tokyo for visiting a foreign university for five months.

Last but not least, I would like to thank my family for all their financial support and encouragement. Especially, I am greatly thankful to my mother for raising me and respecting my curiosity about science.

December, 2015

Kotaro Hiramatsu